

Nanostructured Optoelectronics: Materials and Devices

Guest Editors: Hieu P. T. Nguyen, Shamsul Arafin, J. Piao,
and Tran Viet Cuong





Nanostructured Optoelectronics: Materials and Devices

**Nanostructured Optoelectronics:
Materials and Devices**

Guest Editors: Hieu P. T. Nguyen, Shamsul Arafin,
J. Piao, and Tran Viet Cuong



Copyright © 2016 Hindawi Publishing Corporation. All rights reserved.

This is a special issue published in "Journal of Nanomaterials." All articles are open access articles distributed under the Creative Commons Attribution License, which permits unrestricted use, distribution, and reproduction in any medium, provided the original work is properly cited.

Editorial Board

- Domenico Acierno, Italy
Katerina Aifantis, USA
Nageh K. Allam, USA
Margarida Amaral, Portugal
Martin Andersson, Sweden
Raul Arenal, Spain
Ilaria Armentano, Italy
Vincenzo Baglio, Italy
Lavinia Balan, France
Thierry Baron, France
Andrew R. Barron, USA
Reza Bayati, USA
Hongbin Bei, USA
Daniel Bellet, France
Stefano Bellucci, Italy
Enrico Bergamaschi, Italy
Samuel Bernard, France
Debes Bhattacharyya, New Zealand
Sergio Bietti, Italy
Giovanni Bongiovanni, Italy
Theodorian Borca-Tasciuc, USA
Mohamed Bououdina, Bahrain
Torsten Brezesinski, Germany
C. Jeffrey Brinker, USA
Christian Brosseau, France
Philippe Caroff, Australia
Victor M. Castaño, Mexico
Albano Cavaleiro, Portugal
Shafiu Chowdhury, USA
Jin-Ho Choy, Republic of Korea
Kwang-Leong Choy, UK
Yu-Lun Chueh, Taiwan
Elisabetta Comini, Italy
Giuseppe Compagnini, Italy
David Cornu, France
Miguel A. Correa-Duarte, Spain
P. Davide Cozzoli, Italy
Shadi A. Dayeh, USA
Luca Deseri, USA
Yong Ding, USA
Philippe Dubois, Belgium
Zehra Durmus, Turkey
Joydeep Dutta, Oman
Ali Eftekhari, USA
- Samy El-Shall, USA
Ovidiu Ersen, France
Claude Estournès, France
Andrea Falqui, KSA
Matteo Ferroni, Italy
Elena J. Foster, USA
Ilaria Fratoddi, Italy
Alan Fuchs, USA
Miguel A. Garcia, Spain
Siddhartha Ghosh, Singapore
P. K. Giri, India
Russell E. Gorga, USA
Jihua Gou, USA
Jean M. Greneche, France
Smrati Gupta, Germany
Kimberly Hamad-Schifferli, USA
Simo-Pekka Hannula, Finland
Michael Harris, USA
Yasuhiko Hayashi, Japan
F. Hernandez-Ramirez, Spain
Michael Z. Hu, USA
Nay Ming Huang, Malaysia
Shaoming Huang, China
Zafar Iqbal, USA
Balachandran Jeyadevan, Japan
Xin Jiang, Germany
Rakesh Joshi, Australia
Jeong-won Kang, Republic of Korea
Hassan Karimi-Maleh, Iran
Antonios Kelarakis, UK
Alireza Khataee, Iran
Ali Khorsand Zak, Iran
Philippe Knauth, France
Ralph Krupke, Germany
Christian Kübel, Germany
Prashant Kumar, UK
Michele Laus, Italy
Eric Le Bourhis, France
Jun Li, Singapore
Meiyong Liao, Japan
Shijun Liao, China
Silvia Licocchia, Italy
Wei Lin, USA
Nathan C. Lindquist, USA
Zainovia Lockman, Malaysia
- Nico Lovergine, Italy
Jim Low, Australia
Jue Lu, USA
Ed Ma, USA
Laura M. Maestro, Spain
Gaurav Mago, USA
Muhamamd A. Malik, UK
Devanesan Mangalaraj, India
Sanjay R. Mathur, Germany
Tony McNally, UK
Yogendra Mishra, Germany
Paulo Cesar Morais, Brazil
Paul Munroe, Australia
Jae-Min Myoung, Republic of Korea
Rajesh R. Naik, USA
Albert Nasibulin, Russia
Toshiaki Natsuki, Japan
Koichi Niihara, Japan
Natalia Noginova, USA
Sherine Obare, USA
Won-Chun Oh, Republic of Korea
Atsuto Okamoto, Japan
Abdelwahab Omri, Canada
Ungyu Paik, Republic of Korea
Piersandro Pallavicini, Italy
Edward A. Payzant, USA
Alessandro Pegoretti, Italy
Ton Peijs, UK
Oscar Perales-Pérez, Puerto Rico
Jorge Pérez-Juste, Spain
Alexey P. Popov, Finland
Philip D. Rack, USA
Peter Reiss, France
Orlando Rojas, USA
Marco Rossi, Italy
Ilker S. Bayer, Italy
Cengiz S. Ozkan, USA
Sudipta Seal, USA
Shu Seki, Japan
Vladimir Šepelák, Germany
Huaiyu Shao, Japan
Prashant Sharma, USA
Donglu Shi, USA
Bhanu P. Singh, India
Surinder Singh, USA



Vladimir Sivakov, Germany
Ashok Sood, USA
Adolfo Speghini, Italy
Marinella Striccoli, Italy
Xuping Sun, KSA
Ashok K. Sundramoorthy, USA
Angelo Taglietti, Italy
Bo Tan, Canada
Leander Tapfer, Italy
Valeri P. Tolstoy, Russia
Muhammet S. Toprak, Sweden

R. Torrecillas, Spain
Achim Trampert, Germany
Takuya Tsuzuki, Australia
Tamer Uyar, Turkey
Bala Vaidhyanathan, UK
Luca Valentini, Italy
Rajender S. Varma, USA
Ester Vazquez, Spain
Ajayan Vinu, Australia
Ruibing Wang, Macau
Shiren Wang, USA

Yong Wang, USA
Magnus Willander, Sweden
Ping Xiao, UK
Zhi Li Xiao, USA
Yangchuan Xing, USA
Doron Yadlovker, Israel
Yoke K. Yap, USA
Kui Yu, Canada
William Yu, USA
Michele Zappalorto, Italy
Renyun Zhang, Sweden

Contents

Nanostructured Optoelectronics: Materials and Devices

Hieu P. T. Nguyen, Shamsul Arafin, J. Piao, and Tran Viet Cuong

Volume 2016, Article ID 2051908, 2 pages

Optimization of DWDM Demultiplexer Using Regression Analysis

Venkatachalam Rajarajan Balaji, Mahalingam Murugan, and Savarimuthu Robinson

Volume 2016, Article ID 9850457, 10 pages

A Method to Control Dynamic Errors of the Stylus-Based Probing System for the Surface Form Measurement of Microstructures

Hui Fang, Bin Xu, Deqiang Yin, and Shiping Zhao

Volume 2016, Article ID 3727514, 8 pages

Nanostructural Effect of ZnO on Light Extraction Efficiency of Near-Ultraviolet Light-Emitting Diodes

Young Jae Park, Hyounsuk Song, Kang Bok Ko, Beo Deul Ryu, Tran Viet Cuong, and Chang-Hee Hong

Volume 2016, Article ID 7947623, 6 pages

Atomistic Tight-Binding Theory of Electron-Hole Exchange Interaction in Morphological Evolution of CdSe/ZnS Core/Shell Nanodisk to CdSe/ZnS Core/Shell Nanorod

Worasak Sukkabot

Volume 2016, Article ID 1572641, 6 pages

First-Principle Study on the Interaction between Fe and Trivacancy in Graphene

Xielong Hu and Fanyan Meng

Volume 2016, Article ID 2672816, 7 pages

Photoactive Layer of DSSCs Based on Natural Dyes: A Study of Experiment and Theory

Yuanzuo Li, Huixing Li, Peng Song, and Chaofan Sun

Volume 2015, Article ID 139382, 6 pages

Editorial

Nanostructured Optoelectronics: Materials and Devices

Hieu P. T. Nguyen,¹ Shamsul Arafin,² J. Piao,³ and Tran Viet Cuong⁴

¹Department of Electrical and Computer Engineering, New Jersey Institute of Technology, Newark, NJ 07102, USA

²Department of Electrical and Computer Engineering, University of California, Santa Barbara, CA 93106, USA

³Epitaxial Laboratory, Inc., Dix Hills, NY 11746, USA

⁴Department of Solid State Physics, University of Science, Vietnam National University, Ho Chi Minh City, Vietnam

Correspondence should be addressed to Hieu P. T. Nguyen; hieu.p.nguyen@njit.edu

Received 11 July 2016; Accepted 11 July 2016

Copyright © 2016 Hieu P. T. Nguyen et al. This is an open access article distributed under the Creative Commons Attribution License, which permits unrestricted use, distribution, and reproduction in any medium, provided the original work is properly cited.

The use of nanostructure materials for optoelectronic devices, including light-emitting diodes (LEDs), laser diodes, photodetectors, and solar cells, has recently attracted considerable attention due to their unique geometry. Nanostructures in small dimensions can be perfectly integrated into a variety of technological platforms, offering novel physical and chemical properties for the high performance optoelectronic devices. The exploitation of new nanostructures and their optical and electrical properties is necessary for their emerging practical device applications.

This special issue contains six papers, presenting some recent advances in the theoretical calculation, synthesis, characterization, and application of such novel nanostructures.

Recently, natural dyes have been widely studied as potential sensitizers for dye-sensitized solar cells (DSSCs) due to their cost efficiency, nontoxicity, and complete biodegradation. In “Photoactive Layer of DSSCs Based on Natural Dyes: A Study of Experiment and Theory,” Y. Li et al. investigated, both theoretically and experimentally, three natural dyes for DSSCs which were extracted from natural plants, including *Forsythia suspensa*, Herba Violae, and Corn leaf. The authors reported that such natural dyes exhibit wide absorption region which covers almost the whole visible spectrum. The highest photoelectronic conversion efficiency for these natural dyes was recorded to be 0.96% with open circuit voltage of 0.66 V and short circuit current density of 1.97 mAcm^{-2} which is promising for future biophotovoltaics applications.

Among these novel nanostructures, recent rapid advances in research involving two-dimensional (2D) layered nanomaterials and nanoplasmonics could pave the way for developing

next-generation optoelectronic and photonic devices. Furthermore, the use of such 2D materials as a buffer layer for the growth of light-emitting III-V compound semiconductors by the so-called van der Waals epitaxy method has opened up a new route of heteroepitaxy, mitigating a lot of growth-related technological challenges. As an effort, this special issue features a theoretical paper relating to emerging 2D materials. X. Hu and F. Meng in “First-Principle Study on the Interaction between Fe and Trivacancy in Graphene” have reported the interaction between iron metal and monolayer graphene. In fact, this study has described a detailed investigation on the structural and electronic properties of graphene with vacancies as well as the advantages offered by having these vacancies on the graphene surface. These results certainly provide insights to engineer the electrical properties of graphene through defect addition and manipulation, being useful for industrial semiconductor applications such as the photocatalytic technology and graphene-based electronics.

In another paper, W. Sukkabot theoretically studied the impact of structure shapes on the electron-hole exchange interaction in core/shell nanostructure semiconductors. The study focused on the electron-hole exchange interaction in the morphological transformation of CdSe/ZnS core/shell nanodisk to CdSe/ZnS core/shell nanorod using atomistic tight-binding theory and a configuration interaction description. The aspect ratios were successfully used to study the structural and optical properties of such nanostructures. The single-particle and excitonic gaps are believed to be decreased by changing from disk to rod shapes. The authors concluded that light hole is suggested to be used for quantum information instead of a heavy hole. This study contributes

important information to the design of high performance II-VI semiconductor nanocrystals for optoelectronic applications.

Y. J. Park et al. reported their study on the enhanced light extraction efficiency of LEDs by employing two ZnO nanostructures. The experiments were performed on two types of nanostructures including one-dimensional nanorods and two-dimensional nanosheets which were grown directly on top of LEDs. The formation of surface texturing on LEDs with ZnO nanorods offers increased escape cone and surface scattering, resulting in the enhancement of light output power of 30% compared to conventional LEDs without using ZnO nanostructures. However, due to the increased internal reflection and light absorption in ZnO nanosheets, LEDs using nanosheet structures have lower light output efficiency compared to the conventional one. The employment of ZnO nanorods shows promising approach for the enhanced output power of LEDs. More importantly, LED devices are not severely suffering from degradation of electrical properties by using ZnO nanorods.

In the paper "A Method to Control Dynamic Errors of the Stylus-Based Probing System for the Surface Form Measurement of Microstructures," H. Fang et al. proposed a simple and cost-effective method to control dynamic errors of the stylus-based probing system on measuring the surface form of microstructures. The dynamic errors were numerically simulated and suggested that the scanning speed and initial position of the measured specimen directly affect the dynamic errors. The authors proposed a solution to enhance the form measurement accuracy of microstructures by using kinematical models to predict the influence of the measurement setup on dynamic performance. The dynamic errors, therefore, can be controlled by properly choosing the optimal scanning speed and the initial position of the measured samples.

V. R. Balaji et al. presented a novel design of twelve-channel Dense Wavelength Division Multiplexing (DWDM) demultiplexer using the two-dimensional photonic crystal (2D PC) square resonant cavity. The rod radius and wavelength were optimized by linear regression analysis. The authors claimed that their DWDM exhibits high accuracy of 95% with an average quality factor close to 8000. Importantly, the proposed PC based demultiplexer has small figure size and is perfectly applied in integrated optics.

Acknowledgments

The Guest Editors would like to thank all authors for their contributions to this special issue. They would also like to acknowledge reviewers of this special issue for their time and comments.

Hieu P. T. Nguyen
Shamsul Arafin
J. Piao
Tran Viet Cuong

Research Article

Optimization of DWDM Demultiplexer Using Regression Analysis

Venkatachalam Rajarajan Balaji,¹ Mahalingam Murugan,² and Savarimuthu Robinson³

¹Department of Electronics and Communication Engineering, St. Joseph's Institute of Technology, Chennai, Tamil Nadu 600119, India

²Department of Electronics and Communication Engineering, SRM Valliammai Engineering College, Kattankulathur, Tamil Nadu 603203, India

³Department of Electronics and Communication Engineering, Mount Zion College of Engineering and Technology, Pudukkottai, Tamil Nadu 622507, India

Correspondence should be addressed to Venkatachalam Rajarajan Balaji; vp@valliammai.co.in

Received 24 December 2015; Revised 5 May 2016; Accepted 31 May 2016

Academic Editor: James Piao

Copyright © 2016 Venkatachalam Rajarajan Balaji et al. This is an open access article distributed under the Creative Commons Attribution License, which permits unrestricted use, distribution, and reproduction in any medium, provided the original work is properly cited.

We propose a novel twelve-channel Dense Wavelength Division Multiplexing (DWDM) demultiplexer, using the two-dimensional photonic crystal (2D PC) with square resonant cavity (SRC) of ITU-T G.694.1 standard. The DWDM demultiplexer consists of an input waveguide, SRC, and output waveguide. The SRC in the proposed demultiplexer consists of square resonator and microcavity. The microcavity center rod radius (R_m) is proportional to refractive index. The refractive index property of the rods filters the wavelengths of odd and even channels. The proposed microcavity can filter twelve ITU-T G.694.1 standard wavelengths with 0.2 nm/25 GHz channel spacing between the wavelengths. From the simulation, we optimize the rod radius and wavelength with linear regression analysis. From the regression analysis, we can achieve 95% of accuracy with an average quality factor of 7890, the uniform spectral line-width of 0.2 nm, the transmission efficiency of 90%, crosstalk of -42 dB, and footprint of about 784 μm^2 .

1. Introduction

Fiber cable transfers the data for the long distance without loss, when compared to the coaxial transmission. However, individual fiber connectivity to single consumer needs robust and expensive routing system. To overcome the high-priced routing SMF connectivity to each consumer is the solution.

The single-mode optical fiber (SMF) works with wavelength division multiplexing (WDM) and DWDM techniques, for transferring multiple light waves with precise wavelengths inside the fiber. The SMF DWDM system in demultiplexer at the consumer end separates the multiple light wavelengths [1]. The demultiplexers are classified as passive and active demultiplexers. The passive demultiplexers design consists of frequency filters [2], prisms [3], and diffraction gratings [2]. The active demultiplexer comprises passive components and tunable detectors [4]. The disadvantages of active and passive demultiplexers are as follows: low normalized transmission power, high crosstalk, low-quality factor,

and scale of centimetres. The disadvantages of demultiplexers are overcome by replacing them with Photonics Integrated Circuits (PICs).

PICs consist of photonic crystals (PCs) which can maintain hundreds of channels through micro dimension scale. The growth of PCs in PIC drastically increases in the field of fiber optics. Photonic crystals are low loss periodic dielectric electromagnetic medium, with Photonic Band Gaps (PBGs). The PCs control the propagation of light with PBG. The PBG structure does not allow the light with different wavelengths in any direction [5, 6]. By introducing defects in the periodic structures the PBG is entirely broken which allows the different wavelength inside the structure. Typically, there are two kinds of defects reported, namely, line defects and point defects. The removal/change of structural parameters of the rods in a row or column is denoted as line defect; however, the change/removal of structural parameters of single rods are termed point defects. The structural parameters are the radius of the rod, the refractive index, and the lattice constant.

The line and point defects are very important to realize PC based optical devices. The PCs with defects can apply in designing various devices such as wavelength demultiplexers [7], beam splitters [8], optical logical encoder [9], ring resonators [10], and photonic sensors [11].

In WDM wavelength demultiplexers play a vital role for point-to-point networks, which are classified as coarse wavelength division multiplexing (CWDM) and DWDM. The CWDM comprises the ITU-T G.694.2 standard of eight wavelengths with 20 nm channel spacing. The DWDM consists of ITU-T G.694.1 criterion of 0.1, 0.2, 0.4, and 0.8 nm channel dispersing with 512 distinct wavelengths. The channel-dispersing feature of the DWDM standard attracts many researchers to improve the DWDM criterion. However, DWDM technology in fiber optics provides low attenuation and the dynamic usage of bandwidth for SMF. The SMF with DWDM technology uses multiple wavelengths as carriers and concedes them to transmit in the fiber concurrently to the consumer end.

From the literature survey, it is deemed that the 2D PC based demultiplexer for CWDM and the DWDM system is reported using line defects [12–17], ring resonant cavity [18, 19], and so forth, for introducing the line and point defects. As the ITU-T G.694.1 DWDM system has many benefits, which are very relevant, the authors have considered the DWDM system and presented the research results here. The DWDM demultiplexer using 2D PC has a T-shaped structure with line defects resonant cavity [12–14] and P-shaped single resonant cavity with different rod radius to drop different wavelengths [20] and, hence, the multi-T-shaped structure with line/point defects [15–17], X-ring cavity [18], and resonant cavity/line defects [19]. From the literature survey, it is identified that the demultiplexer is designed using different shapes of the cavity. However, the transmission efficiency, crosstalk, and Q factor need improvement to meet the future requirements. Hence, in this paper, a new square ring resonant cavity/point defects based demultiplexer has been proposed and designed to work with constructive interferences that result in high transmission efficiency.

The DWDM demultiplexer is of two and four channels. The drawbacks of the earlier works are less channel number, nonuniform spectral line-width for dropped channels, low Q factor, and low transmission efficiency [12–19]. The DWDM of six and eight channels to improve the aforementioned parameters with novel demultiplexer structure is formed. The increasing channels in DWDM reduce the cost, and best optimization is obtained since the number of users increased with the number of channels. The proposed 12-channel DWDM has odd and even distinct color wavelengths. The demultiplexer is formed with the combination of square ring resonator, a waveguide, and microcavity rods in a 2D photonic crystal. In the demultiplexer for developing 12-channel DWDM, we design a filter in a position to drop high-intensity resonant wavelength on the influence of microcavity inner rod (R_m). The radius of the rod (R_m) is 100% reflection situation.

This paper is prepared as follows: Section 2 discusses the band diagram for 50×50 PC structures earlier than inducing the defects. Section 3 describes the design of microcavity and

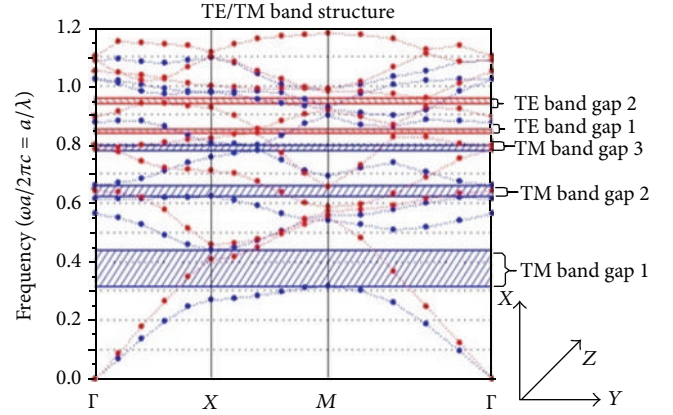


FIGURE 1: Band diagram for 50×50 PC structures before inducing the defects.

its features. The novel design for 12-channel demultiplexer is proposed in Section 4. The simulations outcome and discussion are analyzed in Section 5. Section 6 discusses the regression evaluation to optimize the radius of rods with wavelength. Subsequently, Section 7 concludes the paper.

2. Photonic Crystal Geometry

The proposed DWDM demultiplexer uses the 2-dimensional photonic crystal square lattice, and it will be better to attain horizontal confinement of light by the use of square lattice structure. The filter is developed with 50×50 rods in the X and Z direction for higher coupling of modes. The high refractive index Si rods and background air are 3.48 and 1; each rod has a radius $R = 110$ nm, where the lattice constant $a = 560$ nm and silicon permittivity (ϵ) = 11.9.

The analysis of PC band structure is studied by the Plane Wave Expansion (PWE) method. The PWE method calculates PBG in propagation modes for the periodic and nonperiodic structures [21]. The electromagnetic wave propagation modes in photonic crystal analysis follow Maxwell's equations:

$$\nabla \times \left(\frac{1}{\epsilon(r)} \nabla \times E(r) \right) = \frac{\omega^2}{c^2} E(r), \quad (1)$$

where $\epsilon(r)$ represents the dielectric function, " ω " is the angular frequency, $E(r)$ represents the electric field of periodic structure, and " c " is the speed of the light. From (1), the 2D PC band structure is determined.

The photonic crystal realizes the fields in two polarizations: TE polarization where the electrical field is polarized in XY plane, that is, magnetic field in direction of propagation (Z), and TM polarization, the place the magnetic field is parallel to the interface and electric field is within the propagation direction (Z).

The proposed band structure before introducing the defects is shown in Figure 1, which has three TM PBGs and two TE PBGs in the band diagram as shown in Figure 1. The normalized frequency and its wavelength range are listed in Table 1. In the table, first TM PBG wavelength, lies between

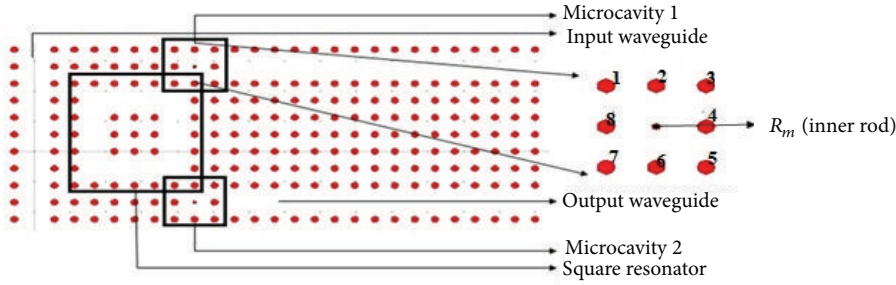


FIGURE 2: A single resonant cavity with two microcavities.

TABLE 1: Photonic band gap and normalized frequency and its corresponding wavelength of the proposed structure.

S. number	PBG	Normalized frequency (a/λ)	Wavelength (nm)
1	TM PBG	0.31–0.445	1258–1806
		0.588–0.6455	867–952
		0.768–0.778	729–719
2	TE PBG	0.923–0.934	599–606
		0.825–0.835	670–678

1258 nm and 1806 nm for low loss communication, since the frequency lies in the third window of optical communication in proposed work. All the simulation performs with TM mode where the electric field is perpendicular to the rod axis. The proposed band structure design uses a 12-channel DWDM filter. Finite Difference Time Domain (FDTD) is utilized to analyze the transmission and reflection spectrum of the photonic device including photonic crystals. The FDTD method simulates the propagation of electromagnetic waves inside the PCs [22].

3. Microcavity Design

Figure 2 shows the single resonant cavity with two microcavities. The microcavity with point defect shown is separated and magnified, in Figure 2. The microcavity with point defects is introduced. The point defect is created by altering the shape, size, and dielectric constant of the rods. The sizes of the rods increase with the change of refractive index; so, the desired wavelength is tuned. The SRC has a square resonator and microcavity. The microcavity consists of one center rod surrounded by 8 reflecting rods. The 8 rods are used to control the width of the resonant frequency in the band gap. The center rod (R_m) is used to tune the desired wavelength with high intensity. The square resonator is used to localize the photon inside the region. Once the distinct photons couple with the microcavity, it tunes the coupled wavelength with the high resonant frequency with the presence of the rod (R_m). The high resonant frequency for 1554.9 nm is shown in Figure 3 after simulation.

The microcavity performance is analyzed with Q factor. Typically, the Q factor determines the selectivity of

the demultiplexer and the Q factor is calculated separately for all the channels using the following formula:

$$Q \equiv \omega_0 \tau_{ph} \equiv \frac{\lambda_r}{\Delta\lambda}, \quad (2)$$

where λ_r is resonant wavelength of the desired channel and $\Delta\lambda$ represents the Full Width at Half Maximum point for the desired channel. In the proposed DWDM model, the microcavity increases the Q factor and shows better performance when compared to the existing DWDM demultiplexer.

4. Multichannel Filter Design

Figure 4 shows the twelve-channel DWDM demultiplexer schematic. The proposed DWDM demultiplexer utilizes 50×50 rods, with the $784 \mu\text{m}^2$ lattice structure, which can acquire narrower spectral line-width. The DWDM also filters precise color wavelength through the constitution of the resonant cavity. The square resonant cavity filter consists of square ring resonator and microcavity rods. The square ring resonator straps the photons in the cavity when low resistance with specific color wavelength occurs and the color wavelength couples to microcavity cells. In this novel design, microcavity cells work as wavelength selective filter to drop the desired wavelengths. The rods in microcavity cells work to separate the even and odd color wavelengths by adjusting the radius of microcavity inner rods (R_m). The radius of the microcavity interior rod (R_m) increases due to the high-intensity resonant wavelength. As soon as the radius of the R_m increases, the refractive index in rods increases due to the fact that the resonant wavelength also shifts with 0.2 nm channel spacing. The rods around the microcavity control the width of the channel spacing of desired color wavelengths. Figure 2 shows the base of the single resonant cavity designed to 12-channel DWDM demultiplexer. The 12-channel DWDM demultiplexer design has six resonant cavities, where each cavity is to drop two distinct color wavelengths. The six resonant cavities are positioned between the input bus waveguide and the output drop waveguide. The input bus waveguide is designed by eliminating 47 rods in the lattice. Likewise output drop waveguide works with removing 16 rods in each channel. The 15 rods are left for designing the square resonant cavity. The distance between waveguide and the cavity is deemed to be

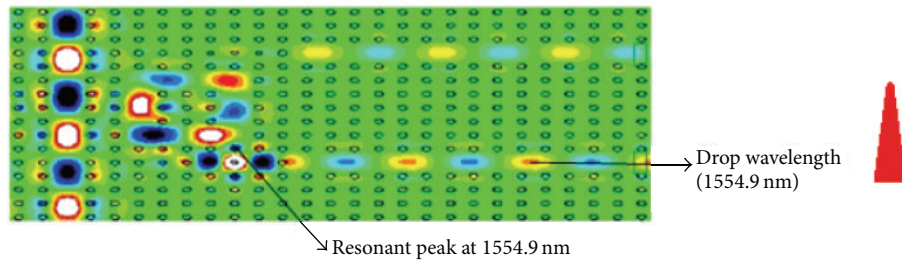


FIGURE 3: Electric field distribution of a single resonant cavity for color wavelength 1554.9 nm.

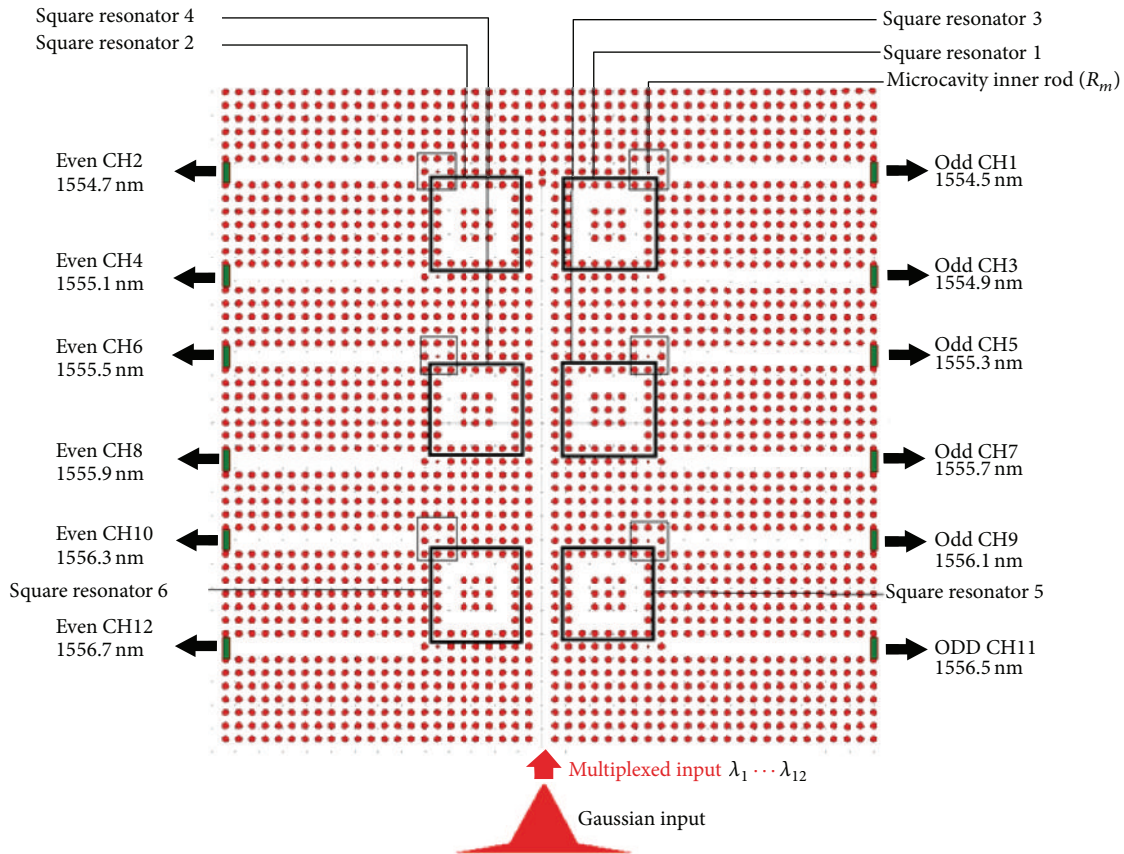


FIGURE 4: Schematic diagram of the proposed twelve-channel demultiplexer using PC square resonant cavity.

good with two rows of rods in order to reduce the coupling loss and the back reflection loss.

The novel resonant cavity works with two microcavities, one microcavity positioned at the higher end of the cavity and the other microcavity placed below the cavity. The microcavity is partitioned into eight rods and core rod radius named R_m . The radius of rods (R_m) increases for every microcavity to filter the desired color wavelength.

The walls of the cavity are used to control the width of a resonant frequency. To design a 12-channel DWDM demultiplexer, we include six resonant cavities. Each cavity design has two branches with distinct defects in its dimension. The two channel branches from the single resonant cavity with a separation of seven rows of rods are shown in Figure 4. The proposed design exhibits more quantity of

channels with the small footprint. As we stated previously with increasing microcavity core rods (R_m) are able to shift the resonant wavelength on the higher side which controls the channel spacing (0.2 nm) through the surrounding rods of the microcavity. We added point defects (R_m) with 12 different sizes to drop 12 channels. The radius (R_m , $m = 1, 2, 3, 4, 5, 6, 7, 8, 9, 10, 11, 12$) is given as $R_1 = 41.5$ nm, $R_2 = 41.95$ nm, $R_3 = 42.4$ nm, $R_4 = 42.85$ nm, $R_5 = 43.3$ nm, $R_6 = 43.75$ nm, $R_7 = 44.20$ nm, $R_8 = 44.65$ nm, $R_9 = 45.10$ nm, $R_{10} = 45.55$ nm, $R_{11} = 46$ nm, and $R_{12} = 46.45$ nm.

The desired wavelengths are the drop with a radius of the microcavity inner rods (R_m) due to the filter. Other parameters are constant such as nondefected rods, lattice constant, and refractive index. The channels are designed to drop the desired wavelength with high transmission efficiency,

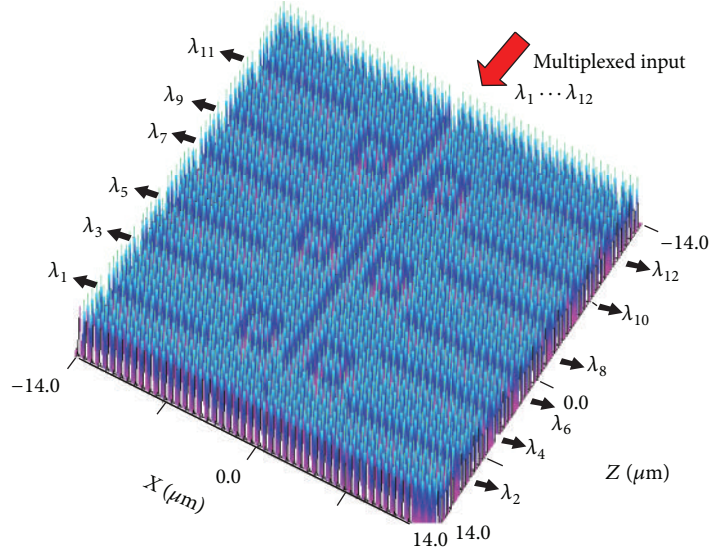


FIGURE 5: 3D view of the proposed twelve-channel demultiplexer.

high Q , and narrow line-width. The designed demultiplexer selects the radius of the microcavity inner rods (R_m) with optimized simulation under different conditions, like characteristics of rods, the lattice constant, and refractive index. The demultiplexer is designed with twelve ports to drop the twelve desired wavelengths. The 3D view of proposed twelve-channel demultiplexer is depicted in Figure 5. The size of the demultiplexer is $28 \mu\text{m} \times 28 \mu\text{m}$, which is very small; hence, it could be easily deployed in PICs.

5. Simulation Results and Discussion

The proposed DWDM demultiplexer is simulated using FDTD with PML ABC. The proposed crystal structure utilizes PML ABC (PML Absorbing Boundary Conditions) to optimize the boundary region without reflection of electromagnetic waves. To observe boundary conditions without any reflection of electromagnetic waves for all the frequency and angle of incidence with PML layer, formulate Maxwell's equations [23].

The absorption rate is higher in the PML ABC structure, whereas other boundary conditions show more reflections during simulations. The proposed model utilizes PML width and reflection as 500 nm , PML, and 10^{-8} , respectively. The FDTD grid size in the simulation at 28 nm ($x/20 = 0.05a$) works significantly in DWDM environment. The proposed 12-channel DWDM demultiplexer makes use of spatial Gaussian pulse within the input waveguide. The power monitor is placed on the end of the waveguide with the intention of receiving the normalized output transmission. The output transmission spectrum is acquired using Fourier transform of the electric field using the monitor. The normalized transmission is calculated with

$$T(f) = \frac{1/2 \int \text{real}(p(f)^{\text{monitor}}) \cdot dS}{\text{SourcePower}}, \quad (3)$$

where $T(f)$ denotes normalized transmission about the frequency, $p(f)$ denotes the pointing vector, and dS denotes surface normal preserving right time step in the FDTD simulation having an effect on DWDM environment. The time step should follow this rule in the filter:

$$\Delta t \leq \frac{1}{c\sqrt{1/\Delta X^2 + 1/\Delta Y^2}}, \quad (4)$$

where Δt represents the step time and c represents the speed of light in free space. The filter is simulated with an increment of 0.0001 nm for a 4476 min runtime for memory structure of 53.6 MB to get high Q factor output. The size of the structure in X and Z direction is $28 \mu\text{m}$ and $28 \mu\text{m}$, so the footprint proposed demultiplexer is $784 \mu\text{m}^2$.

In the previous work on the DWDM demultiplexer, more focus was on four channels and less focus was on eight channels. The increasing channels in DWDM reduce the cost, and the best optimization is obtained since number of users increased with number of channels. The paper shows the results with 12-channel DWDM demultiplexer. The proposed design utilized the benefits of both square resonator and novel microcavity. The square resonator straps the modes within the cavity with the sustained time and microcavity tuned to couple the distinct color wavelength with high resonant frequency simply with point defects. The resonant cavity is designed with the novel microcavity. The novel microcavity can filter the distinct DWDM wavelengths with the change in inner rods. The radius of inner rods is optimized for simulation under different conditions (characteristics of rods, a lattice constant, and refractive index) to separate odd and even distinct wavelengths. This approach drastically reduces the crosstalk between neighbour channels in practical.

The output spectra of proposed twelve-channel demultiplexer for odd channels and even channels are as shown in Figures 6 and 7. The wavelengths in Figures 6, 7, and 8 attain

TABLE 2: The summary of various parameters of the twelve-channel DWDM demultiplexer for odd channels.

DWDM channel/wavelength λ_r (nm)	Defect rod (R_m) (nm)	Spectral linewidth ($\Delta\lambda$) in (nm)	Q factor	Efficiency (%)
λ_1 -1554.5 nm	41.5	0.2	7772.5	90
λ_3 -1554.9 nm	42.4	0.2	7774.5	94
λ_5 -1555.3 nm	43.3	0.2	7776.5	98
λ_7 -1555.7 nm	44.20	0.2	7778.5	93
λ_9 -1556.1 nm	45.10	0.2	7780.5	99
λ_{11} -1556.5 nm	46	0.2	7782.5	92

TABLE 3: The summary of various parameters of the twelve-channel DWDM demultiplexer for even channels.

DWDM channel/wavelength λ_r (nm)	Defect rod (R_m) (nm)	Spectral linewidth ($\Delta\lambda$) in (nm)	Q factor	Efficiency (%)
λ_2 -1554.7 nm	41.95	0.2	7773.5	99.4
λ_4 -1555.1 nm	42.85	0.2	7775.5	95.3
λ_6 -1555.5 nm	43.75	0.2	7777.5	100
λ_8 -1555.9 nm	44.65	0.2	7779.5	94
λ_{10} -1556.3 nm	45.55	0.2	7781.5	91.3
λ_{12} -1556.7 nm	46.45	0.2	7783.5	99

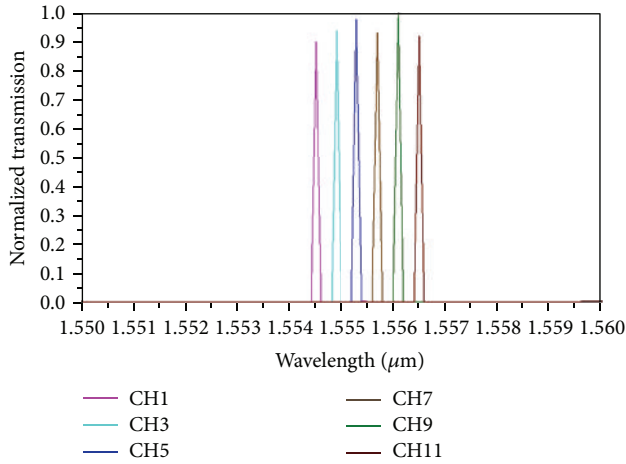


FIGURE 6: Normalized output spectra of twelve-channel DWDM demultiplexer for the odd channel.

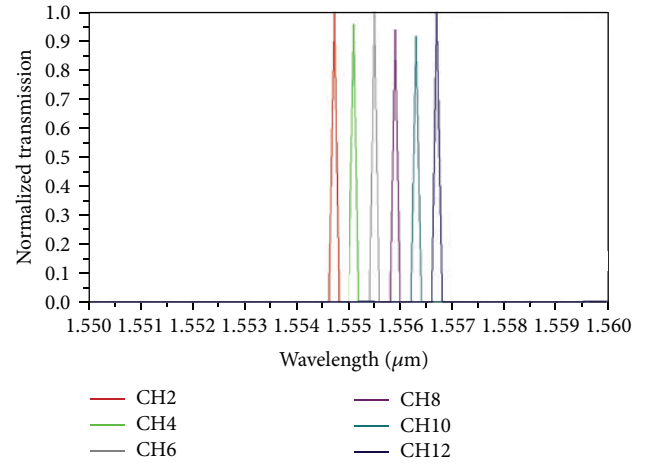


FIGURE 7: Normalized output spectra of twelve-channel DWDM demultiplexer for even channel.

ITU-T G.694.1 DWDM system and the output spectra of twelve-channel DWDM demultiplexer are shown in Figure 8.

The resonant wavelengths of the DWDM system observed at 1554.5 nm, 1554.9 nm, 1555.3 nm, 1555.7 nm, 1556.1 nm, 1556.5 nm, 1554.7 nm, 1555.1 nm, 1555.5 nm, 1555.9 nm, 1556.3 nm, and 1556.7 nm lie in C band of the optical window. The C band window widely prefers the network due to low loss communication. The complete specifications of the twelve-channel DWDM demultiplexer for odd and even channels are listed in Tables 2 and 3.

In this paper, authors designed 2D PC based 12-channel demultiplexer for DWDM ITU-T G.694.1 standard system.

Hence we have considered that the wavelength range lies between 1554.5 nm and 1556.7 nm with 0.2 nm channel spacing. In order to attain the normalized output spectra which are shown in Figures 6–9, authors considered the wavelength increment (resolution) as 0.0001 nm from 1550 nm to 1560 nm (i.e., the total simulation period (time) is about 4476 minutes). The quality factor is calculated from (2); for example, the resonant wavelength and Full Width at Half Maximum of channel 1 are 1554.5 nm and 0.2 nm, respectively. From the above value, authors attained the Q factor value of 7772.5. Similarly, the Q factors calculated for all the other channels are listed in Tables 2 and 3.

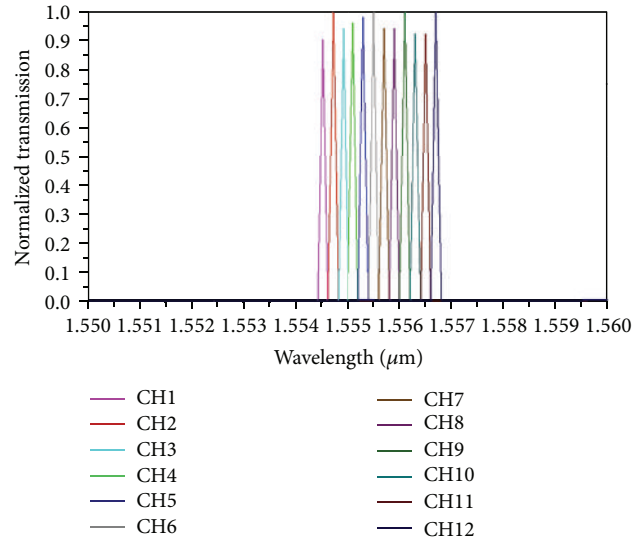


FIGURE 8: Normalized output spectra of twelve-channel DWDM demultiplexer with uniform spectral line-width 0.2 nm.

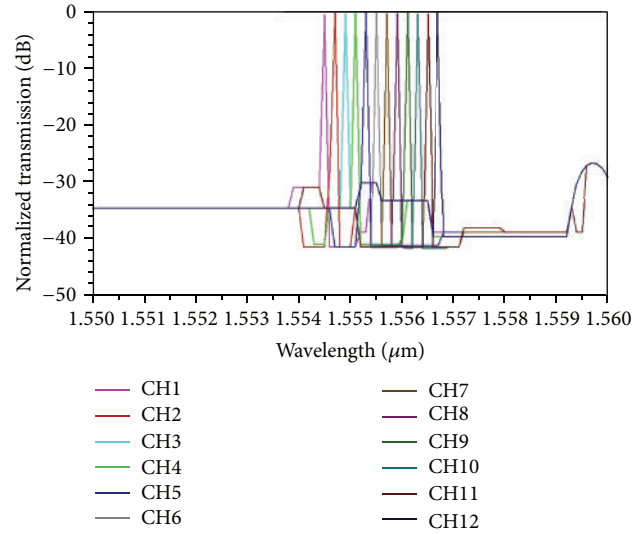


FIGURE 9: The spectral output of the twelve-channel DWDM demultiplexer in dB scale.

There are several microfabrication methods available for fabricating 2D PC. They are optical UV lithography, direct UV laser writing, electron-beam lithography, focused ion beam, and multiexposure holography. Above all, electron-beam lithography and dry-etching techniques offer remarkable resolution of fabrication of PC based devices [24, 25]. In addition, technology could support fabricating the device with nm resolution. In addition, there are several attempts already made with less than 0.45 nm [14–17]. Hence our proposed work could be realized in near future.

The biggest challenge in designing DWDM demultiplexer is to obtain low crosstalk. The demultiplexer design is the focus to improve low crosstalk with proposed SRC cavity. The spectral response of demultiplexer in dB scale is seen in Figure 9 and is used to calculate the crosstalk among the channels (C_{ij}). From Figure 9, we observe that the crosstalk

of the channels varied over the range from -30 dB to -42 dB, which produces much small crosstalk, compared to the previous results. The crosstalk between channels is C_{ij} , where i and j denote the channel number. For example, C_{23} gives the crosstalk between channel 2 and channel 3. The crosstalk among the channels is listed in Table 4.

The functional characteristics of the proposed twelve-channel DWDM demultiplexer are compared to the reported DWDM demultiplexers, which are listed in Table 5. From Table 5, it is proved that the proposed square resonant cavity based demultiplexer works better than the existing DWDM design. From the simulation of various wavelengths, we achieved functional parameters such as a quality factor of 8000, the spectral line-width of 0.2 nm, a transmission efficiency of 90–100%, crosstalk of -42 dB, and device size of about $784 \mu\text{m}^2$. From the results, the existing DWDM system

TABLE 4: Crosstalk values (C_{ij}) of proposed twelve-channel PC based demultiplexer (dB).

Channels (C_{ij})	λ_1	λ_2	λ_3	λ_4	λ_5	λ_6	λ_7	λ_8	λ_9	λ_{10}	λ_{11}	λ_{12}
λ_1	NA	-30.7	-41.5	-41.5	-39.1	-30.1	-33.2	-33.4	-33.4	-33.4	-33.3	-39
λ_2	-31	NA	-32	-37	-30	-30	-33.3	-33.4	-33.2	-33.3	-33.4	-39.6
λ_3	-33	-34.2	NA	-31	-41.6	-41.6	-41.6	-41.6	-41.6	-41.6	-41.6	-41.6
λ_4	-34	-34	-31	NA	-32	-40.1	-40.1	-40.1	-40.1	-40.1	-33	-33
λ_5	-35	-41	-41	-33	NA	-37	-41.1	-41.1	-41.1	-41.1	-41.1	-41.1
λ_6	-35	-35	-35	-35	-37	NA	-41	-41	-41	-41	-41	-41
λ_7	-31.1	-34.8	-34.6	-41.1	-41.7	-37.1	NA	-37.3	-42.2	-42.4	-42.6	-42.8
λ_8	-34.5	-34.7	-34.8	-41.9	-41.6	41.5	-37.2	NA	-37.7	-41.9	-41.6	-41.3
λ_9	-34.5	-34.7	-34.9	-41.5	-41.6	-41.7	-41.8	-36.9	NA	-37.3	-41.7	-41.6
λ_{10}	-34.7	-34.7	-34.6	-41.5	-41.6	-41.6	-41.6	-41.6	-37.2	NA	-38	-41.9
λ_{11}	-34.8	-35	-34	-41.8	-41.8	-41.5	-41.5	-41.6	-41.6	-37.9	NA	-38.7
λ_{12}	-34	-34	-34	-30	-30	-33.4	-33.4	-33.4	-33.4	-33.3	-35.8	NA

TABLE 5: Comparison of the proposed and existing DWDM system.

Authors, year, and reference number	Number of output ports	Coupling efficiency (%)		Q factor	Crosstalk (dB)		Footprint (μm) ²	Spectral line-width (nm)
		Min	Max		Min	Max		
Rostami et al. 2010 [12]	4	42.5	86.5	3006	-30.00	-14.2	536	0.4 NUSL*
Liu et al. 2012 [13]	4	99	99.5	90	—	—	—	20 NUSL*
Alipour-Banaei et al. 2013 [18]	4	45	63	561	-23.70	-7.5	422.4	2.8 NUSL*
Gupta and Janyani 2014 [14]	4	40	80	7795	—	—	—	0.2 USL*
Kuo et al. 2007 [15]	6	25	60	416	-27	-17	—	3.2 NUSL*
Rakhshani et al. 2013 [16]	6	81	100	2319	-35	-23	—	NUSL*
Tian et al. 2013 [19]	8	65	90	1969	-18	-15	882	0.8 NUSL*
Mehdizadeh and Soroosh 2016 [17]	8	94	98	1723	-40	-11.2	495	1 NUSL*
<i>Proposed design</i>	<i>12</i>	<i>90</i>	<i>99</i>	<i>7783.5</i>	<i>-42</i>	<i>-30</i>	<i>784</i>	<i>0.2</i> <i>USL*</i>

* USL: uniform spectral linewidth for dropped wavelengths.

NUSL: nonuniform spectral linewidth for dropped wavelengths.

with nonuniform spectral line-width for drop wavelengths is replaced with a uniform spectral line-width one. The functional parameters are significantly enhanced with smaller size and the higher number of channels and hence the proposed demultiplexer can be implemented in the Photonic Integrated Circuits.

6. Optimization of Rods and Wavelengths in DWDM

The novel DWDM demultiplexer tunes the rods and wavelength of different sizes and wavelengths. The size of the rods

ranging from 41.5 nm to 46.45 nm shows the better performance compared to the below 40 nm rod size. The corresponding wavelength at 1554.5 nm and below the rod size of 40 nm shows more distortions. The maximum size of the rod without distortion has been observed at 65 nm. The rods and wavelength are optimized with regression analysis [26, 27] only for 12-channel DWDM. For the proposed 12-channel DWDM demultiplexer, it works better for the Si rods and background air with the refractive indexes of 3.48 and 1.0, respectively, and each rod has a radius $R = 110$ nm, where lattice constant $a = 560$ nm and silicon permittivity $\epsilon(\text{Si}) = 11.9$.

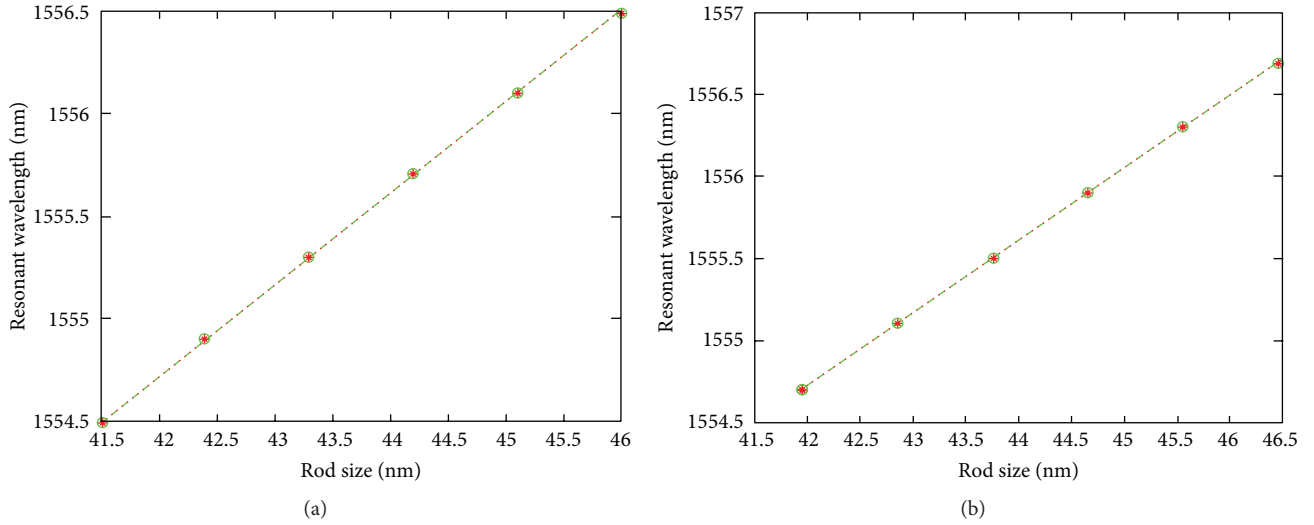


FIGURE 10: Effect of rods radius with the odd wavelength (a) and even wavelength (b).

The rods of different size (x) taken as n data points with respect to wavelength (y) and data point are $\{(x_i, y_i), i = 1, \dots, n\}$.

The straight line equation for data points is described with x as rod size and y as wavelength:

$$y_i = \alpha + \beta x_i. \quad (5)$$

In (5), α is the intercept for wavelength and β is the slope. We can provide the best fit for rod size and wavelength, the best fit derived with the least square approach, which reduces the sum of square residual of linear regression model.

By solving linear regression equations, we find the value optimization of rods and wavelength:

$$y = 0.444(x) + 1533.5. \quad (6)$$

From the above regression model we derived

$$\begin{aligned} \text{Wavelength} &= 0.444(\text{rods size}) \\ &+ \text{intercept for wavelength}, \end{aligned} \quad (7)$$

where y is the wavelength, x is the different rod size, and α is the intercept for wavelength.

In the proposed demultiplexer, radius of inner microcavity rod (R_m) is the important parameter for filtering the specific desired wavelengths. To demultiplex the desired wavelength, the radius of the rod (R_m) changes the odd resonant wavelength and the even resonant wavelength changes due to the change of refractive index as shown in Figure 10.

7. Summary

The proposed twelve-channel Dense Wavelength Division Multiplexing demultiplexer with the two-dimensional photonic crystal square resonant cavity fulfils the ITU-T recommendation of G.694.1 DWDM systems. The novelty in

proposed DWDM system drops the desired wavelength tuned with the radius of the inner rod (R_m), which is positioned in the microcavity. The spectral response of the proposed DWDM performs with an average of about 96% of transmission efficiency, -42 dB crosstalk with the quality factor of 8000. Further, the channel spacing and spectral line-width between the channels are 0.2 nm/25 GHz and 0.2 nm, respectively. The proposed PC based demultiplexer is excellent in fulfilling the requirements of ITU-T G.694.1 DWDM system and size is very small, about $784 \mu\text{m}^2$; it could be integrated for the integrated optics. From the results, the existing DWDM system with nonuniform spectral line-width for drop wavelengths is replaced with a uniform spectral line-width one. The crosstalk of proposed DWDM demultiplexer improves about -42 dB compared to previous works.

Competing Interests

There are no competing interests regarding the publication of this paper.

Acknowledgments

The authors are very much grateful to Dr. B. Chidambaranjan, Principal of Valliammai Engineering College, Kattankulathur, and Dr. R. Nakkeeran, Head of Electronics Engineering Department, School of Engineering & Technology, Pondicherry University, for their valid suggestions and inputs at suitable levels. Authors are extremely thankful to Professor N. Lakshmana Perumal, Professor and Head of English Department of Valliammai Engineering College, Kattankulathur, for his help in correcting the grammatical errors in the paper. Venkatachalam Rajarajan Balaji would like to acknowledge Dr. N. R. Shanker, Manager, Research and Development, Chase Technologies, Chennai, for his support at different times.

References

- [1] B. Hoanca, "DWDM fundamentals, components, and applications," *Journal of Optical Networking*, vol. 1, no. 5, pp. 184–185, 2002.
- [2] A. K. Dutta, N. K. Dutta, and M. Fujiwara, Eds., *WDM Technologies: Passive Optical Components: Passive Optical Components*, Academic Press, 2003.
- [3] I. Nishi, T. Oguchi, and K. Kato, "Broad-passband-width optical filter for multi/demultiplexer using a diffraction grating and a retroreflector prism," *Electronics Letters*, vol. 21, no. 10, pp. 423–424, 1985.
- [4] X. Xing and Y. Wang, "A planar lightwave circuit based on optical add-drop multiplexer with 16 tunable wavelength channels," *Advanced Materials Research*, vol. 216, pp. 661–665, 2011.
- [5] E. Yablonovitch, "Inhibited spontaneous emission in solid-state physics and electronics," *Physical Review Letters*, vol. 58, no. 20, pp. 2059–2062, 1987.
- [6] J. D. Joannopoulos, P. R. Villeneuve, and S. Fan, "Photonic crystals: putting a new twist on light," *Nature*, vol. 386, no. 6621, pp. 143–149, 1997.
- [7] K. B. Chung and S. W. Hong, "Wavelength demultiplexers based on the superprism phenomena in photonic crystals," *Applied Physics Letters*, vol. 81, no. 9, pp. 1549–1551, 2002.
- [8] M. Bayindir, B. Temelkuran, and E. Ozbay, "Photonic-crystal-based beam splitters," *Applied Physics Letters*, vol. 77, article 3902, 2000.
- [9] H. Alipour-Banaei, M. G. Rabati, P. Abdollahzadeh-Badelbou, and F. Mehdizadeh, "Application of self-collimated beams to realization of all optical photonic crystal encoder," *Physica E: Low-Dimensional Systems and Nanostructures*, vol. 75, pp. 77–85, 2016.
- [10] R. Savarimuthu and N. Rangaswamy, "Coupled mode theory analysis for circular photonic crystal ring resonator-based add-drop filter," *Optical Engineering*, vol. 51, no. 11, Article ID 114001, 2012.
- [11] K. V. Shanthi and S. Robinson, "Two-dimensional photonic crystal based sensor for pressure sensing," *Photonic Sensors*, vol. 4, no. 3, pp. 248–253, 2014.
- [12] A. Rostami, F. Nazari, H. A. Banaei, and A. Bahrami, "A novel proposal for DWDM demultiplexer design using modified-T photonic crystal structure," *Photonics and Nanostructures—Fundamentals and Applications*, vol. 8, no. 1, pp. 14–22, 2010.
- [13] W. Liu, D. Yang, H. Tian, and Y. Ji, "Optimization transmission of photonic crystal coupled cavity and design of demultiplexer for wavelength division multiplexing application," *Optical Engineering*, vol. 51, no. 8, Article ID 084002, 2012.
- [14] N. D. Gupta and V. Janyani, "Dense wavelength division demultiplexing using photonic crystal waveguides based on cavity resonance," *Optik—International Journal for Light and Electron Optics*, vol. 125, no. 19, pp. 5833–5836, 2014.
- [15] C.-W. Kuo, C.-F. Chang, M.-H. Chen, S.-Y. Chen, and Y.-D. Wu, "A new approach of planar multi-channel wavelength division multiplexing system using asymmetric super-cell photonic crystal structures," *Optics Express*, vol. 15, no. 1, pp. 198–206, 2007.
- [16] M. R. Rakhshani, M. A. Mansouri-Birjandi, and Z. Rashki, "Design of six channel demultiplexer by heterostructure photonic crystal resonant cavity," *International Research Journal of Applied and Basic Sciences*, vol. 4, no. 4, pp. 976–984, 2013.
- [17] F. Mehdizadeh and M. Soroosh, "A new proposal for eight-channel optical demultiplexer based on photonic crystal resonant cavities," *Photonic Network Communications*, vol. 31, no. 1, pp. 65–70, 2016.
- [18] H. Alipour-Banaei, F. Mehdizadeh, and S. Serajmohammadi, "A novel 4-channel demultiplexer based on photonic crystal ringresonators," *Optik*, vol. 124, no. 23, pp. 5964–5967, 2013.
- [19] H. Tian, G. Shen, W. Liu, and Y. Ji, "Integration of both dense wavelength-division multiplexing and coarse wavelength-division multiplexing demultiplexer on one photonic crystal chip," *Optical Engineering*, vol. 52, no. 7, Article ID 076110, 2013.
- [20] V. R. Balaji, M. Murugan, and S. Robinson, "DWDM demultiplexer using inverted-p photonic crystal structure," *International Journal of Applied Engineering Research (IJAER)*, vol. 10, no. 6, pp. 5688–5692, 2015.
- [21] J. Clerk Maxwell, "A dynamical theory of the electromagnetic field," *Journal of Philosophical Transactions of the Royal Society of London*, vol. 155, no. 1865, pp. 459–512, 2015.
- [22] K. S. Kunz and R. J. Luebbers, *The Finite Difference Time Domain Method for Electromagnetic*, CRC Press, New York, NY, USA, 1993.
- [23] C.-P. Yu and H.-C. Chang, "Yee-mesh-based finite difference eigenmode solver with PML absorbing boundary conditions for optical waveguides and photonic crystal fibers," *Optics Express*, vol. 12, no. 25, pp. 6165–6177, 2004.
- [24] J. Lutkenhaus, D. George, D. Lowell, B. Arigong, H. Zhang, and Y. Lin, "Registering functional defects into periodic holographic structures," *Applied Optics*, vol. 54, no. 23, pp. 7007–7012, 2015.
- [25] K. N. Sediq, D. Coles, P. W. Fry, and D. G. Lidzey, "Plasmonic gold nanodiscs fabricated into a photonic-crystal nanocavity," *Nanotechnology*, vol. 27, no. 22, Article ID 225203, 2016.
- [26] H. Alipour-Banaei and F. Mehdizadeh, "Bandgap calculation of 2D hexagonal photonic crystal structures based on regression analysis," *Journal of Optical Communications*, vol. 34, no. 4, pp. 285–293, 2013.
- [27] N. R. Draper, H. Smith, and E. Pownell, *Applied Regression Analysis*, vol. 3, Wiley, New York, NY, USA, 1966.

Research Article

A Method to Control Dynamic Errors of the Stylus-Based Probing System for the Surface Form Measurement of Microstructures

Hui Fang, Bin Xu, Deqiang Yin, and Shiping Zhao

School of Manufacturing Science and Engineering, Sichuan University, 24 South No. 1 Ring Road, Chengdu 610065, China

Correspondence should be addressed to Bin Xu; bin_xu@outlook.com and Deqiang Yin; deqiang.yin@scu.edu.cn

Received 25 December 2015; Accepted 12 April 2016

Academic Editor: James Piao

Copyright © 2016 Hui Fang et al. This is an open access article distributed under the Creative Commons Attribution License, which permits unrestricted use, distribution, and reproduction in any medium, provided the original work is properly cited.

Dynamic errors of the stylus-based probing system seriously affect the measurement accuracy in surface quality detection on microstructures. A method, which is focused on measuring the surface form of microgears, microholes on the injector nozzle, and so forth, is proposed to control dynamic errors of the stylus-based probing system. Firstly, two kinematical models were built to systematically investigate the dynamic performance of the stylus-based probing system, and the relationship between the measuring force, scanning speed, fidelity, and dynamic errors was described. Then, numerical simulations of the surface form measurement, in which a sine-shaped microstructure was taken as a target surface, were carried out. Results of the numerical simulations reveal that the dynamic errors were affected by the scanning speed and the initial position of the measured specimen. Lastly, a method to control dynamic errors by properly setting up the scanning speed and the initial position of the specimen was proposed for the surface form measurement of microstructures.

1. Introduction

Microstructures, such as microgears and microholes, are widely used in precision industries [1–3]. The working performance of microstructure-based systems and devices is primarily determined by the geometric accuracy of the employed microstructures [4]. It is, therefore, important to carry out high-accuracy surface form measurement of microstructures so that the form accuracy of microstructures can be improved and guaranteed in the manufacturing process. However, due to the fact that many of the microstructures have the characteristics of high-aspect-ratios and steep surface slopes, it is difficult to carry out high-accuracy surface form measurement on microstructures [5–7].

The stylus-based probing system is an important technique for measuring the surface form of microstructures because of the advantages of convenient utilization, insensitivity to surface contaminants, and high measurement accuracy [8–10]. In the authors' previous study, two types of stylus-based profiling systems, one of which has an elastic element and the other one without it, were used to measure the surface

form of gear-shaped microstructures [2, 11]. Measurement results show that it had an obvious form distortion on the top of the measured microstructures and the measurement repeatability got worse on the side flanks. The stylus-based probing system employs a stylus to trace the surface of the target surface, and the spatial position of the stylus tip is recorded and employed to reconstruct the surface form of the target surface. However, the trace of the stylus tip cannot always follow the surface variation of the measurement target, because the motion of the stylus tip is affected by the kinetics of the stylus-based probing system. For instance, the stylus tip separates from the measured surface during scanning process, which is referred to as stylus flight phenomenon.

Over the years, work has been conducted to resolve the issue of stylus flight. Damir proposed a method to choose the suitable spring stiffness of a stylus-based profiling system [12]. Liu et al. developed an active damping control method to modify a stylus instrument and confirmed that the stylus instrument could get better working performance while the damping factor was in the region between 0.5 and 0.7 [8], which meets the research results of Whitehouse [13, 14].

McCool pointed out that the reconstructed profile deduced from the stylus profile traces was distorted by the nonlinear filtering effect of the finite stylus tip and by the failure at high enough tracing speeds of the stylus to maintain contact with the profile being traced [15]. Pawlus et al. discussed the influence of the stylus flight on change of surface topography parameters [10, 16]. Liu and Tian et al. built dynamic models, which took the Hertzian contact and nonlinear damping forces into consideration, to analyse the stylus flight phenomenon [9, 17, 18]. The above approaches focused on the modification of hardware of the stylus instrument, such as modifications of the damping factor, spring stiffness, and the mass of a stylus. The modification of hardware would cause high costs in economy and technology. Therefore, a simple and cost-effective method to depress the stylus flight is desired in precision engineering.

This paper presents a method to control dynamic errors of the stylus-based probing system for the surface form measurement of microstructures. Firstly, two kinematical models were built to systematically investigate the dynamic performance of the stylus-based probing system, and relevant theoretical work was given in detail. Then, numerical simulations of the surface form measurement were carried out while taking a sine-shaped microstructure as a target surface. Lastly, a method was proposed to control the dynamic errors on the surface form measurement of microstructures.

2. Kinematical Model of the Stylus-Based Probing System

The stylus-based probing system employs a stylus to traverse the target surface. The vertical position of the stylus changes following the variation of the target surface, and it is measured by a displacement sensor. The output of the displacement sensor, the position variation of the stylus in vertical direction, is employed to reconstruct the surface form for the measurement specimen. However, the vertical position of the stylus cannot always exactly follow the variation of the measured surface in the region with steep slopes and huge slope variations, which results in form distortion and is known as the stylus flight phenomenon as shown in Figure 1(a).

Typical stylus-based probing systems have the types of lever mechanism, flexure hinge mechanism, and the air-bearing mechanism according to how the stylus is supported [2, 9] and can be generally modelled by a second-order kinematical system as shown in Figure 1(b). In this kinematical system, the vertical position of the stylus is denoted by y , which is subjected to the measured surface form y_s and crucial parameters of the stylus-based probing system. Neglecting the friction force between the stylus tip and the measured surface for clarity, the equation of the stylus motion can be expressed as follows:

$$-mg - m\ddot{y} - ky - c\dot{y} + F = 0, \quad (1)$$

where m is the equivalent mass of the stylus-based probing system, g is the gravitational acceleration, k is the spring stiffness, c is the damping coefficient, \dot{y} and \ddot{y} are the velocity

and acceleration of the stylus motion along the Y -direction, and F is the measuring force, namely, the interaction force between the stylus tip and the measured surface. The surface scanning is carried out along the X -direction with a speed v . The Y -direction is aligned to the direction of the gravity, and the origin O of Y coordinate is the position of the stylus tip while the spring is not stretched. The position A is assumed to be the position where the spring is stretched by its gravity and the zero point of the probe sensing. The distance of the average height of the measured surface to the zero point of the probe sensing, position A , is defined to be the initial position of the measured surface.

In the surface scanning process, the stylus tip always contacts with the measured surface while the stylus flight phenomenon does not occur. Under this condition, the measuring force should be greater than zero. Therefore, the measuring force F is an important parameter to represent the dynamic behavior of the stylus-based probing system. Then, (1) is rearranged as

$$F = m\ddot{y} + c\dot{y} + ky + mg. \quad (2)$$

In the case that the stylus flight phenomenon does not occur, which means that the stylus tip is contacting with the measured surface, the stylus motion follows the variation of the measured surface. Therefore, the velocity and the acceleration of the stylus motion are equal to those of the variation of the measured surface, which are expressed by the following equation:

$$\begin{aligned} \dot{y} &= \dot{y}_s \\ \ddot{y} &= \ddot{y}_s, \end{aligned} \quad (3)$$

where y_s is the measured surface. Assuming the measured surface is of a form of $y_s = f(x)$, (3) becomes

$$\begin{aligned} \dot{y} &= \dot{x}f'(x) \\ \ddot{y} &= (\dot{x})^2 f''(x), \end{aligned} \quad (4)$$

where \dot{x} is equal to the scanning speed v , $f'(x)$ is the slope ρ of the measured surface, and $f''(x)$ is the variation of the surface slope and is denoted by $\dot{\rho}$. Therefore, the measuring force expressed by (2) is rewritten as

$$F = mv^2\dot{\rho} + cv\rho + kf(x) + mg. \quad (5)$$

While the stylus tip contacts with the measured surface, F should be greater than zero, which is expressed as

$$F = v^2\dot{\rho} + 2\xi\omega v\rho + \omega f(x) + g > 0, \quad (6)$$

where $\xi = c/2\sqrt{km}$ is the damping ration and $\omega = \sqrt{k/m}$ is the resonant frequency of the stylus-based probing system. In order to guarantee that the measuring force is greater than zero, the general solutions are to improve the resonant frequency ω , adjust the damping ration ξ , and reduce the scanning speed v .

The methods to improve the resonant frequency ω are the increase of spring stiffness k and the reduction of equivalent

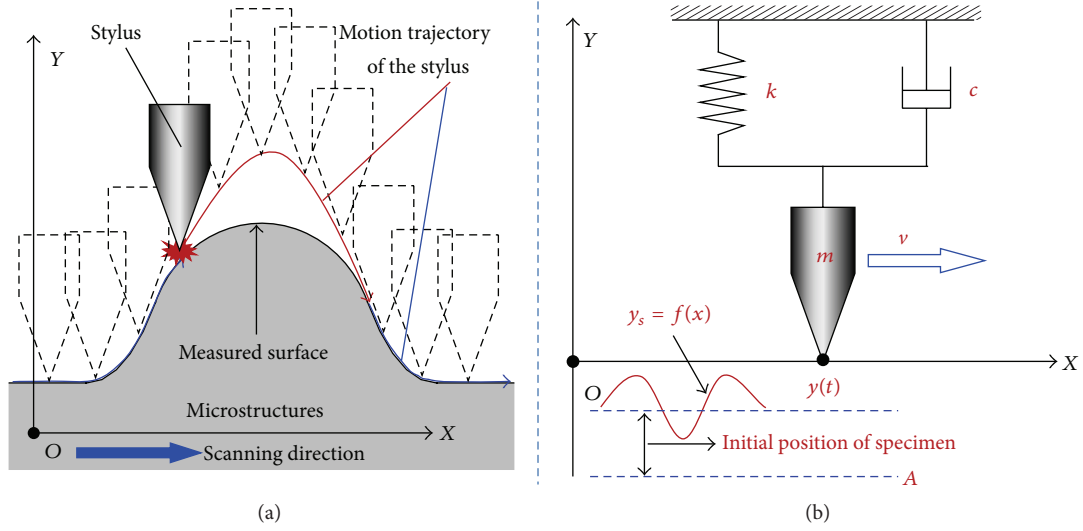


FIGURE 1: (a) Schematic of the stylus flight. (b) Kinematical model of the stylus-based probing system.

mass m . The increase of the spring stiffness k would increase the measuring force F , which possibly results in the damage of the measured surface. On the other hand, the equivalent mass m also cannot be reduced without limitation, because the geometric parameters of the stylus should meet the requirement of functional requirements. As shown in (6), the effect on the measuring force F is relevant to the surface slope ρ . If the surface slope ρ is positive, it is better that the damping ration ξ be greater; otherwise, it should be smaller. It should be mentioned that the slope ρ of the measured surface has the potential to be distributed from negative to positive. Therefore, it is hard to realize an appropriate adjustment of the damping ration ξ , or the appropriate adjustment would result in the increase of costs in economy and technology. The effect of the scanning speed v to the measuring force F is the function of the surface slope ρ and its variation $\dot{\rho}$. Generally, it is believed that a better measurement result can be obtained at a slower scanning speed. However, the slower scanning speed would lead to the reduction of work efficiency.

In this case the stylus flight phenomenon occurs, which means the stylus tip is out of contact with the measured surface. In this condition, the measuring force is reduced to zero and the stylus motion is free oscillation. Figure 2 illuminates the kinematical model of the stylus flight. Assuming that the stylus separates from the measured surface on the point $P_0(x_{P_0}, y_{P_0})$ with a vertical speed v_{P_0} , the time on this moment is set to zero for clarity. The vertical position y_{P_t} of the stylus is a time-varying quantity and it is the solution of (7), which is derived from (2). Consider

$$\ddot{y} + \frac{c}{m}\dot{y} + \frac{k}{m}y = -g. \quad (7)$$

Equation (7) is linear and of second order with a constant coefficient. The general solution is

$$y = e^{\alpha t} [C_1 \cos \beta t + C_2 \sin \beta t], \quad (8)$$

where $\alpha = -c/2m$ and $\beta = \sqrt{4km - c^2}/2m$. To (8), the characteristic equation is expressed as

$$r^2 + \frac{c}{m}r + \frac{k}{m} = 0. \quad (9)$$

Due to $c < 2\sqrt{km}$, the solution to this characteristic equation is

$$r_{1,2} = -\frac{c}{2m} \pm i * \frac{\sqrt{4km - c^2}}{2m}. \quad (10)$$

To (8), the general solution can be expressed as follows:

$$y_1 = e^{-(c/2m)t} \left[C_1 \cos \frac{\sqrt{4km - c^2}}{2m} t + C_2 \sin \frac{\sqrt{4km - c^2}}{2m} t \right]. \quad (11)$$

To (8), the particular solution is

$$y_2 = -\frac{mg}{k}. \quad (12)$$

The solution to (8) can be derived from (11) and (12) and expressed as follows:

$$y = e^{-(c/2m)t} \left[C_1 \cos \frac{\sqrt{4km - c^2}}{2m} t + C_2 \sin \frac{\sqrt{4km - c^2}}{2m} t \right] - \frac{mg}{k}. \quad (13)$$

The initial condition of (13) is that $y = y_{P_0}$ and $dy/dt = v_{P_0}$ while $t = 0$. Substituting this initial condition into (13), the parameters C_1 and C_2 can be found. Consider

$$\begin{aligned} C_1 &= \frac{mg}{k} + y_{P_0} \\ C_2 &= \frac{2mv_{P_0} + mgc/k + cy_{P_0}}{\sqrt{4km - c^2}}. \end{aligned} \quad (14)$$

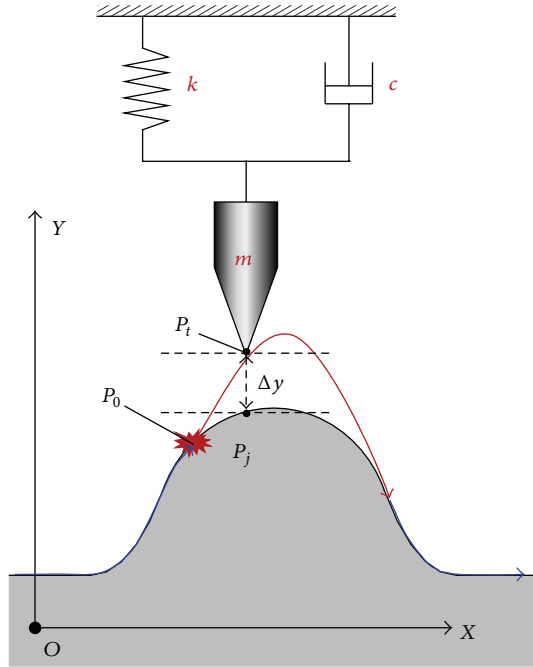


FIGURE 2: Kinematical model of the stylus flight.

Then, (13) can be rewritten as

$$y = e^{-(c/2m)t} \left[\left(\frac{mg}{k} + y_{P_0} \right) \times \cos \frac{\sqrt{4km - c^2}}{2m} t + \left(\frac{2mv_{P_0} + mgc/k + cy_{P_0}}{\sqrt{4km - c^2}} \right) \sin \frac{\sqrt{4km - c^2}}{2m} t \right] - \frac{mg}{k}. \quad (15)$$

Equation (15) gives out the motion of the stylus while the stylus flight occurs.

3. Numerical Simulation and Analysis of Dynamic Performance

3.1. Effect of Measurement Setup on Dynamic Performance. The parameters of the stylus-based probing system and the measurement setup affect the dynamic performance (e.g., fidelity, measuring force, and dynamic errors), which were analysed by numerical simulations based on the kinematical model expressed by (1). In the numerical simulations, the parameters of a practical stylus-based probing system were employed and given as $m = 3.5 \text{ g}$, $k = 2.7 \text{ N/m}$, and $c = 0.00144 \text{ Nsm}^{-1}$ [19]. A sine-shaped microstructure expressed by (16) with amplitude of $200 \text{ }\mu\text{m}$ and period of $100 \text{ }\mu\text{m}$ was used as the measurement specimen. The interval of the measured surface discretization was set to $0.1 \text{ }\mu\text{m}$, and the scanning interval was set to $1 \text{ }\mu\text{m}$. Consider

$$y_s = 200 \times \cos \left(\frac{x \times \pi}{50} \right) - b, \quad (16)$$

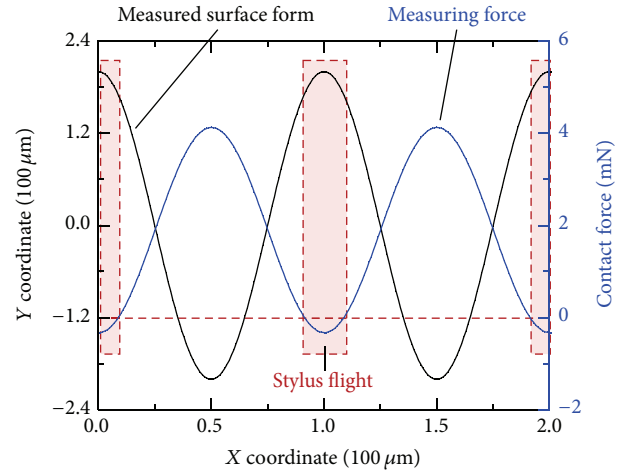


FIGURE 3: Measured surface form and the measuring force.

in which the unit is micrometer and the parameter b is used to simulate the initial setup of the specimen's position. The stylus tip is stretched 12.7 mm below the x -axis by its gravity, where it was assumed to be the zero point of the displacement sensing of the stylus-based probing system. If the parameter b is 12×10^3 , the distance of the measured form to the zero point of the displacement sensing is 0.7 mm .

Firstly, the fidelity of form measurement, which means how much of the measured surface could be exactly measured without the stylus flight phenomenon, was investigated by the numerical simulation. The scanning speed c was set to 1 mm/s and the initial position of the measured surface was set to 0.7 mm . The kinematical model expressed by (6) about the measuring force was utilized to detect whether the stylus flight phenomenon occurred or not. Figure 3 shows the simulation results. The curve of the measuring force, which is plotted by the raw output of (6), presents a sine shape and has a phase difference of π to the measured surface form. The values of the measuring force distribute from -0.32 mN to 4.12 mN . In practice, the measuring force cannot be smaller than zero. The region marked by red blocks, where the measuring force is negative, indicates that the stylus flight occurred in the region near the peak of the measured form. In this case, 82.79% of the measured surface can be exactly measured.

The influence of the surface geometrical characteristic to the stylus flight was analysed in Figure 4. In this figure, the surface slope and the rate of slope variation were drawn according to their X coordinates, and the region of the stylus flight was covered by red blocks. It can be found that the rate of slope variation has a strong impact on the stylus flight compared to the surface slope, which means that the stylus tip usually lost contact in the region with a huge slope variation.

The effect of the scanning speed on the measuring force and the fidelity was investigated by changing the speed from 0.01 mm/s to 4 mm/s , of which the result was shown in Figure 5. In this figure, the black curve is plotted by the maximum value of the measuring force at each scanning speed, and the red one is plotted by the fidelity at each

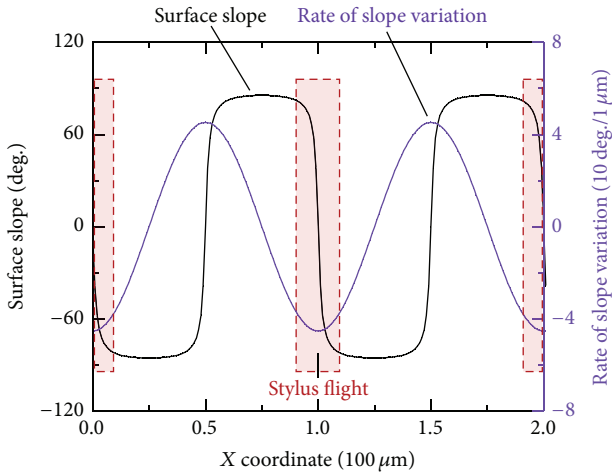


FIGURE 4: Effect of the surface slope and rate of slope variation on stylus flight.

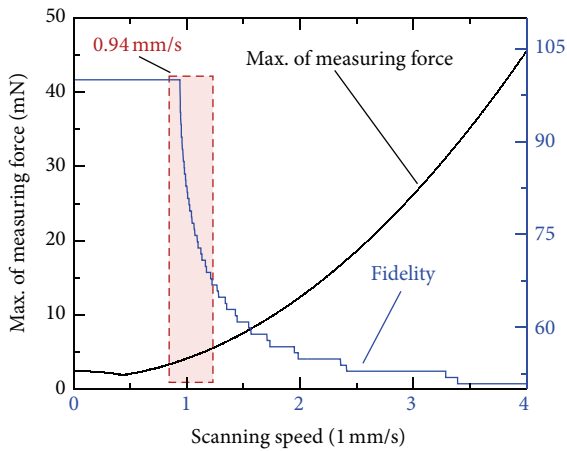


FIGURE 5: Effect of the scanning speed on dynamic performance.

scanning speed. The results show that while the scanning speed exceeded 0.94 mm/s, the fidelity would be rapidly falling and the measuring force would be rising up very fast.

The initial position of the measured specimen is another crucial factor to affect the dynamic performance. Therefore, the distance of the measured specimen to the zero point of displacement sensing was set from 0.2 mm to 0.7 mm and was used as a variable in the numerical simulation. The relation of the specimen's initial position with the measuring force and the fidelity is shown in Figure 6. As shown in the figure, while the initial position is increasing, both the measuring force and the fidelity are increasing. However, it should be known that the measuring force is generally expected to be in the region of few micronewtons.

3.2. Effect of Measurement Setup on Dynamic Error. Higher scanning speed and lower measuring force are desired in practical measurement tasks. However, both the increase of scanning speed and the reduction of the measuring force could potentially result in stylus flight, which would

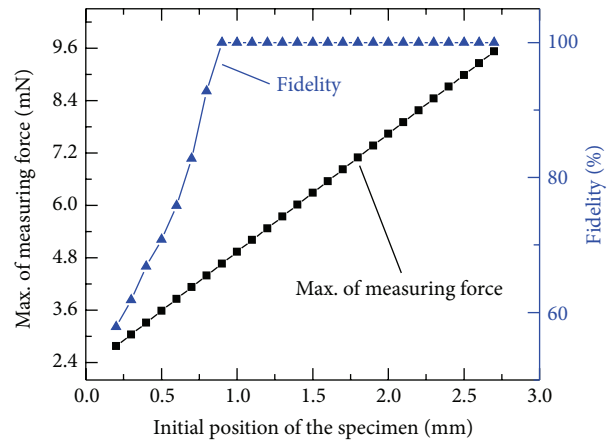


FIGURE 6: Effect of the initial position of the specimen on dynamic performance.

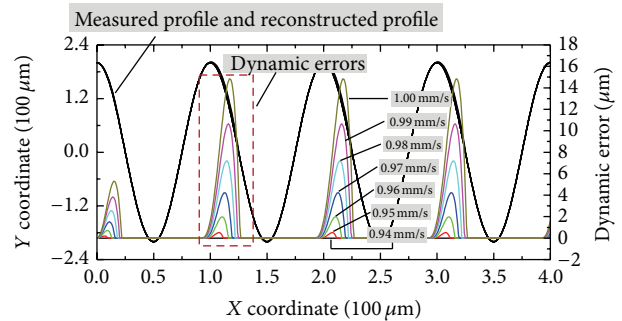


FIGURE 7: Effect of scanning speed (0.94 mm/s to 1 mm/s) on dynamic errors.

introduce dynamic errors into measurement results. The above numerical simulation method was also used to analyse the effect of measurement setup on dynamic errors. There is only one difference, which is that the motion trace of stylus tip was computed by (15), and the initial condition was obtained from (5). The motion trace of the stylus tip in whole scanning process was the measurement results, which was used to reconstruct the surface form for the measured profile. The difference of the reconstructed profile and the measured profile was seen as the dynamic errors introduced by the stylus flight.

Figure 5 indicates that while the scanning speed exceeded 0.94 mm/s, the stylus flight would occur. Therefore, the scanning speed was set from 0.94 mm/s to 1.00 mm/s with an interval of 0.01 mm/s, and the initial position of the measured specimen was set to 0.7 mm. The results of the numerical simulation are shown in Figure 7. The reconstructed profiles at each scanning speed and the measured profile are covered with each other due to their small differences. The dynamic errors increase from smaller than 1 μm to about 15 μm. The increase ratio is approximately 3 μm per 0.01 mm/s. The region marked by a red block in this figure indicates that the position with the maximum dynamic errors is not exactly on the peaks of the measured microstructures. In this case, the position with the maximum dynamic errors slightly passed

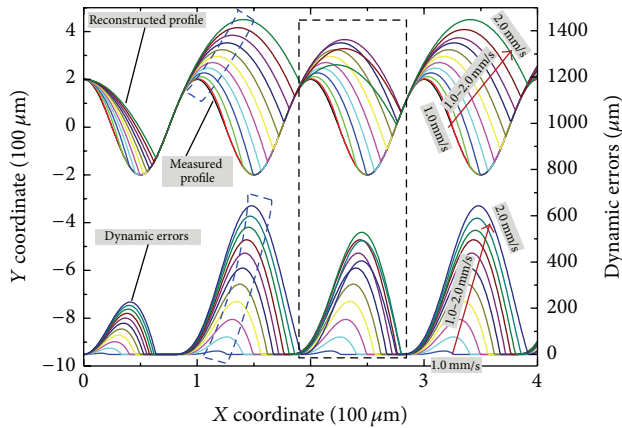


FIGURE 8: Effect of scanning speed (1 mm/s to 2 mm/s) on dynamic errors.

over the peaks. The other feature that should be mentioned is that the dynamic errors present periodic features expect in the first period of the measured surface. This is because the initial condition of the stylus flight is different; namely, the separation position and the vertical speed of stylus tip differ.

The effect of the scanning speed on the dynamic errors was studied on a larger scale, 1.00 mm/s to 2.00 mm/s, and the results are shown in Figure 8. The dynamic errors sharply increased from 15 μm to about 650 μm , which would be out of the acceptable error range. The feature of the dynamic errors on the third period of the measured surface does not completely repeat with it on the second period. This is because the separation position of the stylus tip changed after a serious stylus flight. But this feature is repeated over two periods of the measured profile.

The initial position of the measured specimen is also very important and seriously affects the dynamic errors. In the numerical simulation, the initial position of the measured specimen was set from 0.1 mm to 0.6 mm while the scanning speed remained 1 mm/s. The measurement results and corresponding dynamic errors at different initial position are shown in Figure 9. While the initial position was increasing, the dynamic errors obviously reduced from about 250 μm to smaller than 1 μm . Comparing the results shown in Figures 7–9, the curve shape of dynamic errors presents a subtle asymmetry that the dynamic errors on the flank side against the stylus scanning motion are obviously greater than on another side.

4. Control Method of Dynamic Errors

The above numerical simulation and analysis reveals that the measurement setup (i.e., scanning speed and the initial position of the specimen) should be properly chosen. Otherwise, excessive measuring force would make the stylus damage the measured surface, and unacceptable dynamic errors would reduce the reliability of the measurement results. The method to control the dynamic errors into the acceptable range was proposed based on the prediction of dynamic errors and the measuring force. Firstly, the surface scanning is simulated

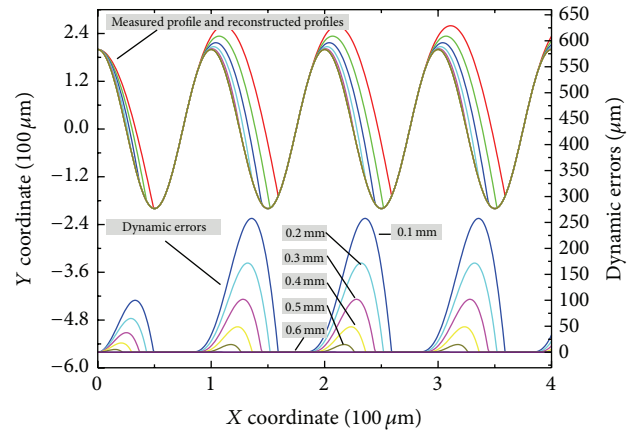


FIGURE 9: Effect of initial position on dynamic errors.

by the method introduced in Section 3.2, and the measuring force is analysed by the method introduced in Section 3.1. The maximum values of the dynamic errors and the measuring force are recorded as a set of data. Then change the values of the scanning speed and the initial position of the specimen; step 1 is repeated and more sets of data are acquired. All the obtained sets of data present the relationship graph between the dynamic performance and the measurement setup. Lastly, the optimized selections of the scanning speed and the initial position of the specimen can be carried out from the relationship graph according to the requirements about the dynamic errors and the measuring force of a measurement task.

The sine-shaped microstructure with steep slopes expressed by (16) was employed by the numerical simulation to verify the proposed method. The scanning speed was set from 0.93 mm/s to 2.00 mm/s, and the initial position of the specimen was set from 0.3 mm to 0.9 mm. The relationship graph between the dynamic performance and the measurement setup was plotted in Figure 10. Assume that the measurement task requires that the dynamic errors should be smaller than 10 μm and the measuring force should be smaller than 5 mN. Then, Figure 10 was reprocessed with a limitation of the 10 μm dynamic errors and was shown in Figure 11. The scale of the colour bar was redefined to easily get more details of the measuring force. The regions of the scanning speed and the initial position of the specimen would be the choice which would make the measurement result meet the requirements of the measurement task. In addition, the best measurement setup would be 1.1 mm/s scanning speed and 0.9 mm initial position for higher measurement efficiency.

5. Conclusion

In order to enhance the form measurement accuracy of microstructures such as microgears and microholes on the injector nozzle, research on the dynamic feature of stylus-based probing systems has been carried out in this paper. Results of numerical simulations reveal that the rate of the

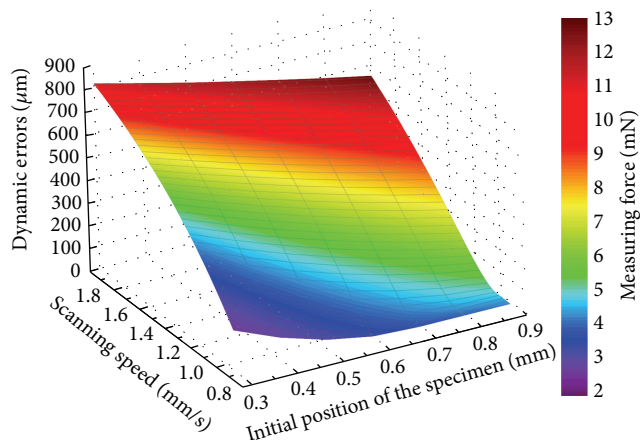


FIGURE 10: Relationship graph between the dynamic performance and the measurement setup.

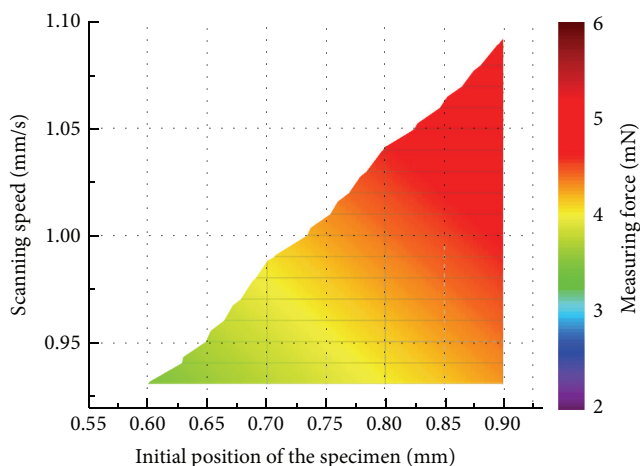


FIGURE 11: Optimized selections of the measurement setup.

slope variation of the measured surface greatly affects the dynamic performance of the stylus-based probing system. Furthermore, it is hard to control the dynamic performance by decreasing scanning speed and increasing spring stiffness due to requirements on measurement efficiency and measuring force. Afterwards, a simple and cost-effective method to control the dynamic performance has been proposed without changing the hardware of the stylus-based probing system. This method employs kinematical models to predict the influence of the measurement setup on dynamic performance, and then the optimal scanning speed and the initial position of the measured sample can be selected according to requirements on measurement efficiency and measuring force.

It should be noted that the proposed method did not take adhesion, friction, and elastic deformation into consideration and the constructed dynamic model is two-dimensional. These issues remain to be investigated by future work.

Competing Interests

The authors declare that they have no competing interests.

Acknowledgments

This work is supported by the National Natural Science Foundation of China (Grant nos. 51405314, 11302141, and 61006403), by the Fundamental Research Funds for the Central Universities (Grant no. 2015SCU04A12), and by the LPMT, CAEP (Grant no. KF15004).

References

- [1] H. N. Hansen, K. Carneiro, H. Haitjema, and L. De Chiffre, "Dimensional micro and nano metrology," *CIRP Annals—Manufacturing Technology*, vol. 55, no. 2, pp. 721–743, 2006.
- [2] E. Peiner, M. Balke, and L. Doering, "Form measurement inside fuel injector nozzle spray holes," *Microelectronic Engineering*, vol. 86, no. 4–6, pp. 984–986, 2009.
- [3] B. Xu, Y. Shimizu, T. Takeishi, S. Ito, and W. Gao, "Surface form measurement and analysis of a cylindrical workpiece with microstructures," *Journal of Advanced Mechanical Design, Systems and Manufacturing*, vol. 6, no. 6, pp. 936–948, 2012.
- [4] B.-F. Ju, Y.-L. Chen, W. Zhang, and F. Z. Fang, "Rapid measurement of a high step microstructure with 90° steep sidewall," *Review of Scientific Instruments*, vol. 83, no. 1, Article ID 013706, 2012.
- [5] M. B. Bauza, S. C. Woody, B. A. Woody, and S. T. Smith, "Surface profilometry of high aspect ratio features," *Wear*, vol. 271, no. 3–4, pp. 519–522, 2011.
- [6] J. D. Claverley and R. K. Leach, "A vibrating micro-scale CMM probe for measuring high aspect ratio structures," *Microsystem Technologies*, vol. 16, no. 8–9, pp. 1507–1512, 2010.
- [7] H. Fang, B. Xu, W. Chen, H. Tang, and S. Zhao, "A slope-adapted sample-tilting method for profile measurement of microstructures with steep surfaces," *Journal of Nanomaterials*, vol. 2015, Article ID 253062, 8 pages, 2015.
- [8] X. Liu, D. G. Chetwynd, S. T. Smith, and W. Wang, "Improvement of the fidelity of surface measurement by active damping control," *Measurement Science & Technology*, vol. 4, no. 12, pp. 1330–1340, 1993.
- [9] Y. Tian, X. Liu, D. G. Chetwynd, V. Eichhorn, S. Fatikow, and D. Zhang, "Nonlinear viscoelastic modelling of stylus probing for surface metrology," *Precision Engineering*, vol. 37, no. 3, pp. 711–720, 2013.
- [10] P. Pawlus and M. Śmieszek, "The influence of stylus flight on change of surface topography parameters," *Precision Engineering*, vol. 29, no. 3, pp. 272–280, 2005.
- [11] B. Xu, Y. Shimizu, S. Ito, and W. Gao, "Surface profile measurement of internal micro-structures," *International Journal of Precision Engineering and Manufacturing*, vol. 14, no. 9, pp. 1535–1541, 2013.
- [12] M. N. H. Damir, "Error in measurement due to stylus kinematics," *Wear*, vol. 26, no. 2, pp. 219–227, 1973.
- [13] D. J. Whitehouse, "Dynamic aspects of scanning surface instruments and microscopes," *Nanotechnology*, vol. 1, no. 1, pp. 93–102, 1990.
- [14] D. J. Whitehouse, "Enhancement of instrument and machine capabilities," *Nanotechnology*, vol. 7, no. 1, pp. 47–51, 1996.
- [15] J. I. McCool, "Assessing the effect of stylus tip radius and flight on surface topography measurements," *Journal of Tribology, Transactions of the ASME*, vol. 106, no. 2, pp. 202–209, 1984.
- [16] J. F. Song and T. V. Vorburger, "Stylus flight in surface profiling," *Journal of Manufacturing Science and Engineering*, vol. 118, p. 11, 1996.

- [17] Y. Tian, X. Liu, D. G. Chetwynd, B. Shirinzadeh, and D. Zhang, "Vibration analysis of stylus instrument for random surface measurement," *Precision Engineering*, vol. 34, no. 3, pp. 586–591, 2010.
- [18] Y. Tian, X. Liu, D. Zhang, and D. G. Chetwynd, "Dynamic modelling of the fidelity of random surface measurement by the stylus method," *Wear*, vol. 266, no. 5-6, pp. 555–559, 2009.
- [19] K.-W. Lee, Y.-J. Noh, W. Gao et al., "Experimental investigation of an air-bearing displacement sensor for on-machine surface form measurement of micro-structures," *International Journal of Precision Engineering and Manufacturing*, vol. 12, no. 4, pp. 671–678, 2011.

Research Article

Nanostructural Effect of ZnO on Light Extraction Efficiency of Near-Ultraviolet Light-Emitting Diodes

Young Jae Park,¹ Hyounsuk Song,¹ Kang Bok Ko,¹ Beo Deul Ryu,¹
Tran Viet Cuong,^{1,2} and Chang-Hee Hong¹

¹*School of Semiconductor and Chemical Engineering, Semiconductor Physics Research Center, Chonbuk National University, 20 Geonji-ro, Deokjin-gu, Jeonju-si 54907, Republic of Korea*

²*NTT Hi-Tech Institute, Nguyen Tat Thanh University, 298-300 A Nguyen Tat Thanh Street, Ho Chi Minh City, Vietnam*

Correspondence should be addressed to Tran Viet Cuong; tvuong@ntt.edu.vn and Chang-Hee Hong; chhong@jbnu.ac.kr

Received 1 December 2015; Accepted 17 February 2016

Academic Editor: Takuya Tsuzuki

Copyright © 2016 Young Jae Park et al. This is an open access article distributed under the Creative Commons Attribution License, which permits unrestricted use, distribution, and reproduction in any medium, provided the original work is properly cited.

The effect of ZnO nanostructures on the light output power of 375 nm near-ultraviolet light-emitting diodes (NUV-LEDs) was investigated by comparing one-dimensional (1D) nanorods (NR-ZnO) with two-dimensional (2D) nanosheets (NS-ZnO). ZnO nanostructures were grown on a planar indium tin oxide (ITO) by solution based method at low temperature of 90°C without degradation of the forward voltage. At an injection current of 100 mA, the light output efficiency of NUV-LED with NR-ZnO was enhanced by around 30% compared to the conventional NUV-LEDs without ZnO nanostructures. This improvement is due to the formation of a surface texturing, resulting in a larger escape cone and a multiple scattering for the photons in the NUV-LED, whereas the light output efficiency of NUV-LED with NS-ZnO was lower than that of the conventional NUV-LEDs due to the internal reflection and light absorption in the defective sites of NS-ZnO.

1. Introduction

An attempt to improve the performance of AlGaIn based near-ultraviolet light-emitting diodes (NUV-LEDs) has attracted much attention due to their great potential for applications such as water purification, biochemical detection, and being a source for white Hg-free lamps [1–3]. However, UV-LEDs have suffered from low external quantum efficiency due to high electrical activation energy for Mg-doped *p*-GaIn, low optical transmittance of transparent conductive layers, and low internal quantum efficiency. Several studies have reported improving the crystal quality of AlGaIn by using AlN interlayer [4, 5] and AlN/AlGaIn superlattices to enhance the optoelectrical performance of the NUV-LED, and using modified graphene [6, 7]. However, these researches only focused on the improvement of the crystal quality and have a large turn-on voltage with inefficient current spreading. An increase in the light extraction efficiency of NUV-LED without degradation of electrical properties is rarely discussed. One of the challenges

which need to be overcome is the low light extraction efficiency, owing to the high internal reflection and narrow escape cone ($\sim 23.6^\circ$) due to the large difference of refractive indexes between nitride material ($n_{\text{GaIn}} = 2.5$) and air ($n_{\text{air}} = 1$). In the past decade, several methods have been proposed for releasing the photons trapped inside the LEDs, including flip-chip LEDs [8], photonic crystals [9], and surface roughening [10, 11]. However, these methods involve complex, costly, long fabrication and dry etching process which may result in degradation of the electrical properties due to surface damage [12]. Alternatively, our previous study revealed that light extraction can be enhanced without degradation of electrical properties by using an aqueous solution method to grow ZnO nanostructures on top of LEDs. The use of ZnO nanostructures not only significantly increases the escape cones since the well-matched refractive indexes between ZnO and GaIn materials but also allows emitted photons to escape through sidewall and rough surface due to surface scattering at the interface. Although aqueous solution is considered a facile, scalable, low

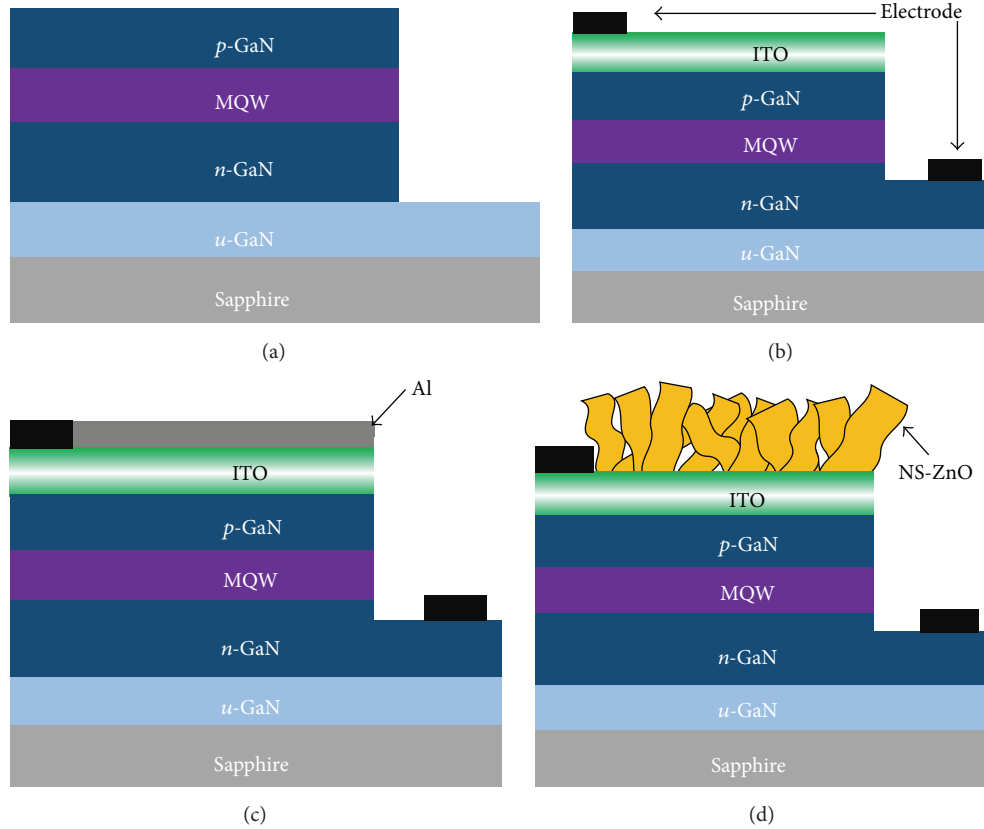


FIGURE 1: Schematic diagram of the process flow: (a) mesa etching after the UVLED structure growth on sapphire substrate, (b) deposition of bonding metal electrode after deposition of ITO layer onto p -GaN, (c) selective deposition of thin Al layer on the ITO area using a photolithography, and (d) ZnO nanostructure growth by a hydrothermal method.

temperature, and cost effective method, difficulties in controlling crystalline structure and morphology are the main obstacles to realizing this approach. It is believed that elucidating the effect of nanostructure morphology on light extraction efficiency of LED devices is very important for the development of NUV-LEDs with high luminance efficiency. In this work, two different nanostructures of ZnO, nanorods (NR) and nanosheets (NS), have been employed to investigate their effect on light extraction efficiency of NUV-LED devices.

2. Experimental

Figure 1 shows the schematic diagram of the processes for fabricating the UVLED with ZnO nanostructures. ZnO nanostructures were formed onto ITO films deposited on NUV-LED structures. The NUV-LED structure was grown on a 2 in. diameter c -plane sapphire substrate using metal organic chemical vapor deposition. Trimethylgallium (TMGa) and trimethylaluminum (TMAl) were used as Ga and Al metal organic precursors, and ammonia (NH_3) was used as a nitrogen source. Bis(cyclopentadienyl) magnesium (Cp_2Mg) and silane (SiH_4) were employed for p -type and n -type dopant sources, respectively. The device structure is p -GaN (0.15 μm)/AlGaIn electron blocking layer/a 5-period InGaIn/AlGaIn multiple quantum wells (MQWs)/ n -GaN

(2 μm)/undoped GaN/sapphire. After mesa etching, a 100 nm ITO layer was deposited onto p -GaN by e-beam evaporation and was annealed at 500°C for 30 sec under $\text{N}_2:\text{O}_2$ (8:2) mixed ambient. The bonding pad electrodes of Cr/Au (30/250 nm) were deposited onto the top surface of the ITO transparent electrode and n -type GaN by e-beam evaporation. We fabricated InGaIn/AlGaIn MQW NUV-LEDs with conventional planar ITO (C-LED), ZnO nanorod array/ITO (NR-LED), and ZnO nanosheet array/ITO (NS-LED). To realize ZnO nanostructures on an ITO electrode, the ITO area of the p -electrode was made open by a photoresist lift-off process. NR- and NS-ZnO were formed by a hydrothermal growth method. This method creates the nanostructures by using an aqueous solution at 90°C on the transparent contact layer of ITO. The solution to grow the ZnO nanorods (NR-ZnO) and ZnO nanosheets (NS-ZnO) is described in detail elsewhere [13].

The morphologies and structures of the ZnO nanostructures arrays were characterized via scanning electron microscopy (SEM, S-4700, Hitachi, Japan). The optical properties were investigated using photoluminescence spectra with a He-Cd excited source (325 nm), and light output power measured as a function of applied current (L - I) was carried out using an optical detector connected to a parameter analyzer. The current-voltage (I - V) characteristics were

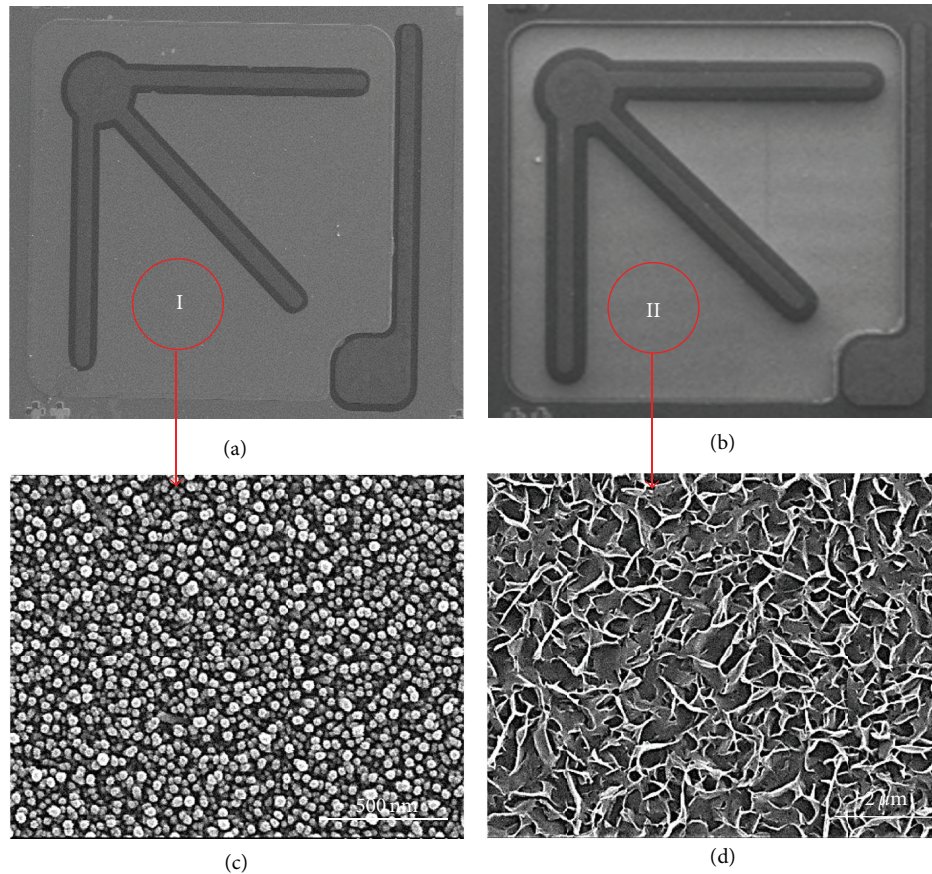


FIGURE 2: Top-view SEM images of ((a)-(b)) electrode pad configuration of NR-LED and NS-LED with two defined areas (c) and (d), respectively.

measured using a semiconductor characterization system (Keithley 4200-MSTech).

3. Results and Discussion

Figure 2 indicates that the ZnO nanostructures are well defined and grown on top of NUV-LED structures via hydrothermal growth method. In order to realize NR-ZnO on the ITO layer selectively, a conventional photolithography technique was performed to make the ITO layer open except the electrodes. A synthesized Ga-doped ZnO (GZO) solution [13] was spin-coated onto the substrate at 3000 rpm for 20 s to form a GZO buffer layer. The GZO buffer layer coated substrate was then annealed at 350°C in air for 60 min to form a seed layer for NR-ZnO. To grow NS-ZnO, a 10 nm thick Al was deposited onto ITO layer using e-beam evaporation. The NR-ZnO on GZO seeds and the NS-ZnO on Al thin film were grown by a dipping and holding process into a mixed solution containing DI water, 18 mM zinc nitrate hexahydrate, and 20 mM hexamethylenetetramine for 90 min at 90°C.

Figures 2(a) and 2(b) show a plan-view optical micrograph of the NR- and NS-LED, respectively. The ZnO nanostructures were selectively grown on ITO surface area as shown in regions I and II. In addition, clear pattern of Cr/Au electrode pad as well as ITO transparent conductive layer was

also observed. The distinct surface morphologies of NR and NS are clearly exhibited in Figures 2(c) and 2(d). Figure 2(c) shows the typical SEM image of single crystalline NR-ZnO with orientation preferably vertical to the ITO surface. The length and the diameter of the nanorods are in the range of 40–50 and 200–250 nm, respectively. Figure 2(d) shows the NS-ZnO structure on ITO layer. The nanosheets have a length of about 500 nm. The two-dimensional growth of NS-ZnO is formed as a result of the Al element. The Al film deposited onto ITO layer had been incorporated into ZnO during hydrothermal reaction process and suppressed the growth along [001] direction. The primary reason is that the Al atom inhibited the growth rate of the polar surface by adsorbing; therefore, the growth rate of the nonpolar surface is faster than that of the polar surface [14].

Figure 3(a) shows UV-Vis spectra of the ITO, NS-ZnO, and NR-ZnO. The optical transmittance of LEDs devices in visible range does not degrade after fabricating ZnO nanostructures on top of the devices. The enhanced transmittance of NS- and NR-ZnO is mainly due to the formation of the nanotexturing surface. Rougher surface changed the light trajectory in a chaotic fashion, and the optical phase-space distribution turned into ergodic, resulting in improvement of the light transmittance. These results are in good agreement with previous study on textured ITO/ZnO surface [15]. It

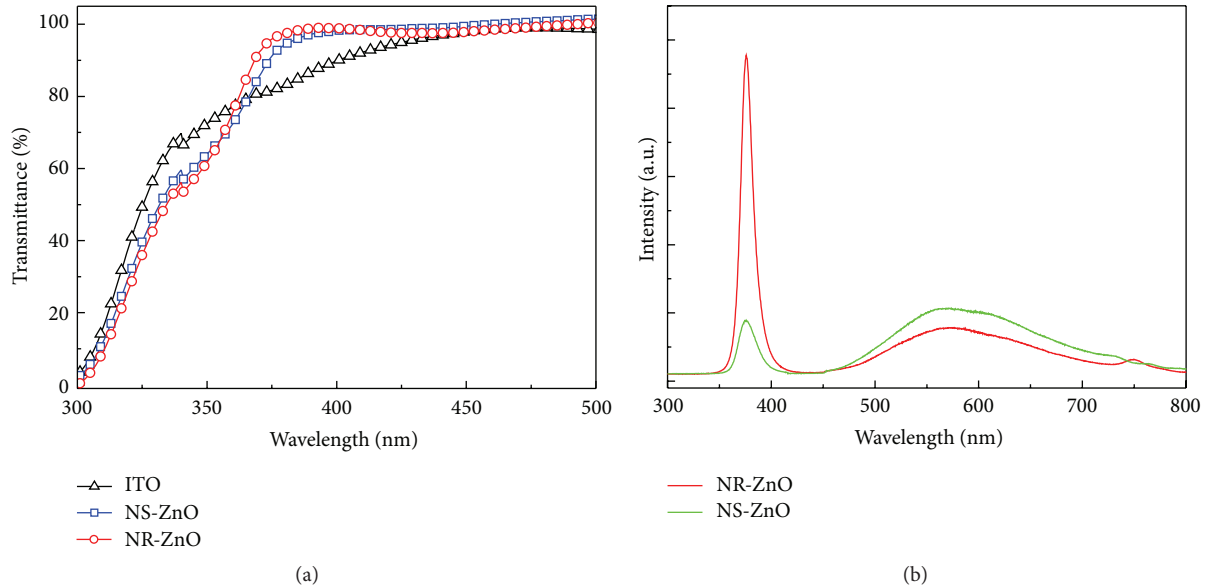


FIGURE 3: (a) UV-Vis and (b) PL spectra of NR-ZnO and NS-ZnO.

should be noted that the transmittance of NR-ZnO is slightly higher than that of NS-ZnO at NUV range (375 nm). On the other hand, the lower transmittance of NS-ZnO as compared to NR-ZnO has been attributed to the angular randomization of photons inside the nanosheets. Moreover, it is implicitly assumed that natural amorphous characteristic of nanosheets with large amount of defects can further limit the transmission.

Room temperature photoluminescence was measured with He-Cd laser excitation at a wavelength of 325 nm to evaluate the optical properties of NS-ZnO versus NR-ZnO, as shown in Figure 3(b). A main peak around 384 nm refers to the near band-edge emission. A broad low intensity peak in the visible region is associated with the defect-level emission, which is attributed to deep level defects, such as oxygen vacancies and Zn interstitial defects. It revealed that NR-ZnO shows better crystalline quality than NS-ZnO because of higher near band-edge emission and lower defect-level emission peak intensity. This result is an experimental support for our suggestion that the low crystalline quality of nanosheets is responsible for the low optical transmission of nanosheets as compared to nanorods in the UV-Vis spectra.

Electrical characteristics of the C-LED, NS-LED, and NR-LED were also studied from the current-voltage (I - V) curves. Figure 4(a) shows that the turn-on voltages of all samples were about 3.28 V at an injection current of 20 mA even though the ZnO nanostructures were grown on ITO layer. No significant difference in the I - V curves was observed at an injection current up to 100 mA. ZnO nanostructures based LED devices exhibited a slight change in leakage current after fabricating the NR-ZnO and NS-ZnO on top of the devices. The leakage currents were also all around 1.3 μ A at -10 V. This small difference in leakage current at the reverse region may originate from the fabrication process of ZnO nanostructures. However, it would not lead to serious degradation

of the electrical properties. Figure 4(b) shows light output power-current (L - I) characteristics of the C-LED, NS-LED, and NR-LED. Compared to C-LED, the optical output power of the NR-LED was dramatically increased with NR-ZnO (47%) at an injection current of 100 mA. The enhanced light output power of NR-LED is primarily due to the scattering effect by surface texturing of the NR-ZnO on ITO layer. NR-ZnO structure has a large number of sidewalls and can provide a larger escape cone for the photons in the NR-LED than that in the C-LED. Moreover, the sample with ZnO nanostructures on ITO layer had the more opportunity to scatter the light at the ZnO nanostructures, which resulted in an increase in light output power. On the other hand, the light output power of NS-LED was decreased by about 42%. A possible explanation for this observation is that the NR-ZnO possesses higher crystalline quality than that of NS-ZnO. It is observed that the visible emission of NS-ZnO is enhanced and the UV emission is greatly weakened compared to NR-ZnO, as shown in Figure 3(b). This result may be due to more defects originating from Al element doping. Consequently, photons generated from the MQWs of NUV-LEDs can be trapped in defected sites of NS-ZnO, resulting in a significant decrease of the light output power.

Figure 5 shows the micrograph images of the C-LED, NS-LED, and NR-LED device operating at an injection current of 20 and 100 mA, respectively. As shown in Figure 5, it is clearly observed that higher intensity of light emission is observed in the top emitting NR-LED due to the formation of a large number of textured surfaces having a larger escape cone. NR-ZnO can also enhance the escape probability. In other words, the photons have multiple opportunities to find the escape cone more easily. However, the light output intensity of NS-ZnO is decreased because the higher defective NS-ZnO can trap or absorb the photon emitted from the MQWs. We suggest that light extraction efficiency would be

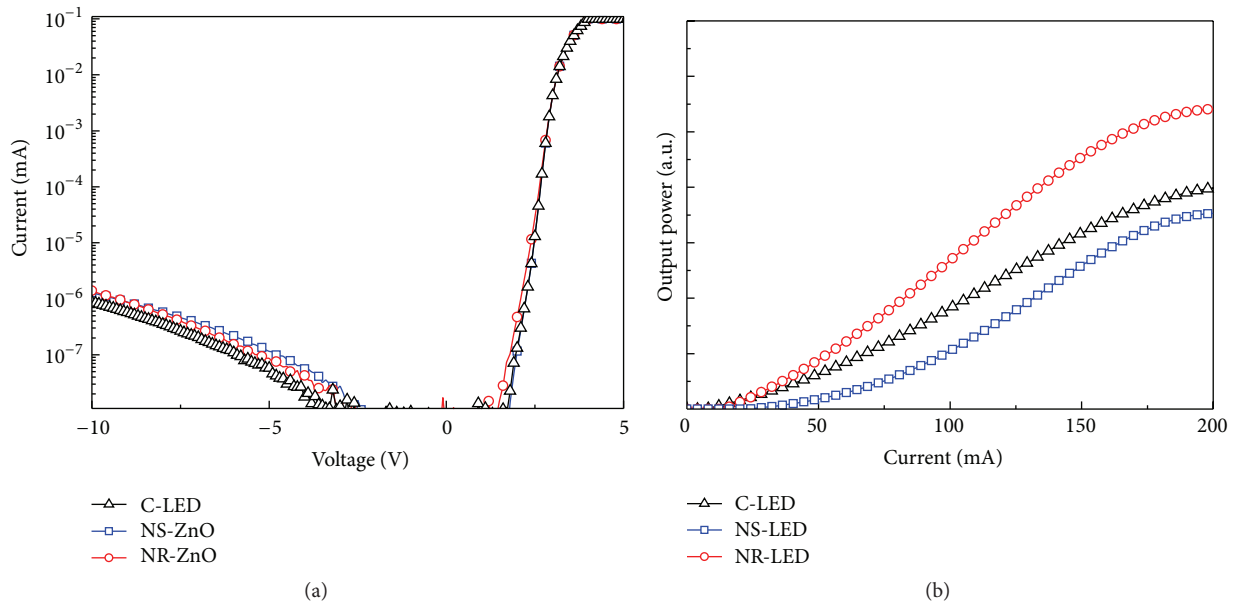


FIGURE 4: (a) *I-V* and (b) light output power as a function of applied current of fabricated NR-LED, NS-LED, and C-LED.

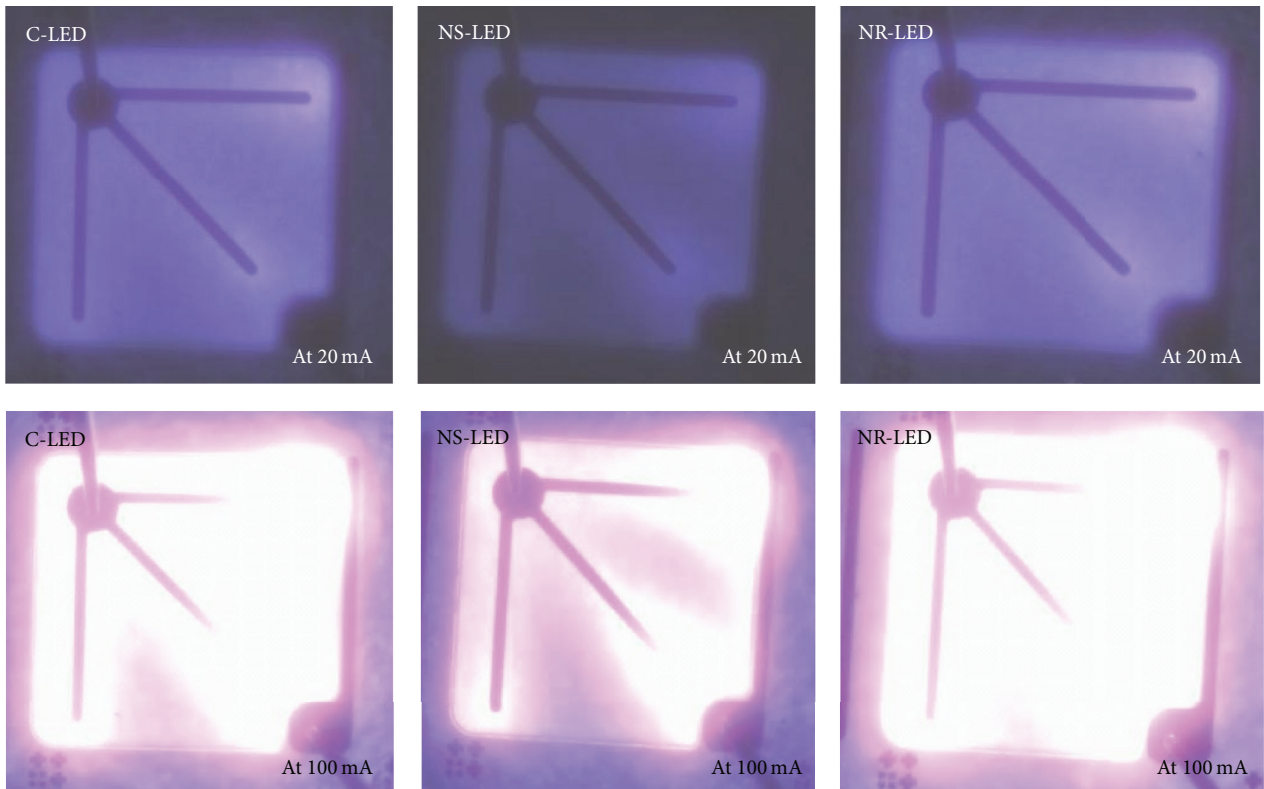


FIGURE 5: Optical micrographs of C-LED, NR-LED, and NS-LED at an operating current of 20 mA and 100 mA, respectively.

different depending on the forms of ZnO in the NUV-LEDs. In summary, NR-ZnO structure is more effective on the light extraction for the NUV-LED than NS-ZnO.

4. Conclusion

In conclusion, a facile method to enhance light extraction efficiency of 375 nm NUV-LEDs by ZnO nanostructures on a planar indium tin oxide (ITO) transparent electrode has been reported. NR-ZnO was compared with NS-ZnO to elucidate the effect of ZnO nanostructures on the light output power. At an injection current of 100 mA, the light output power of the NR-LED was enhanced by around 47% as compared to the C-LED. The increased light extraction by the NR-ZnO is due to the formation of a surface texturing, resulting in an enhancement of the escape probability and the multiple scattering for the photons in the NUV-LED. The light output efficiency of the NS-LED was decreased by 42% compared to the C-LED due to an increase of the internal reflection and light absorption in the defective NS-ZnO.

Competing Interests

The authors declare that there is no competing interests regarding the publication of this paper.

Acknowledgments

This work was supported by Basic Research Program through the National Research Foundation of Korea (NRF) funded by the Ministry of Education (NRF-2014RIA1A2008104 and 2013RIA1A2013044) and ICT & Future Planning (2010-0019694) and the BK21 Plus Center for Future Energy Materials and Devices.

References

- [1] D. Birtalan and W. Nunley, *Optoelectronics: Infrared-Visible-Ultraviolet Devices and Applications*, CRC Press, 2nd edition, 2009.
- [2] A. Khan, K. Balakrishnan, and T. Katona, "Ultraviolet light-emitting diodes based on group three nitrides," *Nature Photonics*, vol. 2, no. 2, pp. 77–84, 2008.
- [3] J. K. Sheu, S. J. Chang, C. H. Kuo et al., "White-light emission from near UV InGaN-GaN LED chip precoated with blue/green/red phosphors," *IEEE Photonics Technology Letters*, vol. 15, no. 1, pp. 18–20, 2003.
- [4] M. Iwaya, S. Terao, N. Hayashi, T. Kashima, H. Amano, and I. Akasaki, "Realization of crack-free and high-quality thick $\text{Al}_x\text{Ga}_{1-x}\text{N}$ for UV optoelectronics using low-temperature interlayer," *Applied Surface Science*, vol. 159–160, pp. 405–413, 2000.
- [5] Y. A. Xi, K. X. Chen, F. Mont et al., "Comparative study of n-type AlGaIn grown on sapphire by using a superlattice layer and a low-temperature AlN interlayer," *Journal of Crystal Growth*, vol. 299, no. 1, pp. 59–62, 2007.
- [6] T. H. Seo, S. J. Chae, B. K. Kim, G. Shin, Y. H. Lee, and E. Suh, "Enhanced light output power of near-ultraviolet light-emitting diodes with Au-doped graphene for transparent and current-spreading electrode," *Applied Physics Express*, vol. 5, no. 11, Article ID 115101, 2012.
- [7] J.-P. Shim, T. H. Seo, J. H. Min, C. M. Kang, E.-K. Suh, and D.-S. Lee, "Thin Ni film on graphene current spreading layer for GaN-based blue and ultra-violet light-emitting diodes," *Applied Physics Letters*, vol. 102, no. 15, Article ID 151115, 2013.
- [8] D.-S. Han, J.-Y. Kim, S.-I. Na et al., "Improvement of light extraction efficiency of flip-chip light-emitting diode by texturing the bottom side surface of sapphire substrate," *IEEE Photonics Technology Letters*, vol. 18, no. 13, pp. 1406–1408, 2006.
- [9] S. Fan, P. R. Villeneuve, and J. D. Joannopoulos, "Rate-equation analysis of output efficiency and modulation rate of photonic-crystal light-emitting diodes," *IEEE Journal of Quantum Electronics*, vol. 36, no. 10, pp. 1123–1130, 2000.
- [10] T. Fujii, Y. Gao, R. Sharma, E. L. Hu, S. P. DenBaars, and S. Nakamura, "Increase in the extraction efficiency of GaN-based light-emitting diodes via surface roughening," *Applied Physics Letters*, vol. 84, no. 6, pp. 855–857, 2004.
- [11] C. Huh, K.-S. Lee, E.-J. Kang, and S.-J. Park, "Improved light-output and electrical performance of InGaIn-based light-emitting diode by microroughening of the p-GaN surface," *Journal of Applied Physics*, vol. 93, no. 11, pp. 9383–9385, 2003.
- [12] X. A. Cao, A. P. Zhang, G. T. Dang et al., "Plasma damage in p-GaN," *Journal of Electronic Materials*, vol. 29, no. 3, pp. 256–261, 2000.
- [13] T. V. Cuong, H. N. Tien, V. H. Luan et al., "Controlled growth of ZnO nanomaterials via hydrothermal method: effect of buffer layer," *Journal of Nanoscience and Nanotechnology*, vol. 12, no. 4, pp. 3313–3316, 2012.
- [14] J. P. Cheng, X. B. Zhang, and Z. Q. Luo, "Oriented growth of ZnO nanostructures on Si and Al substrates," *Surface and Coatings Technology*, vol. 202, no. 19, pp. 4681–4686, 2008.
- [15] P. Uthirakumar, J. H. Kang, B. D. Ryu, H. G. Kim, H. K. Kim, and C.-H. Hong, "Nanoscale ITO/ZnO layer-texturing for high-efficiency InGaIn/GaN light emitting diodes," *Materials Science and Engineering: B*, vol. 166, no. 3, pp. 230–234, 2010.

Research Article

Atomistic Tight-Binding Theory of Electron-Hole Exchange Interaction in Morphological Evolution of CdSe/ZnS Core/Shell Nanodisk to CdSe/ZnS Core/Shell Nanorod

Worasak Sukkabot

Department of Physics, Faculty of Science, Ubon Ratchathani University, 85 Satholmark Road, Warin Chamrap, Ubon Ratchathani 34190, Thailand

Correspondence should be addressed to Worasak Sukkabot; w.sukkabot@gmail.com

Received 7 November 2015; Accepted 28 December 2015

Academic Editor: Hieu P. T. Nguyen

Copyright © 2016 Worasak Sukkabot. This is an open access article distributed under the Creative Commons Attribution License, which permits unrestricted use, distribution, and reproduction in any medium, provided the original work is properly cited.

Based on the atomistic tight-binding theory (TB) and a configuration interaction (CI) description, the electron-hole exchange interaction in the morphological transformation of CdSe/ZnS core/shell nanodisk to CdSe/ZnS core/shell nanorod is described with the aim of understanding the impact of the structural shapes on the change of the electron-hole exchange interaction. Normally, the ground hole states confined in typical CdSe/ZnS core/shell nanocrystals are of heavy hole-like character. However, the atomistic tight-binding theory shows that a transition of the ground hole states from heavy hole-like to light hole-like contribution with the increasing aspect ratios of the CdSe/ZnS core/shell nanostructures is recognized. According to the change in the ground-state hole characters, the electron-hole exchange interaction is also significantly altered. To do so, optical band gaps, ground-state electron character, ground-state hole character, oscillation strengths, ground-state coulomb energies, ground-state exchange energies, and dark-bright (DB) excitonic splitting (stoke shift) are numerically demonstrated. These atomistic computations obviously show the sensitivity with the aspect ratios. Finally, the alteration in the hole character has a prominent effect on dark-bright (DB) excitonic splitting.

1. Introduction

Because of the wealth in the improved photoluminescence quantum yields, high photostability, and size-tunable emission properties, core/shell semiconductor nanocrystals are exceptionally fascinating in the extensive applications such as light-emitting diodes [1, 2], solar cells [3–6], lasers [7], and biological imaging [8–11]. Indeed, they have already demonstrated an excellent material system for the single photon sources in quantum information processing. However, the strong confinement of the charge carriers localized in nanostructures essentially induces the intrinsic electron-hole exchange interaction resulting in a complicated excitonic band-edge fine structure that can destroy the polarization entanglement of photon source. There are several reports being concentrated on the electron-hole exchange interaction of size-dependent II–VI semiconductor nanocrystals [12–15]. Brovelli et al. [16] demonstrated that the electron-hole exchange energies could be tuned by increasing CdS

shell thickness in CdSe/CdS core/shell nanocrystals. Bryant et al. [17] implemented a nanomechanical strain to theoretically engineer the fine structure splitting of quantum dots for quantum processing using the tight-binding theory. Welander and Burkard [18] theoretically reported that a finite applied electric field was used to suppress the fine structure splitting in nonparabolic quantum dots. Sinito et al. [19] demonstrated that it was possible to manipulate the fine structure splitting using an external magnetic field which could be used to tailor the properties of entangled photon sources. Apart from the literature review, an innovative improvement in chemical synthesis of the nanostructures allows control of the material compositions and structural shapes and the realization of high-quality heterostructures in the atomic scale. Thus, Rainò et al. [20] informed about the manipulation and the tunability of the excitonic fine structure splitting in a core/shell nanorod consisting of a CdSe spherical core and an asymmetric rod-like CdS shell. A core/shell nanorod with small core and/or thick rod

diameters could robustly decrease the fine structure splitting. Exclusively, disk-type and rod-type core/shell nanostructures attracted the significant attention because they can provide the new prospects for tailoring the structural and optical properties. In the present study, the atomistic tight-binding theory is implemented to theoretically analyze the electron-hole exchange interaction in morphological evolution of CdSe/ZnS core/shell nanodisk to CdSe/ZnS core/shell nanorod with the aim of offering a deep insight into the knowledge of the shape. Undoubtedly, the atomistic tight-binding model is proficient in affording quite accurately the excitonic fine structure splitting in nanostructures [21–23]. The empirical tight-binding theory in the conjunction with sp^3s^* orbitals [24], the first nearest-neighboring interaction, spin-orbital interaction, and strain distribution is theoretically utilized as the computational tool. The strained atomic positions of CdSe/ZnS disk-type and rod-type core/shell nanostructures are optimized using the valence force field theory [25, 26]. To obtain the excitonic states near the band edges, the configuration interaction (CI) approach together with 12 lowest electron and 12 highest hole states considering the spin component is numerically implemented.

To study the electron-hole exchange interaction in morphological transformation of CdSe/ZnS core/shell nanodisk to CdSe/ZnS core/shell nanorod, the present paper is organized as follows. In Section 2, theory and methodology are briefly described. In Section 3, the computations corresponding to morphological evolution of CdSe/ZnS core/shell nanodisk to CdSe/ZnS core/shell nanorod are discussed with the aim of addressing the pronounced effect of the change in hole states on the structural and optical properties and electron-hole exchange interaction. To finish the task, Section 4 demonstrates the core conclusion.

2. Theory and Methodology

The atomistic simulations consist of several major steps. Firstly, a designation of wurtzite crystal structure with the anion (Se) being in the center of CdSe/ZnS core/shell nanostructures is declared. Secondly, because of the strain distribution induced by the lattice mismatch between CdSe and ZnS, the atomistic valence force field (VFF) method is used to optimize the strained atomic positions as described with more information in [25, 26] and also in my previous papers [27, 28]. Subsequently, the atomic positions of the optimized nanostructures are integrated into the empirical tight-binding model. The single-particle states of the atomistic tight-binding theory are expanded in terms of a linear combination of atomistic orbitals localized on each atom given by

$$\Psi = \sum_{R=1}^N \sum_{\alpha=1}^{10} C_{R,\alpha} \varphi_{\alpha}(\vec{r} - \vec{R}). \quad (1)$$

α are the localized atomic orbitals on atom R with the position variable r and the total number of atoms N in the system. sp^3s^* empirical tight-binding theory with the spin-orbit interaction and the first nearest neighboring interaction is utilized for the computations in the conjunction with

the parameterization [29] which is fitted to reproduce the experimental bulk band structure, band gaps, and effective masses. In addition, the valence-band offset of $E_{VBO} = +0.60$ eV [30] between CdSe and ZnS is incorporated into the tight-binding calculations.

Finally, to theoretically investigate the electron-hole exchange interaction in CdSe/ZnS core/shell nanostructures, a configuration interaction technique (CI) [21–23, 31, 32] is computationally applied. The two-body Hamiltonian of single excitonic states constructed from the single-particle states is given by

$$H = \sum_i E_i e_i^\dagger e_i + \sum_j E_j h_j^\dagger h_j - \sum_{ijkl} V_{ijkl}^{\text{eh,coul}} h_i^\dagger e_j^\dagger e_k h_l + \sum_{ijkl} V_{ijkl}^{\text{eh,exch}} h_i^\dagger e_j^\dagger e_k h_l. \quad (2)$$

The first two terms are the single-particle energies of electron and hole states, respectively. The third term describes the electron-hole coulomb interactions. The final term presents the electron-hole exchange interactions. The detailed calculations are numerically provided in the following.

3. Results and Discussions

To study the behavior of electron-hole exchange interaction localized in the morphological transformation of CdSe/ZnS disk-type to rod-type core/shell nanostructures, the structural parameters are assumed in the following. The CdSe diameter is 4.30 nm with the hexagonal base in the xy plane. The shape evolution from disk to rod is generated in the growth direction (z) defined as $z = \sigma D$ where the aspect ratios σ represent L/D with L and D being the lengths and diameters of CdSe core, respectively. For all cases of the calculations, ZnS shell thickness is kept fixed to be 0.765 nm. Using these structural parameters, the atomistic tight-binding model (TB) and the configuration interaction method (CI) theoretically analyzed the impact of aspect ratios (σ) on the electron-hole exchange interaction. The evolution of single-particle and excitonic gaps in CdSe/ZnS disk-type to rod-type core/shell nanostructures as a function of the aspect ratios is illustrated in Figure 1. The single-particle and excitonic gaps are decreased with the increasing aspect ratios because of the quantum confinement [33]. Next, the atomistic characters of the first electron and hole states are discussed with the aim of understanding the shape dependence on orbital localization in CdSe/ZnS disk-type to rod-type core/shell nanostructures. In Figure 2, the ground electron states display s -like character. The contribution of the ground electron states is not perturbed by the sizes of the aspect ratios. The ground-state hole character in Figure 3 varies from heavy hole-like (HH) to light hole-like (LH) state with the increasing aspect ratios. In the beginning, the ground hole states are heavy hole-like (HH). At $\sigma \approx 1.40$, the level crossing ensues. The ground hole states become light hole-like (LH) character. This analogous crossover has been theoretically reported in InAs/InP nanowire [33] and also my previous paper [34].

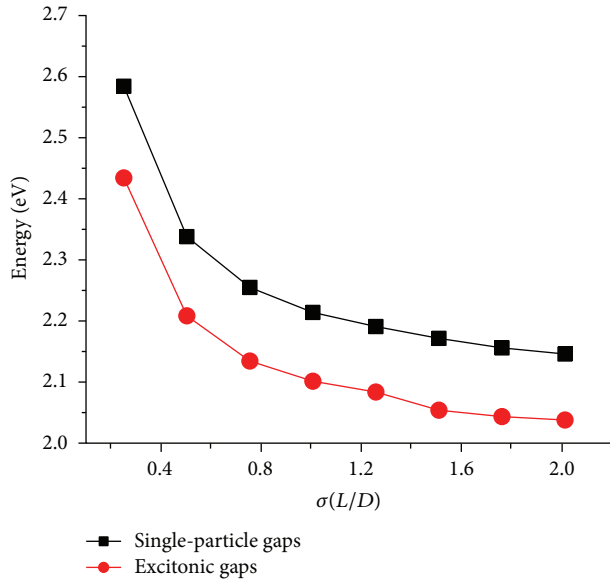


FIGURE 1: Single-particle and excitonic gaps as a function of aspect ratios (σ).

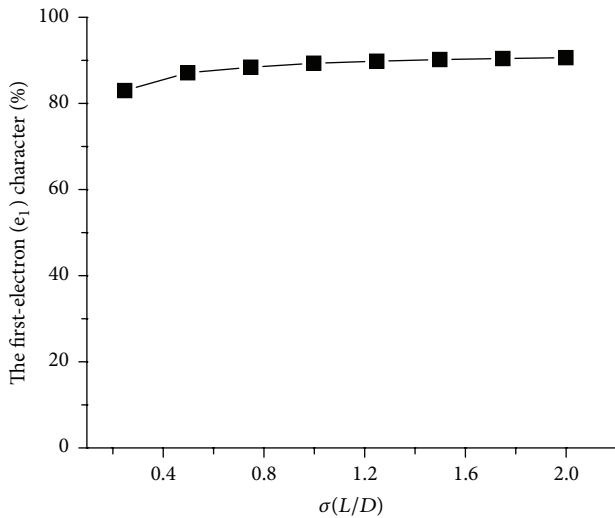


FIGURE 2: The first-electron character as a function of aspect ratios (σ).

The change in the hole wave-function character has a pronounced effect on the optical spectra. Figure 4 shows the scattering plots of the oscillation strengths for four nominated aspect ratios. The calculations of the oscillation strengths are sensitive with the aspect ratios. The significant change is probed in the level crossing of the ground-hole character. For the disk shape, the transitions between electron and hole states of the in-plane polarization ([110]) are much more pronounced than ones of the out-of-plane direction ([001]). As can be described by the atomistic characters, the dipole moment interactions between s-like ground electron states and heavy hole-like ground hole states in the xy plane are more prominent than those along the z direction. With

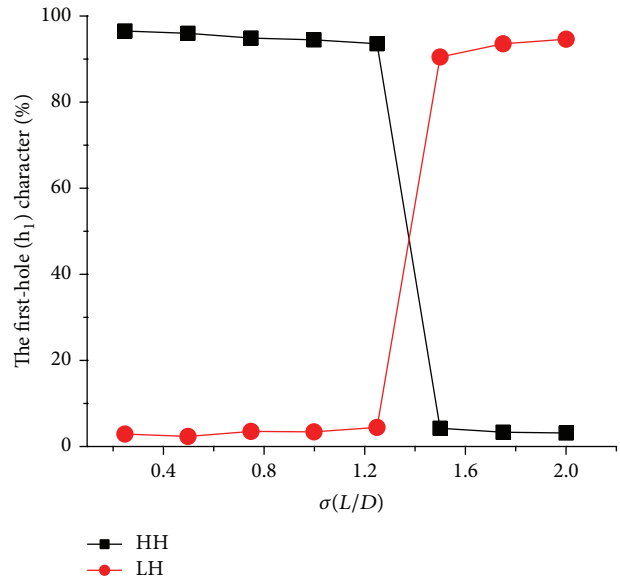


FIGURE 3: The first-hole character as a function of aspect ratios (σ). HH and LH mean heavy hole-like and light hole-like contribution, respectively.

the increasing aspect ratios, the situation changes because of the level crossing in the ground hole states. For the rod shape, the dominant contribution chiefly comes from the out-of-plane polarization ([001]) because the dipole moment interactions between s-like ground electron states and light hole-like ground hole states along z direction are stronger than those in xy plane. These atomistic behaviours have been theoretically reported in [33, 34]. Hence, the optical properties are predominantly controlled by the structural shapes of the CdSe/ZnS core/shell nanostructures.

In addition, Figures 5 and 6 show the ground-state coulomb and exchange energies as a function of aspect ratios (σ), respectively. The electron-hole interactions confined in nanostructures are mainly improved by quantum confinement. Therefore, the energies of coulomb and exchange interactions are generally decreased with the increasing aspect ratios. The information of the electron-hole coulomb interaction demonstrates that electron and hole are weakly confined in CdSe/ZnS core/shell nanorods. In case of the electron-hole exchange interaction, the strong reduction of the ground-state exchange energies is probed in CdSe/ZnS core/shell nanorods with the light hole-like character in the ground hole states. It is expected that the atomistic mechanism of electron-hole interactions is achieved by changing the aspect ratios and associated hole characters.

In the last discussions, the dark-bright (DB) excitonic splitting energies of CdSe/ZnS disk-type and rod-type core/shell nanostructures as a function of the aspect ratios are demonstrated in Figure 7. To obtain the excitonic splitting energies, the configuration interaction description (CI) considering coulomb and exchange effect is utilized with inclusion of 12 electron and 12 hole levels each. The dark-bright (DB) excitonic splitting energies, usually called stoke shift, are calculated from the energy difference between

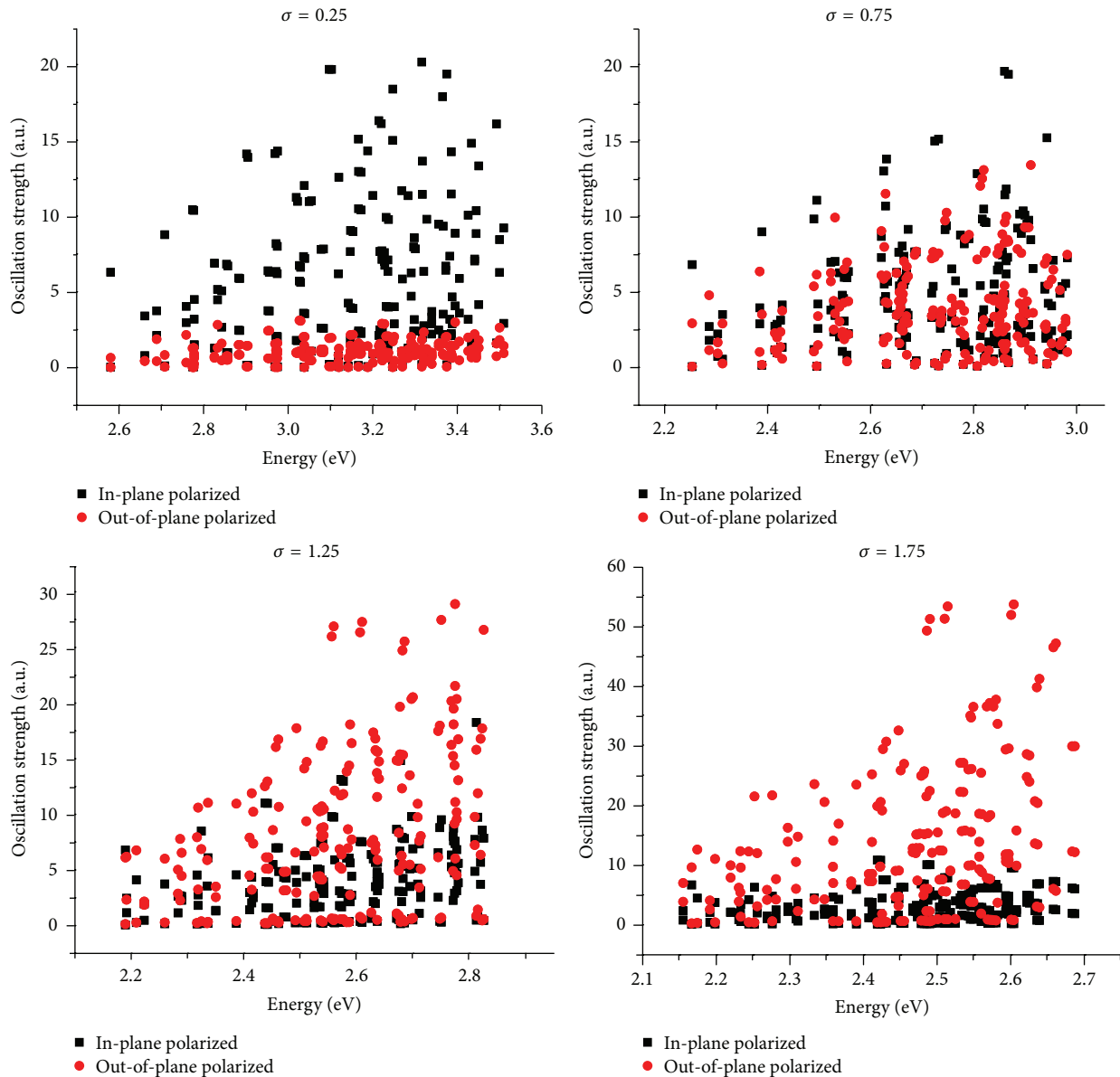


FIGURE 4: Scattering plots of oscillation strengths for four selected aspect ratios (σ).

the lowest optically forbidden excitonic state and the lowest optically allowed excitonic state. As can be seen, the reduction of the DB excitonic splitting energies is observed with the increasing aspect ratios. However, when ground-state holes become light hole-like, DB excitonic splitting energies are gradually increased. Therefore, excitonic splitting energies in morphological evolution of CdSe/ZnS core/shell nanodisk to CdSe/ZnS core/shell nanorod are considerably operated by the dimension of aspect ratios in order to grasp the desired hole characters.

4. Summary

The electron-hole exchange interaction in the morphological transformation of CdSe/ZnS core/shell nanodisk to CdSe/ZnS core/shell nanorod is theoretically studied by an

atomistic tight-binding theory (TB) and a configuration interaction description (CI). The computations highlight that the variation of the aspect ratios can be used to engineer the structural and optical properties and to switch heavy hole to light hole state. For the disk shape, the interband transitions of the in-plane polarization ([110]) are more promoted than those of the out-of-plane direction ([001]), while, for the rod shape, the central contribution is mostly from the out-of-plane polarization ([001]). In addition, the reduction in the energies of coulomb and exchange interactions is reported with the increasing aspect ratios. Changing from disk to rod, the single-particle and excitonic gaps are decreased because of the quantum confinement. The DB excitonic splitting energies are decreased with the increasing aspect ratios when the ground-state holes are heavy hole-like. Conversely, DB excitonic splitting energies are gradually increased with the

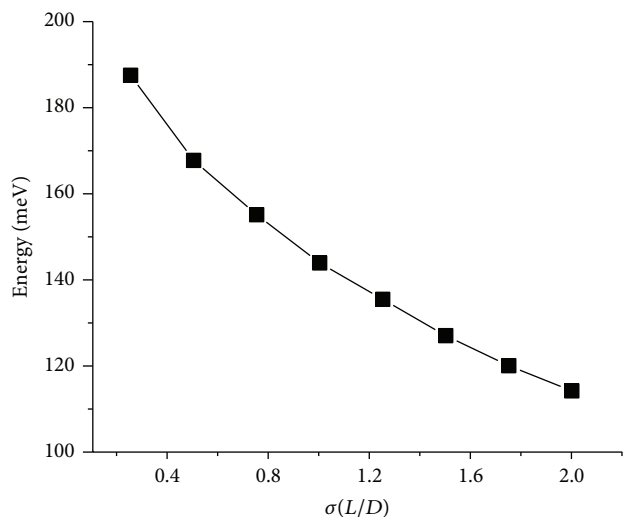


FIGURE 5: Ground-state coulomb energies as a function of aspect ratios (σ).

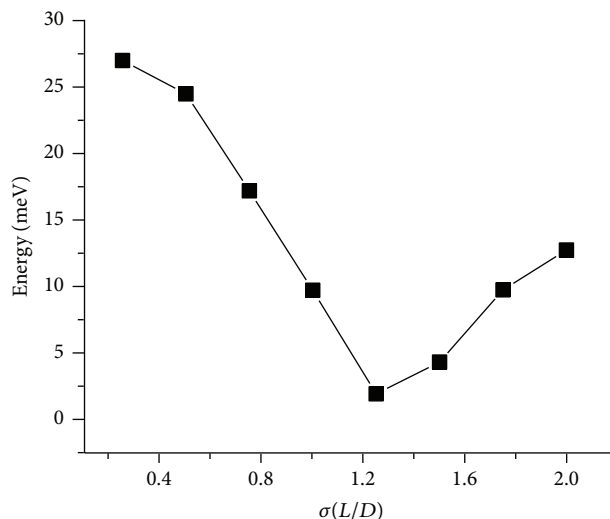


FIGURE 7: Energies of dark-bright splitting (DB) as a function of aspect ratios (σ).

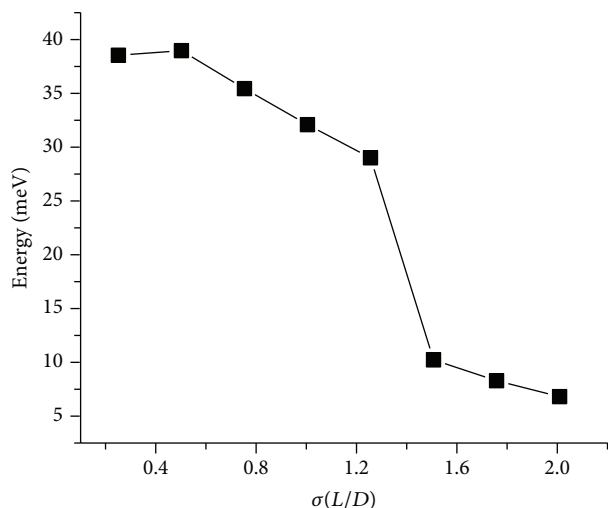


FIGURE 6: Ground-state exchange energies as a function of aspect ratios (σ).

ground-state holes being light hole-like. Finally, the atomistic computations of the electron-hole exchange interaction can provide the useful recommendation in using a light hole instead of a heavy hole for the quantum information.

Conflict of Interests

The author declares that there is no conflict of interests regarding the publication of this paper.

Acknowledgments

The author would like to acknowledge the financial support from the Thailand Research Fund Grants (TRG58880072) and Department of Physics, Faculty of Science, Ubon Ratchathani University, Thailand.

References

- [1] M. J. Bowers II, J. R. McBride, and S. J. Rosenthal, "White-light emission from magic-sized cadmium selenide nanocrystals," *Journal of the American Chemical Society*, vol. 127, no. 44, pp. 15378–15379, 2005.
- [2] P. O. Anikeeva, C. F. Madigan, S. A. Coe-Sullivan, J. S. Steckel, M. G. Bawendi, and V. Bulovic, "Photoluminescence of CdSe/ZnS core/shell quantum dots enhanced by energy transfer from a phosphorescent donor," *Chemical Physics Letters*, vol. 424, no. 1–3, pp. 120–125, 2006.
- [3] A. J. Nozik, "Quantum dot solar cells," *Physica E: Low-Dimensional Systems and Nanostructures*, vol. 14, no. 1–2, pp. 115–120, 2002.
- [4] I. Gur, N. A. Fromer, M. L. Geier, and A. P. Alivisatos, "Air-stable all-inorganic nanocrystal solar cells processed from solution," *Science*, vol. 310, no. 5747, pp. 462–465, 2005.
- [5] M. C. Hanna and A. J. Nozik, "Solar conversion efficiency of photovoltaic and photoelectrolysis cells with carrier multiplication absorbers," *Journal of Applied Physics*, vol. 100, no. 7, Article ID 074510, 2006.
- [6] P. V. Kamat, "Quantum dot solar cells. Semiconductor nanocrystals as light harvesters," *Journal of Physical Chemistry C*, vol. 112, no. 48, pp. 18737–18753, 2008.
- [7] V. I. Klimov, A. A. Mikhailovsky, S. Xu et al., "Optical gain and stimulated emission in nanocrystal quantum dots," *Science*, vol. 290, no. 5490, pp. 314–317, 2000.
- [8] S. Achilefu, "Lighting up tumors with receptor-specific optical molecular probes," *Technology in Cancer Research & Treatment*, vol. 3, no. 4, pp. 393–409, 2004.
- [9] M. Bruchez Jr., M. Moronne, P. Gin, S. Weiss, and A. P. Alivisatos, "Semiconductor nanocrystals as fluorescent biological labels," *Science*, vol. 281, no. 5385, pp. 2013–2016, 1998.
- [10] A. Mukherjee and S. Ghosh, "Optimum excitation photon energy for CdSe-ZnS core-shell quantum dot based luminescence imaging," *Journal of Physics D*, vol. 45, no. 19, Article ID 195103, 2012.
- [11] M. Dahan, S. Lévi, C. Luccardini, P. Rostaing, B. Riveau, and A. Triller, "Diffusion dynamics of glycine receptors revealed by

- single-quantum dot tracking,” *Science*, vol. 302, no. 5644, pp. 442–445, 2003.
- [12] A. L. Efros, M. Rosen, M. Kuno, M. Nirmal, D. J. Norris, and M. Bawendi, “Band-edge exciton in quantum dots of semiconductors with a degenerate valence band: dark and bright exciton states,” *Physical Review B*, vol. 54, no. 7, pp. 4843–4856, 1996.
- [13] M. Nirmal, D. J. Norris, M. Kuno, M. G. Bawendi, A. L. Efros, and M. Rosen, “Observation of the ‘dark exciton’ in CdSe quantum dots,” *Physical Review Letters*, vol. 75, no. 20, pp. 3728–3731, 1995.
- [14] N. Le Thomas, E. Herz, O. Schöps, U. Woggon, and M. V. Artemyev, “Exciton fine structure in single CdSe nanorods,” *Physical Review Letters*, vol. 94, no. 1, Article ID 016803, 2005.
- [15] I. Moreels, G. Rainò, R. Gomes, Z. Hens, T. Stöferle, and R. F. Mahrt, “Band-edge exciton fine structure of small, nearly spherical colloidal CdSe/ZnS quantum dots,” *ACS Nano*, vol. 5, no. 10, pp. 8033–8039, 2011.
- [16] S. Brovelli, R. D. Schaller, S. A. Crooker et al., “Nano-engineered electron-hole exchange interaction controls exciton dynamics in core-shell semiconductor nanocrystals,” *Nature Communications*, vol. 2, no. 1, article 280, 2011.
- [17] G. W. Bryant, N. Malkova, and J. Sims, “Mechanism for controlling the exciton fine structure in quantum dots using electric fields: manipulation of exciton orientation and exchange splitting at the atomic scale,” *Physical Review B*, vol. 88, no. 16, Article ID 161301, 2013.
- [18] E. Welander and G. Burkard, “Electric control of the exciton fine structure in nonparabolic quantum dots,” *Physical Review B*, vol. 86, no. 16, Article ID 165312, 2012.
- [19] C. Sinito, M. J. Fernée, S. V. Goupalov, P. Mulvaney, P. Tamarat, and B. Lounis, “Tailoring the exciton fine structure of cadmium selenide nanocrystals with shape anisotropy and magnetic field,” *ACS Nano*, vol. 8, no. 11, pp. 11651–11656, 2014.
- [20] G. Rainò, T. Stöferle, I. Moreels, R. Gomes, Z. Hens, and R. F. Mahrt, “Controlling the exciton fine structure splitting in CdSe/CdS dot-in-rod nanojunctions,” *ACS Nano*, vol. 6, no. 3, pp. 1979–1987, 2012.
- [21] G. W. Bryant, M. Zieliński, N. Malkova, J. Sims, W. Jaskólski, and J. Aizpurua, “Effect of mechanical strain on the optical properties of quantum dots: controlling exciton shape, orientation, and phase with a mechanical strain,” *Physical Review Letters*, vol. 105, no. 6, Article ID 067404, 2010.
- [22] M. Korkusinski and P. Hawrylak, “Atomistic theory of emission from dark excitons in self-assembled quantum dots,” *Physical Review B*, vol. 87, no. 11, Article ID 115310, 2013.
- [23] M. Zieliński, “Valence band offset, strain and shape effects on confined states in self-assembled InAs/InP and InAs/GaAs quantum dots,” *Journal of Physics: Condensed Matter*, vol. 25, no. 46, Article ID 465301, 2013.
- [24] P. Vogl, H. P. Hjalmarson, and J. D. Dow, “A semi-empirical tight-binding theory of the electronic structure of semiconductors,” *Journal of Physics and Chemistry of Solids*, vol. 44, no. 5, pp. 365–378, 1983.
- [25] P. N. Keating, “Effect of invariance requirements on the elastic strain energy of crystals with application to the diamond structure,” *Physical Review*, vol. 145, no. 2, pp. 637–645, 1966.
- [26] R. M. Martin, “Elastic properties of ZnS structure semiconductors,” *Physical Review B*, vol. 1, no. 10, pp. 4005–4011, 1970.
- [27] W. Sukkabot, “Electronic structure and optical properties of colloidal InAs/InP core/shell nanocrystals: tight-binding calculations,” *Physica E: Low-Dimensional Systems and Nanostructures*, vol. 63, pp. 235–240, 2014.
- [28] W. Sukkabot, “Variation in the structural and optical properties of CdSe/ZnS core/shell nanocrystals with ratios between core and shell radius,” *Physica B: Condensed Matter*, vol. 454, pp. 23–30, 2014.
- [29] Ö. Akinci, H. H. Gürel, and H. Ünlü, “Semiempirical tight binding modeling of Cd based II–VI heterostructures for solar cells,” *Thin Solid Films*, vol. 511–512, pp. 684–689, 2006.
- [30] S. Chattopadhyay, P. Sen, J. Thomas Andrews, and P. Kumar Sen, “Semiconductor core-shell quantum dot: a low temperature nano-sensor material,” *Journal of Applied Physics*, vol. 111, no. 3, Article ID 034310, 2012.
- [31] F. A. Reboredo, A. Franceschetti, and A. Zunger, “Dark excitons due to direct Coulomb interactions in silicon quantum dots,” *Physical Review B*, vol. 61, no. 19, pp. 13073–13087, 2000.
- [32] E. L. de Oliveira, E. L. Albuquerque, J. S. de Sousa, G. A. Farias, and F. M. Peeters, “Configuration-interaction excitonic absorption in small Si/Ge and Ge/Si core/shell nanocrystals,” *Journal of Physical Chemistry C*, vol. 116, no. 7, pp. 4399–4407, 2012.
- [33] M. Zieliński, “Fine structure of light-hole excitons in nanowire quantum dots,” *Physical Review B*, vol. 88, no. 11, Article ID 115424, 2013.
- [34] W. Sukkabot, “Tight-binding theory in morphological evolution of CdSe/ZnS core/shell nanodisk to CdSe/ZnS core/shell nanorods,” *Physica Scripta*, vol. 89, no. 11, Article ID 115806, 2014.

Research Article

First-Principle Study on the Interaction between Fe and Trivacancy in Graphene

Xielong Hu and Fanyan Meng

Department of Physics, University of Science & Technology Beijing, Beijing 100083, China

Correspondence should be addressed to Fanyan Meng; meng7707@sas.ustb.edu.cn

Received 30 October 2015; Revised 11 December 2015; Accepted 20 December 2015

Academic Editor: Shamsul Arafin

Copyright © 2016 X. Hu and F. Meng. This is an open access article distributed under the Creative Commons Attribution License, which permits unrestricted use, distribution, and reproduction in any medium, provided the original work is properly cited.

Ab initio calculations using density functional theory (DFT) have been performed in order to explore structure and energy gap opening of graphene with bridged-trivacancy and single adsorbed with Fe atom. Compared to the previous reconstructed trivacancy adsorbed with Fe atom with the energy gap of 0.10 eV, one interesting structure for the Fe-doped bridged-trivacancy complex has been identified, with one Fe atom above the graphene plane, and possesses energy gap with the value of 0.32 eV in the bridged circumstance. The band gap can be explained by the decrease of the free electrons. These results provide insights to engineer graphene's properties through defect addition and manipulation for industrial semiconductor applications such as the photocatalytic technology and graphene based electronics.

1. Introduction

Graphene is among the most potential utilized materials currently studied [1–3]. It exhibits extraordinary properties in electrology [4, 5], magnetism [6, 7], and dynamics [8], proved by various theoretical and experimental studies. However, graphene is a semimetal, which greatly limits the application in the graphene-based electronic field [9–11]. Consequently, in the recent decades, many approaches, such as by employing a staggered AB sublattice potential [12], strain effect [13], intrinsic spin-orbit coupling [14] in single-layer graphene, functionalization with chemical groups [15–17], or applying a perpendicular electric field in bilayer graphene [18], have been explored to open the gap of graphene for designing semiconductor device.

Chan et al. have studied the structures and magnetism about pure graphene adsorbed with many elements such as Li, Na, K, Ca, and Al [19]. However, precise and stable structures of the transition metal (TM) adsorbed on graphene are hardly obtained because TM adsorbents can move freely on the surface of pristine graphene, which limits the use of surface adatom as robust and reliable dopants for nanoelectronic and magnetic applications [20]. Recently, it is forecasted that attaching metal atoms to defected graphene is much firmer

than to pristine graphene by theoretical studies [21–25]. Kim et al. have used X-ray magnetic circular dichroism (XMCD) to study the electronic and magnetic properties of transition metal (TM), for example, Fe, Co, and Ni clusters on monolayer graphene [26]. Also a very high magnetic anisotropy energy (MAE) has been found in single-vacancy graphene adsorbed with Ir dimer [27]. Dynamics of single Fe adatom on graphene vacancies have been studied using focused electron beam irradiation [28]. Vacancy-assisted doping method is one available technique for introducing dopants into graphene.

As a matter of fact, iron in graphene nanostructures are very common in experiment, such as Fe pairs doped in graphene [20], single Fe atoms in graphene vacancies [29, 30], and Fe₃O₄/graphene nanocomposites [31–34]. In previous work, band gap of graphene could be opening via Fe atom adsorption [11]. Recently, an interesting structure of graphene trivacancy, which was achieved by using an electron beam to bombard the graphene sheet, has been commonly observed by Robertson et al. [35]. The new structure has a bridging atom (thereafter called bridged-trivacancy), significantly different from the reconstructed trivacancy (r-trivacancy) observed by Wang et al. [36]. Consequently, a combination

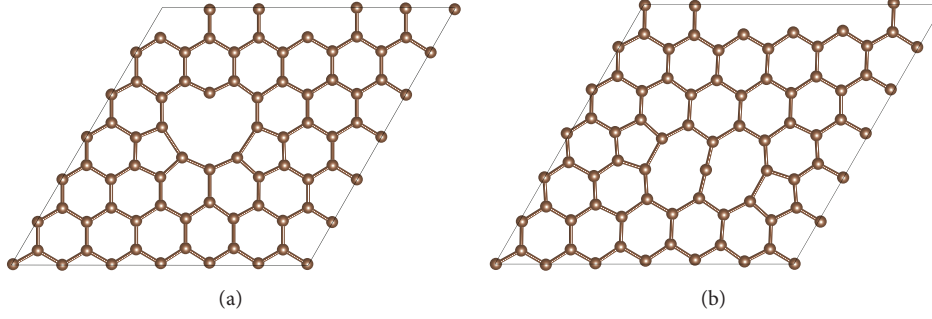


FIGURE 1: (a) Optimized 6×6 graphene supercell with r-trivacancy. (b) Optimized 6×6 graphene supercell with b-trivacancy.

of Fe adsorption and b-trivacancy might contribute to extend the application of graphene by opening the band gap.

This work presents a detailed study of the structure and electronic properties of graphene with r-trivacancy and b-trivacancies trapping Fe atom, using the density functional theory (DFT). Our studies may verify the feasibility of improving graphene electrical properties by controlling TM atom doping and vacancies.

2. Calculation Details

First-principles calculations based on the spin-polarized density functional theory (DFT) were performed using the projector augmented wave (PAW) [37], as implemented in the Vienna Ab initio Simulation Package (VASP) program [38]. The generalized gradient approximation in the Perdew-Burke-Ernzerhof (PBE) [39] parameterization was employed for the exchange-correlation functional. The plane-wave cut-off energy was set to 500 eV. The geometry optimization and total energy calculations were performed until the residual force was within 0.01 eV/\AA and the total energy converged to 10^{-5} eV . The k -point mesh for sampling the Brillouin zone was generated including the gamma point. A $4 \times 4 \times 1$ k -point mesh was used for geometry optimization, and a $6 \times 6 \times 1$ k -point mesh was used for total energy calculations.

We modeled the defect systems using supercells large enough (5×5 and 6×6 supercells in the lateral direction with a 20 \AA thick vacuum in the vertical direction) to minimize boundary effects on the energetics of the systems. Graphene's lattice constant was calculated to be 2.470 \AA , which is similar to the calculated value (2.468 \AA) by Dai et al. and the experimental value of 2.46 \AA [21].

3. Structures for System

Three kinds of trivacancies in graphene have been discovered in previous research, the r-trivacancy observed by Wang in 2012 [35] and the b-trivacancy observed by Robertson in 2014 [36], and the optimized equilibrium configurations for the r-trivacancy and b-trivacancy in our simulations using DFT are shown in Figure 1. The b-trivacancy is not just stabilized by simple bond reconstructions between undercoordinated carbon atoms, as exhibited by r-trivacancy. Reconstructions consist of undercoordinated bridging carbon atoms spanning

the vacancy to saturate edge atoms in b-trivacancy, which matches well with the previous work [36].

All the systems with Fe adsorbate on perfect graphene and defective graphene (containing a r-trivacancy or b-trivacancy) are studied. Three possible adsorption sites of Fe on the perfect graphene are labeled as follows: hollow (H), top (T), and bridge (B). And the complexes of perfect graphene adsorbed with Fe which locates in the three possible sites are indicated as Fe@G(H) , Fe@G(T) , and Fe@G(B) , respectively. For adsorption on defect-free graphene, Fe@G(H) (on the hollow site) is the most stable complex, which is in good agreement with the previous theoretical results [5, 19]. In the case of the adsorption of Fe on the defective graphene, Fe is positioned at different hollow, top, and bridge sites in the trivacancy region as the initial positions and then fully relaxed. The configurations of the adsorption of Fe on defective graphene are shown in Figure 2, in both top view and side view. For convenience, the complex of Fe adsorbed on the graphene with a r-trivacancy is labeled as Fe@RTV , and the one with b-trivacancy as Fe@BTV . From the side views, it is obvious that Fe atom is above the plane of graphene with b-trivacancy and the adatom-graphene distance d (\AA) is 1.38 \AA .

The formation energy E_f of a trivacancy in graphene, indicated by E_f , is defined as

$$E_f = E_s - \frac{N-n}{N} E_g, \quad (1)$$

where $n = 3$ is the number of vacant C atoms in the system, and N is the total number of C atoms in supercells of the perfect graphene. E_s and E_g are the energies of the graphene with r-trivacancy or b-trivacancy and the 5×5 or 6×6 graphene supercells, respectively. The adsorption energy of Fe on the perfect or defective graphene is defined as

$$E_{\text{ads}} = E_s - E_g - E_{\text{Fe}}, \quad (2)$$

where E_s , E_g , and E_{Fe} are the energies for the optimized systems of Fe-graphene with or without trivacancy, the 5×5 or 6×6 graphene supercells with or without trivacancy, and the isolated Fe atom, respectively.

Table 1 summarizes the energetic and structural properties of the 5×5 and 6×6 supercells of graphene with trivacancy adsorbed with Fe. For comparison, the formation energy of the trivacancy in graphene and the adsorption

TABLE 1: Energetic and structural properties of Fe on the defect-free graphene and defective graphene with r-trivacancy and b-trivacancy. The properties listed include the size of graphene supercells s , types of the Fe-graphene complex t , the Fe-graphene distance d (Å), formation energy E_f (eV) of trivacancy in graphene, adsorption energies E_{ads} (eV), bulk band gap Δ (eV), and the magnetization of the adatom μ_{ag} (μ_{B}). For comparison, the magnetization of the graphene with a trivacancy is included.

s	t	d (Å)	E_f (eV)	E_{ads} (eV)	Δ (eV)	μ_{ag} (μ_{B})
5×5	Fe@RTV	0.00	—	-6.35	0.13	2.00
	Fe@BTV	1.24	—	-6.90	0.32	0.00
	Fe@G(H)	1.65	—	-1.04	0.08	2.00
	Fe@G(B)	2.23	—	-0.28	0.00	4.10
	Fe@G(T)	2.06	—	-0.27	0.00	4.10
	r-trivacancy	—	11.68	—	0.00	1.05
	b-trivacancy	—	14.86	—	0.00	1.66
6×6	Fe@RTV	0.00	—	-6.61	0.03	2.00
	Fe@BTV	1.38	—	-6.96	0.25	0.00
	Fe@G(H)	1.50	—	-1.13	0.07	2.00
	Fe@G(B)	2.20	—	-0.29	0.00	4.10
	Fe@G(T)	2.12	—	-0.28	0.00	4.10
	r-trivacancy	—	11.13	—	0.00	1.05
	b-trivacancy	—	14.27	—	0.00	1.66

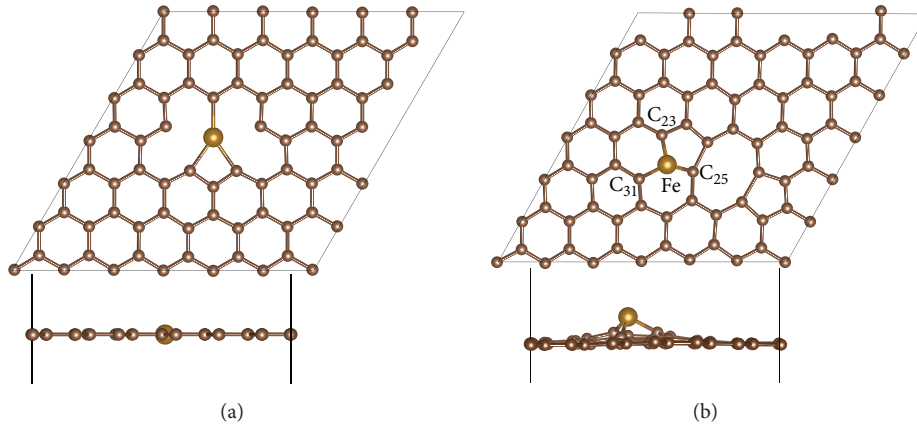


FIGURE 2: The optimized configurations of Fe adsorbed on the 6×6 graphene supercell with a trivacancy in both top view and side view. (a) Fe on the graphene with r-trivacancy (Fe@RTV) and (b) Fe on the graphene with b-trivacancy (Fe@BTV).

energy of Fe on the defect-free graphene are also included in Table 1. The adsorption energy for Fe@G(H) complex is the lowest, indicating that the stable position is the hollow site. The adsorption energy of Fe adsorbed on defective graphene with a trivacancy (Fe@TV) is much lower than that of adsorption on perfect graphene, indicating Fe@TV is more stable, which conforms to the previous studies [22]. It means that the introduction of a trivacancy on graphene will improve the adsorption of Fe atom. The formation energy of r-trivacancy is 11.68 eV, consistent with the result in [21], lower than that of b-trivacancy (14.86 eV), indicating that the b-trivacancy is a metastable structure. It is in good agreement with previous studies [35]. From Table 1, we also notice that graphene supercell with b-trivacancy adsorbed with Fe (Fe@BTV) has a lower adsorption energy in comparison with r-trivacancy adsorbed with Fe (Fe@RTV) in the same concentration, which relates with a better incorporation of the adsorbate into the graphene framework. It is worth noting that the band

gaps of Fe@BTV are 0.32 eV and 0.25 eV for 5×5 and 6×6 graphene supercells, respectively. By contrast, the band gaps of Fe@RTV are 0.13 eV and 0.03 eV for 5×5 and 6×6 supercells, respectively. The system of Fe adsorbed on the perfect graphene has the maximum band gaps of 0.08 eV, which is similar to the result (100.8 meV) in [11]. Fe@BTV system may have a bearing on important applications such as graphene-based electronic device.

4. DOS for Fe@BTV

The graphene with b-trivacancy and r-trivacancy is metallic, as the existence of trivacancy in graphene will increase the number of free electrons in the system. The partial densities of states (PDOS) for spin-up and spin-down electrons of Fe atom and adjacent C atoms and the total density of states (TDOS) in 5×5 and 6×6 graphene are calculated as shown in Figure 3. The indices of C atoms are labeled in Figure 2(b)

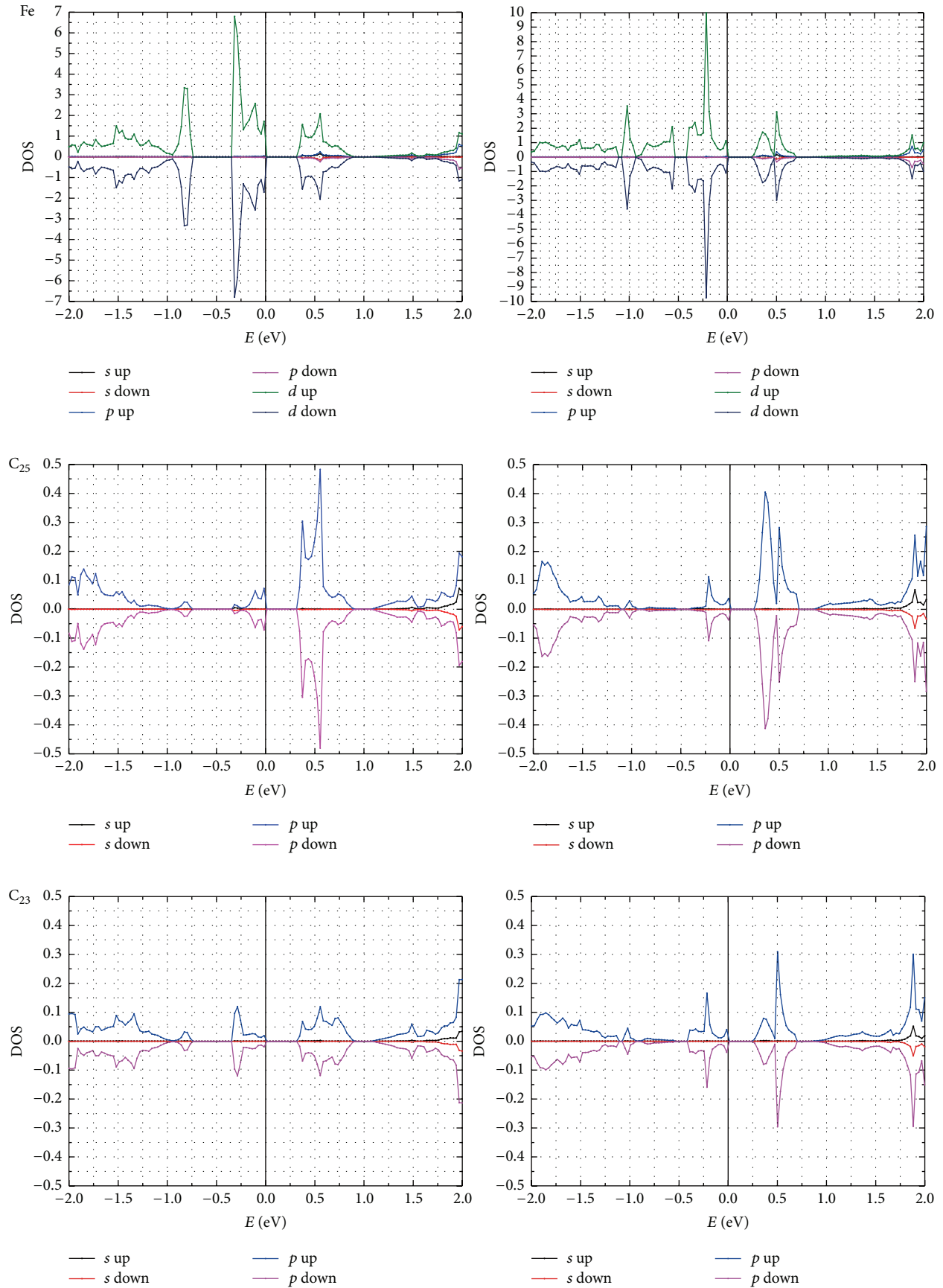


FIGURE 3: Continued.

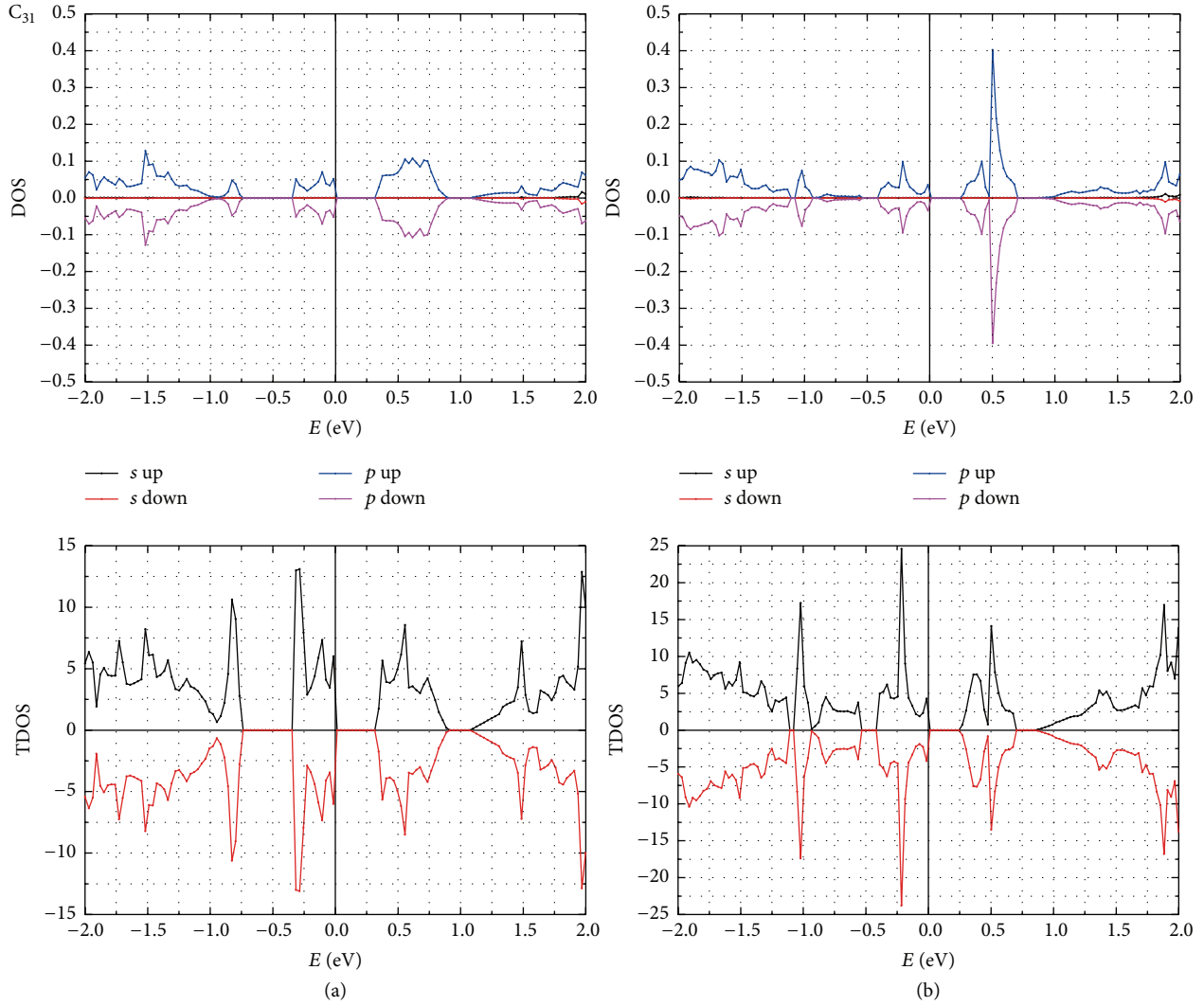


FIGURE 3: The partial densities of states (PDOS) for spin-up and spin-down electrons for Fe atom and C atoms vicinity of adsorbed Fe and the total density of states (TDOS) in 5×5 and 6×6 graphene: (a) 5×5 graphene, (b) 6×6 graphene.

and C_{25} labels the bridge C atom. Obviously, for b-trivacancy, the spin-up and spin-down DOS of C_{25} , C_{23} , C_{31} , Fe, and Fe@BTV is mirror symmetry, indicating no magnetic moment. The PDOS of adjacent C atoms match well with Fe $3d$ orbitals. In 5×5 graphene all the PDOS locate at $-2 \sim -0.75$ eV, $-6 \sim 0$ eV, and $0.32 \sim 0.7$ eV. Similar conclusions can be got in 6×6 graphene. In particular, the PDOS of C_{25} $2p$ orbitals match so consistently with Fe $3d$ orbitals. It suggests that Fe atom has formed covalent bonds with adjacent C atoms. Stronger Fe-C interaction was observed between Fe- C_{25} than that between Fe- C_{23} and Fe- C_{31} . The magnetization of Fe in b-trivacancy is $0 \mu_B$ while the Fe atom in r-trivacancy has magnetization of $2 \mu_B$ (Table 1). This is consistent with the fact that there are enough ten electrons in the $3d$ orbitals of Fe in b-trivacancy after two $4s$ electrons of Fe transferred into $3d$ orbitals and sharing two $2p$ electrons from neighbouring C atoms.

Adsorbate opens the band gap of graphene with b-trivacancy. Fe adatom has formed covalent bonds with

adjacent C atoms in the b-trivacancy region, and the number of free electrons is reduced, resulting in the opening of the energy gap.

The band structures for Fe@BTV are shown in Figure 4. It could be found that an energy gap is opened by trapping Fe to the b-trivacancy and the energy gap is larger in Figure 4(a) than that in Figure 4(b). The value of energy gap is 0.32 and 0.25 for (a) and (b), respectively.

5. Conclusions

In conclusion, density functional theory calculations have been performed to investigate the interaction of Fe adatom with bridged-trivacancy in graphene. The graphene with b-trivacancy trapping Fe atom has one stable structure, namely, Fe@BTV. The adsorption of Fe atom can open a finite energy gap in both r-trivacancy and b-trivacancy. The band gap of Fe@BTV is 0.32 eV, larger than the value of Fe@RTV (0.1 eV), which is close to the value for developing graphene-based

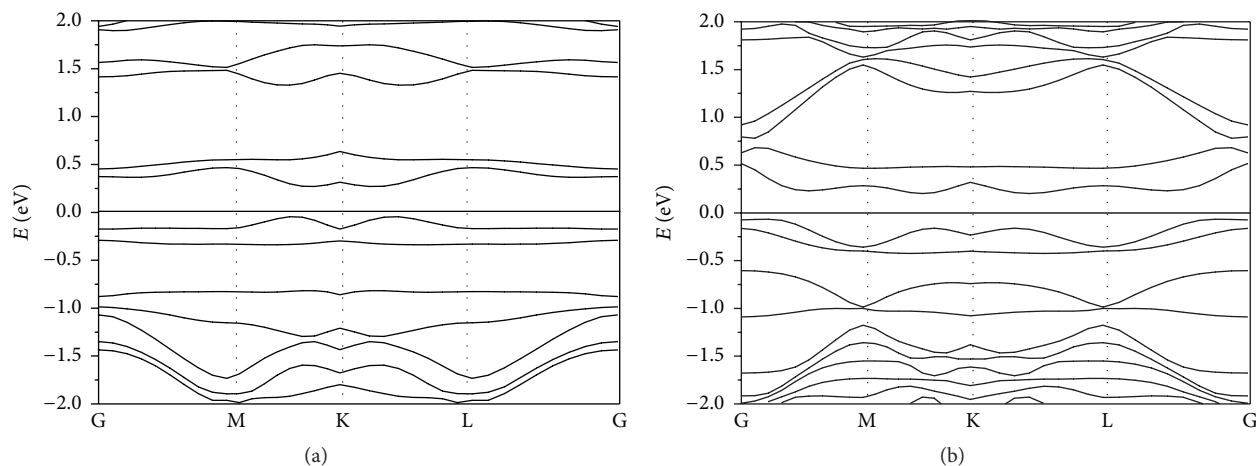


FIGURE 4: Band structures of Fe@BTV complex. (a) Optimized 5×5 graphene supercell with b-trivacancy trapping Fe. (b) Optimized 6×6 graphene supercell with b-trivacancy trapping Fe.

electronics. Fe adatom has formed covalent bonds with adjacent C atoms in the b-trivacancy region, and the number of free electrons is reduced, resulting in the opening of the energy gap. The findings might provide a promising scheme for gap opening of graphene for industrial semiconductor applications and the photocatalytic technology.

Conflict of Interests

The authors declare that there is no conflict of interests regarding the publication of this paper.

Acknowledgments

The authors thank R. Yu for discussions. This work was supported by National Basic Research Program of China (2011CB606406) and the Fundamental Research Funds for the Central Universities (TP-A3: 06108170). This work used the resources of Shanghai Supercomputer Center.

References

- [1] S. Das, M. Kim, J. Lee, and W. Choi, "Synthesis, properties, and applications of 2-D materials: a comprehensive review," *Critical Reviews in Solid State and Materials Sciences*, vol. 39, no. 4, pp. 231–252, 2014.
- [2] A. K. Geim and K. S. Novoselov, "The rise of graphene," *Nature Materials*, vol. 6, no. 3, pp. 183–191, 2007.
- [3] O. V. Yazyev and L. Helm, "Defect-induced magnetism in graphene," *Physical Review B—Condensed Matter and Materials Physics*, vol. 75, no. 12, Article ID 125408, 2007.
- [4] A. H. Castro Neto, F. Guinea, N. M. R. Peres, K. S. Novoselov, and A. K. Geim, "The electronic properties of graphene," *Reviews of Modern Physics*, vol. 81, article 109, 2009.
- [5] Y. Mao, J. Yuan, and J. Zhong, "Density functional calculation of transition metal adatom adsorption on graphene," *Journal of Physics Condensed Matter*, vol. 20, no. 11, Article ID 115209, 2008.
- [6] Y. Zhang, S. Talapatra, S. Kar, R. Vajtai, S. K. Nayak, and P. M. Ajayan, "First-principles study of defect-induced magnetism in carbon," *Physical Review Letters*, vol. 99, Article ID 107201, 2007.
- [7] M. Topsakal, E. Aktürk, H. Sevinçli, and S. Ciraci, "First-principles approach to monitoring the band gap and magnetic state of a graphene nanoribbon via its vacancies," *Physical Review B*, vol. 78, Article ID 235435, 2008.
- [8] T. Susi, J. Kotakoski, D. Kepaptsoglou et al., "Silicon-carbon bond inversions driven by 60-keV electrons in graphene," *Physical Review Letters*, vol. 113, no. 11, Article ID 115501, 2014.
- [9] K. S. Novoselov, Z. Jiang, Y. Zhang et al., "Room-temperature quantum hall effect in graphene," *Science*, vol. 315, no. 5817, p. 1379, 2007.
- [10] Y. Zhang, Y.-W. Tan, H. L. Stormer, and P. Kim, "Experimental observation of the quantum Hall effect and Berry's phase in graphene," *Nature*, vol. 438, no. 7065, pp. 201–204, 2005.
- [11] J. Ding, Z. Qiao, W. Feng, Y. Yao, and Q. Niu, "Engineering quantum anomalous/valley Hall states in graphene via metal-atom adsorption: an *ab-initio* study," *Physical Review B*, vol. 84, Article ID 195444, 2011.
- [12] D. Xiao, W. Yao, and Q. Niu, "Valley-contrasting physics in graphene: magnetic moment and topological transport," *Physical Review Letters*, vol. 99, Article ID 236809, 2007.
- [13] F. Guinea, M. I. Katsnelson, and A. K. Geim, "Energy gaps and a zero-field quantum Hall effect in graphene by strain engineering," *Nature Physics*, vol. 6, pp. 30–33, 2010.
- [14] C. L. Kane and E. J. Mele, " Z_2 topological order and the quantum spin hall effect," *Physical Review Letters*, vol. 95, no. 14, Article ID 146802, 2005.
- [15] D. W. Boukhvalov and M. I. Katsnelson, "Tuning the gap in bilayer graphene using chemical functionalization: density functional calculations," *Physical Review B*, vol. 78, no. 8, Article ID 085413, 2008.
- [16] M. Hammouri, S. K. Jha, and I. Vasiliev, "First-principles study of graphene and carbon nanotubes functionalized with benzyne," *The Journal of Physical Chemistry C*, vol. 119, no. 32, pp. 18719–18728, 2015.
- [17] A. J. Yan and M. Y. Chou, "Oxidation functional groups on graphene: structural and electronic properties," *Physical Review B*, vol. 82, Article ID 125403, 2010.

- [18] J. B. Oostinga, H. B. Heersche, X. Liu, A. F. Morpurgo, and L. M. K. Vandersypen, "Gate-induced insulating state in bilayer graphene devices," *Nature Materials*, vol. 7, pp. 151–157, 2008.
- [19] K. T. Chan, J. B. Neaton, and M. L. Cohen, "First-principles study of metal adatom adsorption on graphene," *Physical Review B*, vol. 77, no. 23, Article ID 235430, 2008.
- [20] Z. He, K. He, A. W. Robertson et al., "Atomic structure and dynamics of metal dopant pairs in graphene," *Nano Letters*, vol. 14, no. 7, pp. 3766–3772, 2014.
- [21] X. Q. Dai, J. H. Zhao, M. H. Xie, Y. N. Tang, Y. H. Li, and B. Zhao, "First-principle study of magnetism induced by vacancies in graphene," *The European Physical Journal B-Condensed Matter and Complex Systems*, vol. 80, no. 3, pp. 343–349, 2011.
- [22] A. V. Krasheninnikov and R. M. Nieminen, "Attractive interaction between transition-metal atom impurities and vacancies in graphene: a first-principles study," *Theoretical Chemistry Accounts*, vol. 129, no. 3–5, pp. 625–630, 2011.
- [23] O. Cretu, A. V. Krasheninnikov, J. A. Rodríguez-Manzo, L. Sun, R. M. Nieminen, and F. Banhart, "Migration and localization of metal atoms on strained graphene," *Physical Review Letters*, vol. 105, Article ID 196102, 2010.
- [24] S. Haldar, B. S. Pujari, S. Bhandary et al., " Fe_n ($n = 1 - 6$) clusters chemisorbed on vacancy defects in graphene: stability, spin-dipole moment, and magnetic anisotropy," *Physical Review B*, vol. 89, no. 20, Article ID 205411, 2014.
- [25] A. V. Krasheninnikov, P. O. Lehtinen, A. S. Foster, P. Pyykkö, and R. M. Nieminen, "Embedding transition-metal atoms in graphene: structure, bonding, and magnetism," *Physical Review Letters*, vol. 102, no. 12, Article ID 126807, 4 pages, 2009.
- [26] G. Kim, S. Jhi, S. Lim, and N. Park, "Effect of vacancy defects in graphene on metal anchoring and hydrogen adsorption," *Applied Physics Letters*, vol. 94, Article ID 173102, 2009.
- [27] T. Eelbo, M. Waśniowska, P. Thakur et al., "Adatoms and clusters of 3d transition metals on graphene: electronic and magnetic configurations," *Physical Review Letters*, vol. 110, no. 13, Article ID 136804, 2013.
- [28] Y. Han, G.-X. Ge, J.-G. Wan, J.-J. Zhao, F.-Q. Song, and G.-H. Wang, "Predicted giant magnetic anisotropy energy of highly stable Ir dimer on single-vacancy graphene," *Physical Review B*, vol. 87, Article ID 155408, 2013.
- [29] A. W. Robertson, B. Montanari, K. He et al., "Dynamics of single Fe atoms in graphene vacancies," *Nano Letters*, vol. 13, no. 4, pp. 1468–1475, 2013.
- [30] A. V. Krasheninnikov, P. O. Lehtinen, A. S. Foster, P. Pyykkö, and R. M. Nieminen, "Embedding transition-metal atoms in graphene: structure, bonding, and magnetism," *Physical Review Letters*, vol. 102, no. 12, Article ID 126807, 2009.
- [31] J. A. Rodríguez-Manzo, O. Cretu, and F. Banhart, "Trapping of metal atoms in vacancies of carbon nanotubes and graphene," *ACS Nano*, vol. 4, no. 6, pp. 3422–3428, 2010.
- [32] K. Zhou, Y. Zhu, X. Yang, and C. Li, "One-pot preparation of graphene/ Fe_3O_4 composites by a solvothermal reaction," *New Journal of Chemistry*, vol. 34, no. 12, pp. 2950–2955, 2010.
- [33] G. Wang, T. Liua, X. Xiea, Z. Renb, J. Baic, and H. Wang, "Structure and electrochemical performance of Fe_3O_4 /graphene nanocomposite as anode material for lithium-ion batteries," *Materials Chemistry and Physics*, vol. 128, no. 3, pp. 336–340, 2011.
- [34] W. Fan, W. Gao, C. Zhang, W. W. Tjiu, J. Pan, and T. Liu, "Hybridization of graphene sheets and carbon-coated Fe_3O_4 nanoparticles as a synergistic adsorbent of organic dyes," *Journal of Materials Chemistry*, vol. 22, no. 48, pp. 25108–25115, 2012.
- [35] A. W. Robertson, G.-D. Lee, K. He, E. Yoon, A. I. Kirkland, and J. H. Warner, "The role of the bridging atom in stabilizing odd numbered graphene vacancies," *Nano Letters*, vol. 14, no. 7, pp. 3972–3980, 2014.
- [36] H. Wang, Q. Wang, Y. Cheng et al., "Doping monolayer graphene with single atom substitutions," *Nano Letters*, vol. 12, no. 1, pp. 141–144, 2012.
- [37] P. E. Blöchl, "Projector augmented-wave method," *Physical Review B*, vol. 50, Article ID 17953, 1994.
- [38] G. Kresse and J. Furthmüller, "Efficiency of ab-initio total energy calculations for metals and semiconductors using a plane-wave basis set," *Computational Materials Science*, vol. 6, no. 1, pp. 15–50, 1996.
- [39] J. P. Perdew, K. Burke, and M. Ernzerhof, "Generalized gradient approximation made simple," *Physical Review Letters*, vol. 77, article 3865, 1996.

Research Article

Photoactive Layer of DSSCs Based on Natural Dyes: A Study of Experiment and Theory

Yuanzuo Li,¹ Huixing Li,² Peng Song,³ and Chaofan Sun¹

¹College of Science, Northeast Forestry University, Harbin, Heilongjiang 150040, China

²School of Physics and Optoelectronic Technology, Dalian University of Technology, Dalian 116024, China

³Department of Physics, Liaoning University, Shenyang, Liaoning 110036, China

Correspondence should be addressed to Yuanzuo Li; yuanzuo.li@gmail.com

Received 10 August 2015; Accepted 12 October 2015

Academic Editor: Tran V. Cuong

Copyright © 2015 Yuanzuo Li et al. This is an open access article distributed under the Creative Commons Attribution License, which permits unrestricted use, distribution, and reproduction in any medium, provided the original work is properly cited.

Three natural dyes (*Forsythia suspensa*, Herba *Violae*, and Corn leaf) have been investigated as potential sensitizers for dye-sensitized solar cells. UV-vis absorption spectra reveal that three natural dyes mainly contain the compound of pheophytin a. Among three DSSCs, the highest photo electronic conversion efficiency η is 0.96% with open circuit voltage (V_{OC}) of 0.66 V, short circuit current density (I_{SC}) of 1.97 mA cm^{-2} , and fill factor (ff) of 0.74. Theoretical time-dependent density functional theory and charge difference density are used to explore the nature of excited states. Results demonstrate that the first state is an intramolecular charge transfer (ICT) state, and electron injection could occur owing to the thermodynamically driving force.

1. Introduction

Since the initial report on dye-sensitized solar cells (DSSCs) by Hagfeldt and Graetzel [1], much effort has been devoted toward designing and synthesizing metal-free photosensitizers to improve sunlight harvesting efficiency and yield efficient charge separation [2–5]. Most of the efficient DSSCs are sensitized with the dyes having ruthenium based complexes that have been shown to operate with power conversion around 10% using nanoporous TiO_2 electrodes [6]. However, due to the high cost of ruthenium complexes and the long term unavailability of these noble metals [7], there is a need to search for alternative photosensitizers for the use in TiO_2 -based photovoltaic devices.

Recently, several studies have focused on the natural dyes as DSSCs sensitizers [8–15] because the natural dyes could be extracted from flowers, vegetables, wood, seed, fruits, and so forth, by using minimal chemical procedures. Several natural pigments such as anthocyanin [10–12], chlorophyll [13], tannin [14], and carotene [15] have been used as sensitizer in DSSCs, and the highest photoelectronic conversion efficiency η based on natural dyes is around 2% [10, 11]. In this study, we extract three dyes from natural plants of *Forsythia suspensa*,

Herba *Violae*, and Corn leaf to use as DSSCs and achieve the highest efficiency $\eta = 0.96\%$ with a good fill factor of 0.74 under AM 1.5 using a density of power 100 mW/cm^2 .

2. Methods

Forsythia suspensa (Fs), Herba *Violae* (Hv), and Corn leaf (Cl) were collected fresh and kept in a vacuum furnace by controlling temperature at 70°C to remove the moisture. The dried samples were crushed in a mortar to make them into powder, and then powdered samples were mixed into ethanol, and the concentration of three samples is 1 g/mL . After extraction for about a week under the opaque condition, further purification of the extracts was avoided in order to achieve efficient sensitization using simple extraction procedures. The structure of DSSCs is mainly composed of electrode, dyes, and electrolyte solution. The elaborated preparation procedure is listed as follows: (a) the TiO_2 electrode was prepared; add 10 mL isopropyl titanate to water, and keep hydrolysis for 3 h; then add HNO_3 and HAC to the solution, under 80°C ; the mixed solution was stirred until it became transparent clear blue; later, at 200°C hydrothermal reaction was carried on for 12 h. After cooling and spin steaming,

centrifugal, terpineol ethyl, and cellulose were added to the ball grinder; the paste was prepared completely by ball mill, rotary steam, and three-roll mill. (b) The application of screen printing technology was used, which printed the TiO₂ paste to the clean surface of conductive glass, and the active area of cell was 0.16 cm²; after ethanol bath and drying, the anode electrodes were sintered, and then the anode electrodes were treated in TiCl₄ solution. In the next process, the anode electrodes were sintered as well, and after the processing, the anode immediately was removed after the natural cooling to 80°C, and the anode electrodes were soaked in the natural dye without light for 24 h. (c) The anode electrode and the platinum plating counter electrode were assembled into the cell, in the middle of the two electrodes, and the electrolyte solution was added (0.5 mol/L LiI, 0.05 mol/L I₂ TBP, and GUSCN were included). UV-vis spectra were measured with TU-1900 spectrometer (Beijing, China), and the FT-IR spectra were measured with FT-IR 360 spectrometer (Nicolet, Madison, WI, USA). Solar energy conversion efficiency measurements were done with a solar simulation instrument (Pecell-15, Japan), and light intensity was adjusted via a reference standard Si-solar solar cell at 1 sun light intensity of 100 mW cm⁻². Theoretically, the ground state optimization and absorption simulation were done with DFT/B3LYP [16–19] and TD-DFT/CAM-B3LYP [20, 21] using same basis set 6-31G(d). For comparison, M062x function was also used. All quantum chemical calculations were done with Gaussian 09 [22]. Quantum chemical calculations [23–27] and three-dimensional (3D) real-space analyses [25, 26] were used to study the relationship between structures and the optical properties, which has been used to explain charge transfer and excited states properties of organic system.

3. Results and Discussion

UV-vis absorption spectra of *Forsythia suspensa* (Fs), Herba Violae (Hv), and Corn leaf (Cl) in ethanol were shown in Figure 1(a), and for comparison, simulated absorption spectrum was shown in Figure 1(b), and the calculated data were listed in Table 1. It is found that the absorption spectra of three dyes cover the two absorption bands from 400 nm to 700 nm, and they display a strongest absorption band (666–669 nm) that corresponds to the red absorption band (666 nm) of pheophytin a [28, 29]. The calculation reproduces the two absorption spectra of dyes (see Figure 1(b)), and the first absorption in ethanol is found to be 595.51 nm ($f = 0.17$) by using TD-CAMB3LYP/6-31G(d)//B3LYP/6-31G(d), which makes a red shift of 50 nm compared with the first absorption peak with TD-M062x/6-31G(d)//B3LYP/6-31G(d) ($\lambda_{\max} = 545$ nm).

The transition energy and oscillator strength were listed in Table 1. As shown in Table 1, it is found that the excited state is composed of electron transition from HOMO to LUMO with the weight of 0.62279. It is very important for DSSCs to perform well with energy match; that is, the HOMO energy level should be laid below the redox couple, and LUMO energy level should be higher than that of TiO₂ semiconductor. Therefore, the energy level match is necessary

TABLE 1: Calculated transition energies and oscillator strengths TE (OS) and CI coefficients for the six excited states.

States	TE (OS)	CI coefficients	Cal. ^[a]
1	595.51 (0.1700)	(0.62279) H → L	545 nm
2	508.40 (0.0332)	(0.58102) H - 1 → L	
3	357.08 (0.8698)	(0.54625) H → L + 1	
4	352.01 (0.9375)	(0.53325) H - 1 → L	
5	335.49 (0.2486)	(0.61823) H - 2 → L	
6	316.61 (0.0088)	(0.50112) H - 5 → L	

^[a]Data from TD-M062x/6-31G(d)//B3LYP/6-31G(d).

TABLE 2: Current-voltage characteristics of *Forsythia suspensa* (Fs), Herba Violae (Hv), and Corn leaf (Cl).

	V _{OC} (V)	J _{SC} (mA/cm)	FF	Eff./%
Fs	0.64	2.01	0.70	0.90
Hv	0.66	1.97	0.74	0.96
Cl	0.61	0.99	0.78	0.47

for the optical electronic transfer and electron recovery in the system of solar cells. Comparison results show that the HOMO energy level is found to be -5.21 eV, which is lower than that of HOMO of the redox couple I⁻/I³⁻ (-4.8 eV [28, 29]), which means that excited dye can obtain electron from the redox couple to recovery; and LUMO energy level is -2.736 eV, which is above the conduction band of TiO₂. The energy gap is 2.474 eV, and exciton binding energy can be obtained from the difference values between excitation energy and energy gap, which are 0.392 eV and 0.199 eV through the two functional evaluations of CamB3LYP and M062x, respectively.

Fourier transform infrared spectrum of three dyes in the range of 400–4000 cm⁻¹ was measured experimentally, as shown in Figure 2(a). For comparison, a simulated spectrum in ethanol was also calculated theoretically (see Figure 2(b)). Figure 2(a) shows that the three dyes have similar shape and peak site of IR, and strong spectra of IR are found to be 3000–4000 cm⁻¹ and 1000–2000 cm⁻¹, that is, 1107.15, 1398.74, 1634.78, 2359.23, 2924.52, and 3420.00 cm⁻¹, respectively. Figure 2(b) shows that there is a peak site of 3520 cm⁻¹, and it is a vibration of N-H, as supported by the vibration analysis in Figure 3. From 3000 to 3200 cm⁻¹ region, the vibration of 3072 cm⁻¹ comes from the stretching vibration of C-H on polyene hydrocarbon (see Figure 3). The stretching vibrations of C=O on the thiophene units and carboxyl group are 1752 cm⁻¹ and 1795 cm⁻¹, respectively. The sharp and strong absorption peaks for C=C stretching mode and the out of plane of C-H bending mode were 1660 cm⁻¹ and 952 cm⁻¹, respectively.

Current-voltage curves for Fs (black line), Hv (red line), and Cl (blue line) were shown in Figure 4, respectively. Table 2 shows *I-V* (current-voltage) characteristics of the DSSCs sensitized with three dyes, which are composed of short circuit current density (*I*_{SC}), open circuit voltage (*V*_{OC}), fill factor (*ff*), and energy conversion efficiency (η). The DSSCs sensitized with Herba Violae dye showed conversion

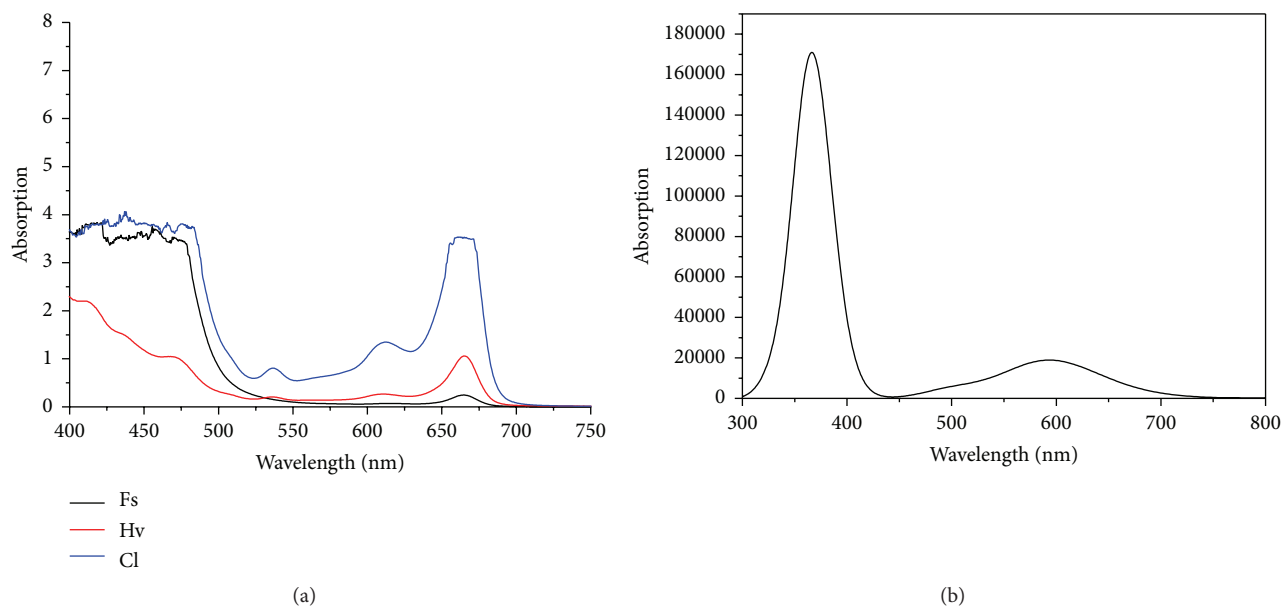


FIGURE 1: Absorption spectra of experiment (a) and simulation (b).

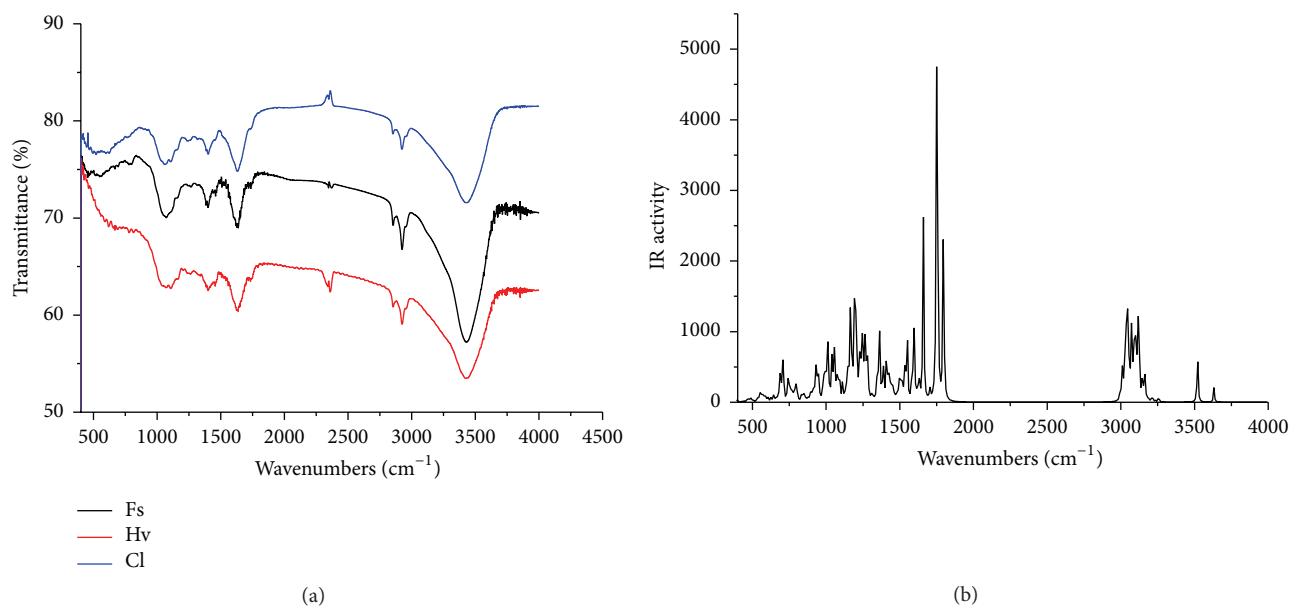


FIGURE 2: Experimental and theoretical IR spectra (a) and (b).

efficiency (η) of 0.96%, with open circuit voltage (V_{OC}) of 0.66 V, short circuit current density (I_{SC}) of 1.97 mA cm^{-2} , and fill factor (ff) of 0.74. The DSSCs sensitized with Fs showed conversion efficiency (η) of 0.90%, and the open circuit voltage of Fs is smaller than that of Hv, but short circuit current density of Fs is larger than that of Hv. For three solar cells, the values of V_{OC} and I_{SC} for Cl are both smaller than the two other cells, and its conversion efficiency (η) is 0.47.

To better study the excited states properties of the dye, the 3D real-space analysis is employed, which successfully explained the excited states properties of oligomers and polymers [25–27]. The 3D real-space analysis was

shown in Figure 5, and density of molecular orbital for HOMO and LUMO was shown in supporting materials Figure S1 in Supplementary Material available online at <http://dx.doi.org/10.1155/2015/139382>. From Figure S1, it is found that electron density distributions of the HOMO and LUMO are mainly located on the pheophytin body and there is no electron density under the polyene hydrocarbon, which are supported by charge difference density (CDD) analysis (see Figure 5). As shown, CDD shows that the excited state only occurs on the pheophytin body (where red and green represent the electron and hole, resp.). The state is an intramolecular charge transfer state (ICT) because the holes

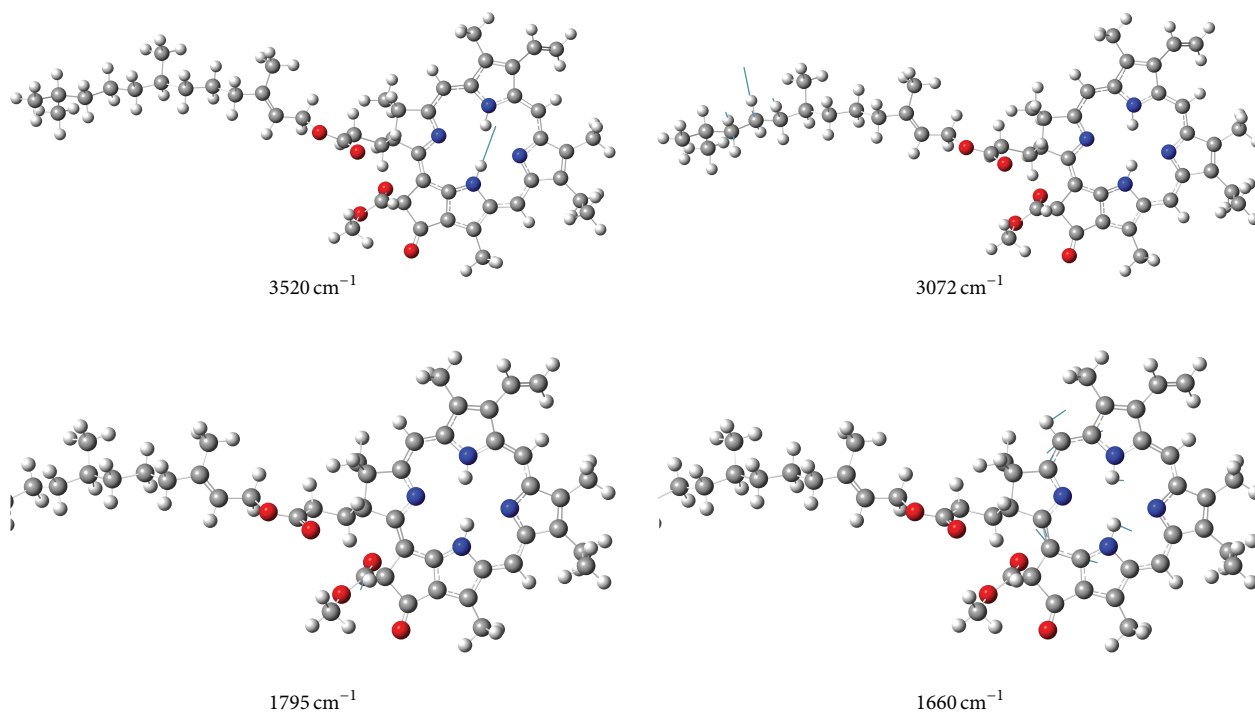


FIGURE 3: Vibration for IR spectrum.

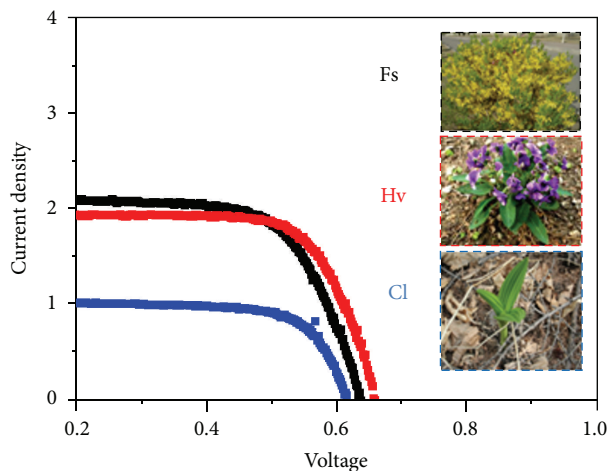


FIGURE 4: Current-voltage curve for FS (block line), Hv (red line), and Cl (blue line), respectively.

are located on the central rings, and electron is transferred into outside area. It is worth nothing that the red electrons are located on the attaching group C=O of pheophytin, and the increasing electron density upon the surface of semiconductor should be an important condition for the electron injection. The density of second state is similar to the first excited state. S3 and S4 are located excited states, and there is no electron upon attaching group. At the same time, the S6 excited state is also a located excited state (which is different with S3 and S4), and Figure 5 shows that excited

electron and hole pair almost only appear upon the attaching group.

For DSSCs, excited electron should be quickly injected from the discontinuous energy level of dyes into the CB of the semiconductor titanium dioxide. Thermodynamically, driving force of the electron injection process can be described as the difference between excited state oxidation potential $E_{\text{ex}}^{\text{ox}}$ and CB edges. From Rehm and Weller equation [30], $E_{\text{ex}}^{\text{ox}}$ can be calculated as follows:

$$E_{\text{ex}}^{\text{ox}} = E_{\text{gr}}^{\text{ox}} - E_{00}, \quad (1)$$

where $E_{\text{ex}}^{\text{ox}}$ and $E_{\text{gr}}^{\text{ox}}$ are the excited and ground state oxidation potentials and E_{00} is the electronic transition energy, and the ground state oxidation potential $E_{\text{gr}}^{\text{ox}}$ is computed from the HOMO energy. The value of $E_{\text{ex}}^{\text{ox}}$ is calculated to be -0.82 V which is more negative than the CB edge of TiO_2 (0.5 V versus normal hydrogen electrode (NHE)) [31–33], and electron injection is more easy to occur owing to the bigger difference between the excited state oxidation potentials and CB edge.

4. Conclusions

Three DSSCs based on natural dyes extracted from *Forsythia suspensa*, Herba Viola, and Corn leaf have been studied, and optical electronic results show that the highest photo-electronic conversion efficiency $\eta = 0.96\%$ with open circuit voltage (V_{OC}) of 0.66 V, short circuit current density (I_{SC}) of 1.97 mA cm^{-2} , and fill factor (ff) of 0.74. TD-DFT calculations show that the objected system has wide absorption region, and charge difference density demonstrated that there is an ICT state for the S1 state and provided the orientation

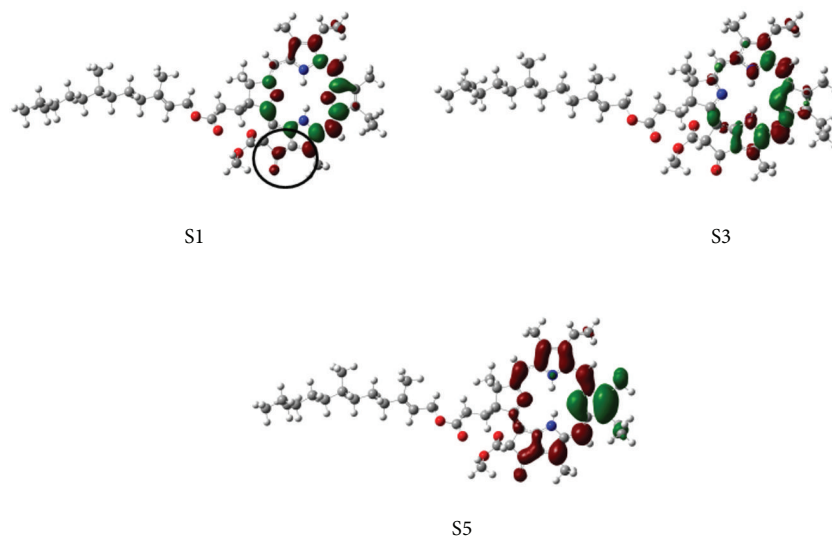


FIGURE 5: Charge difference density for calculated states.

of charge transfer. Electron injection is thermodynamically permitted.

Conflict of Interests

The authors declare no conflict of interests.

Acknowledgments

This work was supported by the Fundamental Research Funds for the Central Universities (Grant no. 2572014CB31), the Heilongjiang Provincial Youth Science Foundation (Grant no. QC2013C006), and the National Natural Science Foundation of China (Grant nos. 11404055 and 11374353).

References

- [1] A. Hagfeldt and M. Graetzel, "Light-induced redox reactions in nanocrystalline systems," *Chemical Reviews*, vol. 95, no. 1, pp. 49–68, 1995.
- [2] S. Ito, S. M. Zakeeruddin, R. Humphry-Baker et al., "High-efficiency organic-dye-sensitized solar cells controlled by nanocrystalline-TiO₂ electrode thickness," *Advanced Materials*, vol. 18, no. 9, pp. 1202–1205, 2006.
- [3] N. Koumura, Z. S. Wang, S. Mori, M. Miyashita, E. Suzuki, and K. Hara, "Alkyl-functionalized organic dyes for efficient molecular photovoltaics," *Journal of the American Chemical Society*, vol. 128, no. 44, pp. 14256–14257, 2006.
- [4] H. N. Tian, X. C. Yang, R. K. Chen et al., "Phenothiazine derivatives for efficient organic dye-sensitized solar cells," *Chemical Communications*, no. 36, pp. 3741–3743, 2007.
- [5] K. Hara, M. Kurashige, Y. Dan-Oh et al., "Design of new coumarin dyes having thiophene moieties for highly efficient organic-dye-sensitized solar cells," *New Journal of Chemistry*, vol. 27, no. 5, pp. 783–785, 2003.
- [6] T. Bessho, E. Yoneda, J.-H. Yum et al., "New paradigm in molecular engineering of sensitizers for solar cell applications," *Journal of the American Chemical Society*, vol. 131, no. 16, pp. 5930–5934, 2009.
- [7] T. Funaki, H. Funakoshi, O. Kitao et al., "Cyclometalated ruthenium(II) complexes as near-IR sensitizers for high efficiency dye-sensitized solar cells," *Angewandte Chemie*, vol. 51, no. 30, pp. 7528–7531, 2012.
- [8] G. Calogero, A. Bartolotta, G. Di Marco, A. Di Carlo, and F. Bonaccorso, "Vegetable-based dye-sensitized solar cells," *Chemical Society Reviews*, vol. 44, no. 10, pp. 3244–3294, 2015.
- [9] N. A. Ludin, A. M. A.-A. Mahmoud, A. B. Mohamad, A. A. H. Kadhum, K. Sopian, and N. S. A. Karima, "Review on the development of natural dye photosensitizer for dye-sensitized solar cells," *Renewable and Sustainable Energy Reviews*, vol. 31, pp. 386–396, 2014.
- [10] M. Shahid, S. Ul-Islam, and F. Mohammad, "Recent advancements in natural dye applications: a review," *Journal of Cleaner Production*, vol. 53, pp. 310–331, 2013.
- [11] M. R. Narayan, "Review: dye sensitized solar cells based on natural photosensitizers," *Renewable and Sustainable Energy Reviews*, vol. 16, no. 1, pp. 208–215, 2012.
- [12] R. Hemmatzadeh and A. Jamali, "Enhancing the optical absorption of anthocyanins for dye-sensitized solar cells," *Journal of Renewable and Sustainable Energy*, vol. 7, no. 1, Article ID 013120, 2015.
- [13] G. R. A. Kumara, S. Kaneko, M. Okuya, B. Onwona-Agyeman, A. Konno, and K. Tennakone, "Shiso leaf pigments for dye-sensitized solid-state solar cell," *Solar Energy Materials and Solar Cells*, vol. 90, no. 9, pp. 1220–1226, 2006.
- [14] R. Espinosa, I. Zumeta, J. L. Santana et al., "Nanocrystalline TiO₂ photosensitized with natural polymers with enhanced efficiency from 400 to 600 nm," *Solar Energy Materials and Solar Cells*, vol. 85, no. 3, pp. 359–369, 2005.
- [15] E. Yamazaki, M. Murayama, N. Nishikawa, N. Hashimoto, M. Shoyama, and O. Kurita, "Utilization of natural carotenoids as photosensitizers for dye-sensitized solar cells," *Solar Energy*, vol. 81, no. 4, pp. 512–516, 2007.
- [16] J. M. R. Dreizler and E. K. U. Gross, *Density Functional Theory*, Springer, Heidelberg, Germany, 1990.

- [17] A. D. Becke, "Density-functional exchange-energy approximation with correct asymptotic behavior," *Physical Review A*, vol. 38, no. 6, pp. 3098–3100, 1988.
- [18] A. D. Becke, "Density-functional thermochemistry. III. The role of exact exchange," *The Journal of Chemical Physics*, vol. 98, no. 7, p. 5648, 1993.
- [19] C. Lee, W. Yang, and R. G. Parr, "Development of the Colle-Salvetti correlation-energy formula into a functional of the electron density," *Physical Review B*, vol. 37, no. 2, pp. 785–789, 1988.
- [20] R. E. Stratmann, G. E. Scuseria, and M. J. Frisch, "An efficient implementation of time-dependent density-functional theory for the calculation of excitation energies of large molecules," *The Journal of Chemical Physics*, vol. 109, no. 19, pp. 8218–8224, 1998.
- [21] T. Yanai, D. P. Tew, and N. C. Handy, "A new hybrid exchange-correlation functional using the Coulomb-attenuating method (CAM-B3LYP)," *Chemical Physics Letters*, vol. 393, no. 1–3, pp. 51–57, 2004.
- [22] M. J. Frinch, G. W. Trucks, H. B. Schlegel et al., *Gaussian 09 (Revision A.1)*, Gaussian, Wallingford, Conn, USA, 2009.
- [23] J. A. Talla, S. A. Salman, H. Sabbah, E. Yasin, and A. A. Zir, "Modeling single-walled boron nitride nanotube pressure sensor: density functional study," *Nanoscience and Nanotechnology Letters*, vol. 7, no. 6, pp. 500–506, 2015.
- [24] G. J. Zhao and K. L. Han, "Hydrogen bonding in the electronic excited state," *Accounts of Chemical Research*, vol. 45, no. 3, pp. 404–413, 2012.
- [25] Y. Z. Li, T. Pullerits, M. Y. Zhao, and M. T. Sun, "Theoretical characterization of the PC₆₀BM:PDDTT model for an organic solar cell," *Journal of Physical Chemistry C*, vol. 115, no. 44, pp. 21865–21873, 2011.
- [26] P. Song, Y. Z. Li, F. C. Ma, and M. T. Sun, "Insight into external electric field dependent photoinduced intermolecular charge transport in BHJ solar cell materials," *Journal of Materials Chemistry C*, vol. 3, no. 18, pp. 4810–4819, 2015.
- [27] X. M. Zhao and M. D. Chen, "DFT study on the influence of electric field on surface-enhanced Raman scattering from pyridine-metal complex," *Journal of Raman Spectroscopy*, vol. 45, no. 1, pp. 62–67, 2014.
- [28] S. M. Milenković, J. B. Zvezdanović, T. D. Andjelković, and D. Z. Marković, "The identification of chlorophyll and its derivatives in the pigment mixtures: HPLC-chromatography, visible and mass spectroscopy studies," *Advanced Technologies*, vol. 1, no. 1, pp. 16–24, 2012.
- [29] V. Shanmugam, S. Manoharan, A. Sharafali, S. Anandan, and R. Murugan, "Green grasses as light harvesters in dye sensitized solar cells," *Spectrochimica Acta—Part A: Molecular and Biomolecular Spectroscopy*, vol. 135, pp. 947–952, 2015.
- [30] A. Hagfeldt, G. Boschloo, L. C. Sun, L. Kloo, and H. Pettersson, "Dye-sensitized solar cells," *Chemical Reviews*, vol. 110, no. 11, pp. 6595–6663, 2010.
- [31] D. Rehm and A. Weller, "Kinetics of fluorescence quenching by electron and H-atom transfer," *Israel Journal of Chemistry*, vol. 8, no. 2, pp. 259–271, 1970.
- [32] C. Y. Qin and A. E. Clark, "DFT characterization of the optical and redox properties of natural pigments relevant to dye-sensitized solar cells," *Chemical Physics Letters*, vol. 438, no. 1–3, pp. 26–30, 2007.
- [33] K. Kalyanasundaram and M. Grätzel, "Applications of functionalized transition metal complexes in photonic and optoelectronic devices," *Coordination Chemistry Reviews*, vol. 177, no. 1, pp. 347–414, 1998.